Electromechanical interactions in lithium-ion batteries: Aging effects and analytical use

**Dissertation zur Erlangung des naturwissenschaftlichen
Doktorgrades der Julius-Maximilians-Universität Würzburg**

Vorgelegt von

Tobias Bach

aus Stuttgart

Würzburg, 2017

Eingereicht bei der Fakultät für Chemie und Pharmazie

Gutachter der schriftlichen Arbeit:

1. Gutachter: Prof. Dr. Gerhard Sextl

2. Gutachter: _____

Prüfer des öffentlichen Promotionskolloquiums:

1. Prüfer: Prof. Dr. Gerhard Sextl

2. Prüfer: _____

3. Prüfer: _____

Datum des öffentlichen Promotionskolloquiums

_____

Doktorurkunde ausgehändigt am

_____

Für Eva und Wolfgang

Table of Contents

1 Introduction and aim of the thesis[1]

1.1 Challenges for lithium-ion cells and aim of the thesis

1.1.1 Motivation

Lithium-ion batteries are the most advanced technology for both stationary and mobile energy storage devices due to their high energy density and efficiency.[1,2] Lithium-ion technology enables new applications in various fields such as consumer devices and electrified vehicles. Indeed, innovations such as smartphones and electric sports cars could not be successful with preceding battery technologies. Capacity and power capability of lithium-ion batteries are quickly increasing and important achievements have been made recently to address safety issues. Today, cost limits the range of electric vehicles below the luxury segment just as much as technical feasibility. The current uncertainty regarding the reachable use time and subsequently the return on investment inhibits deeper market penetration. Understanding aging mechanisms not only allows perfecting design and control of lithium-ion cells, but is also the basis for broader acceptance. The aging of lithium-ion cells is not only influenced by chemical factors but also by mechanical effects such as expansion of active materials, compression and resulting stresses.[3,4] But interactions between mechanic effects and electrochemistry are not only negative. Clearly, close inspection of mechanical effects also opens new ways to characterize the state of charge and health in research and application.[5–7]

1.1.2 Research cooperation ABattReLife

The European project ABattReLife - Automotive Battery Recycling and 2nd Life aimed to tackle cost and environmental issues of lithium batteries by a multidisciplinary approach. As a great portion of this thesis is based on results obtained during cooperation in ABattReLife, its main work packages are presented.

Ten industrial and academic institutions from France, the Netherlands and Germany partnered to investigate the aging of automotive lithium-ion batteries, their potential reuse in second-life applications as well as improved recycling methods. The research was not limited to technical and scientific improvements but life-cycle assessments and improved business models were also developed.

---

[1] This chapter has been published in parts under creative commons licence CC BY 4.0: T. C. Bach, S. F. Schuster, E. Fleder, J. Müller, M. J. Brand, H. Lorrmann, A. Jossen, G. Sextl, Nonlinear aging of cylindrical lithium-ion cells linked to heterogeneous compression, Journal of Energy Storage (2016), in press, http://dx.doi.org/10.1016/j.est.2016.01.003.

An overview of the work packages is given in Figure 1.1. This work is focused on work package WP1 and the results in chapters 4 and 5 were gained as part of a close cooperation with the Institute for Electrical Energy Storage Technology of TU München.
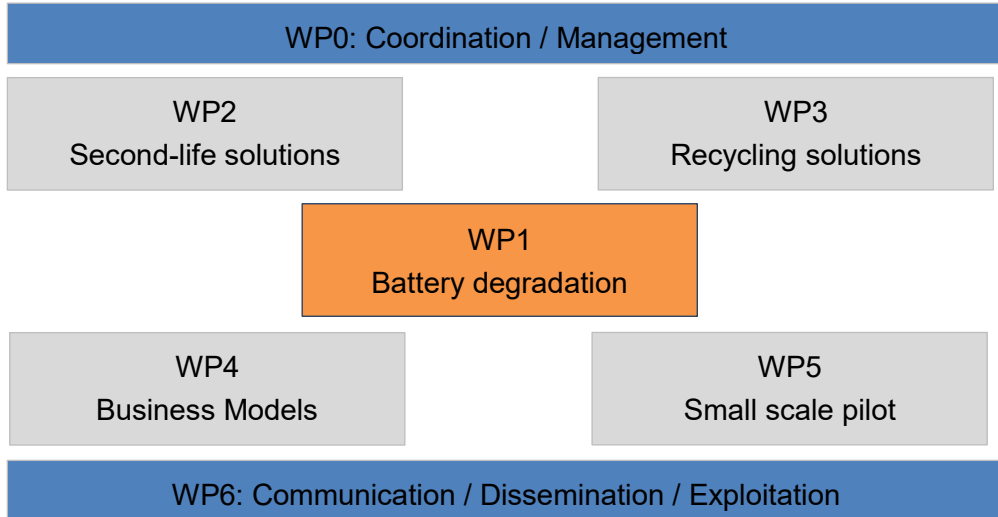

Figure 1.1 Work packages of the European Project ABattReLife. The results presented in this thesis arise from cooperation of the Fraunhofer ISC in work package WP1, which is therefore highlighted. Close cooperation between all partners across work packages made the joint project ABattReLife successful. A selection of results is presented in this thesis.

1.1.3   Scope of the thesis

In this chapter, the outlines of this thesis are introduced and the presented work is set into context. In chapter 2 the theoretical background and the state of the art are presented in a concise format. Chapter 3 outlines the experimental setups and procedures used to obtain the analytical results of the following chapters.

Reports in literature about suddenly increasing aging rates raise concern regarding the viability of aging models and their use in lifetime projections.[8–10] In chapter 4, this aging effect is investigated in detail and effects of heterogeneous pressure on lithium-ion cell aging are presented. It is shown that differences in compression induced by the mechanical design of the investigated cells cause variations in local currents and degrees of lithiation. Furthermore, the importance of limiting graphite lithiation to moderate levels is confirmed, as both very high and low levels may lead to materials degradation. Furthermore, design imperfections and use conditions leading to such unfavorable behavior are discussed.

In mobile applications, as well as in the transport of lithium-ion cells, vibrations and shocks can never be fully avoided. These stress factors may damage improperly designed cells. Nonetheless, the issue has found limited attention in scientific literature.

In chapter 5, cells exposed to vibrations and shocks are investigated for possible failures and design recommendations are derived. To understand the behavior of the most basic part of any battery pack, cells of cylindrical and pouch type were exposed to different load profiles. Mechanic and electrical testing was carried out by the Institute for Electrical Energy Storage Technology, Technische Universität München and the TÜV SÜD Battery Testing GmbH. Cells were characterized using X-Ray computed tomography carried out at the Fraunhofer Center for High-Temperature Materials and Design. The results presented in this work focus on observations gained from computed tomography and Post-Mortem investigations. Details on impedance and capacity investigations are found in a joint publication[11].

In chapter 6 the gained understanding of electrochemical processes and mechanical interactions is used to develop a new characterization method based on small-signal ultrasonic pulses. It is shown that it is possible to determine the state of charge of different cell chemistries by simple ultrasonic pulses. As the method can be implemented with galvanic insulation to the cells' electrodes, the relationships found in this work may be used to control lithium-ion batteries on cell level.

The underlying acoustic effects will be explained by transferring existing acoustic theories from geological prospecting and scaling them to length scales encountered in lithium-ion batteries. Using readily available materials properties of graphite electrodes, observed effects are explained by theoretical predictions.

Based on the gained understanding, a quick method for finding optimal frequencies will be presented. Using this method, the versatility of the ultrasonic approach is demonstrated by applying it to a lithium iron phosphate based cell. Finally, a practical implementation based on existing features of a cheap microcontroller will be presented.

Chapter 7 and 8 summarize the results of this thesis and provide a critical discussion in English and German respectively. The conclusions drawn are put in context and an outlook is given.

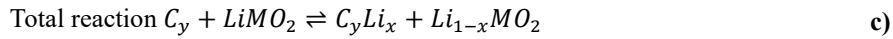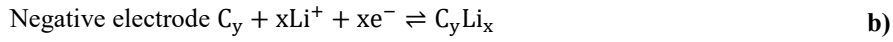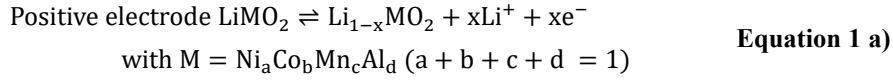# 2 State of the art and theoretical background[1]

2.1 History and Basic Principle of Lithium-Ion Cells

Any galvanic cell is composed of three basic elements, a negative electrode, an electrolyte and a positive electrode. As the voltage of any galvanic element is defined by the difference of the electrodes' potentials, it is desirable to use materials with working potentials at the extremes of the electrochemical series. Furthermore, the used materials should provide high gravimetric and volumetric charge density. The invention of the lithium-ion battery should be understood as a historic process as its functional principle relies on several fortunate circumstances. In his article "The Birth of the Lithium-Ion Battery", Akira Yoshino explains how combining the most promising materials available at the time shaped basic concepts of the rocking chair battery.[12]

Lithium metal is a natural candidate for the negative electrode, as it has the most negative normal potential of all known substances, namely -3,045 V against the standard hydrogen electrode.[13] Furthermore, its small atomic mass and ionic radius, potentially resulting in low battery weight and fast diffusion constants, make it even more suitable for battery applications.[14] While primary lithium metal batteries are very successful, the reversible operation in a secondary cell has been slowed down by diverse issues including dendrite formation[15–17] and continuous decomposition of the electrolytes under cyclic load.[17,18] Due to these issues, a replacement for lithium metal on the negative electrode with comparably negative potentials had to be found. Yazami and Tousain are credited to be the first to report[19] on the use of graphite as a reversible intercalation host for lithium in a galvanic cell,[12] although lithium intercalation compounds were known before.[20] Carbonaceous intercalation compounds operate at potentials close to that of lithium but no dendrites are formed during normal operation and very good efficiencies can be obtained.[21] A suitable, highly reversible positive electrode had already been reported by Mizushima *et al*.[22] Koichi Mizushima and John B. Goodenough not only invented the lithium cobalt oxide intercalation electrode but did also foresee their use for batteries with high energy densities. Soon, alternative positive active materials incorporating further metals such as manganese, nickel and aluminum emerged.[23] The combination of these concepts led to the creation and marketing of the lithium-ion battery.[24] First lithium-ion batteries did not use graphite as negative electrode, because no stable electrolyte was available. This issue could be overcome by the use of lithium

---

[1] This chapter has been published in parts under creative commons licence CC BY 4.0: T. C. Bach, S. F. Schuster, E. Fleder, J. Müller, M. J. Brand, H. Lorrmann, A. Jossen, G. Sextl, Nonlinear aging of cylindrical lithium-ion cells linked to heterogeneous compression, Journal of Energy Storage (2016), in press, http://dx.doi.org/10.1016/j.est.2016.01.003.

hexafluorophosphate (LiPF$_6$) in a mixture of ethylene carbonate (EC) and dimethyl carbonate (DMC) or diethyl carbonate (DEC).[23,25]

Positive electrode $\text{LiMO}_2 \rightleftharpoons \text{Li}_{1-x}\text{MO}_2 + x\text{Li}^+ + x\text{e}^-$
with $\text{M} = \text{Ni}_a\text{Co}_b\text{Mn}_c\text{Al}_d$ $(a + b + c + d \ = 1)$

Equation 1 a)

Negative electrode $\text{C}_y + x\text{Li}^+ + x\text{e}^- \rightleftharpoons \text{C}_y\text{Li}_x$

b)

Total reaction $C_y + LiMO_2 \rightleftharpoons C_yLi_x + Li_{1-x}MO_2$

c)

Most of today's lithium-ion batteries still contain a negative graphite electrode, a metal oxide positive electrode and an organic carbonate-based electrolyte, because this combination allows for long cycle life, acceptable cost as well as high energy and power density.[2] The half-cell reactions taking place at the electrodes are detailed in Equation 1a) and b). The total reaction in Equation 1c) consists of two intercalation equilibria, and does not lead to any changes in solvated lithium salts. Therefore, the lithium-ion cell is often described as a rocking-chair system.

While the form factor of lithium-ion cells and accordingly the placement of the electrodes vary, they share a common functional unit. Figure 2.1 illustrates this functional unit for the example of a cylindrical cell. Negative and positive active materials are applied onto current collectors and stacked alternating with a separator. They are then wound into a jelly roll or stacked.
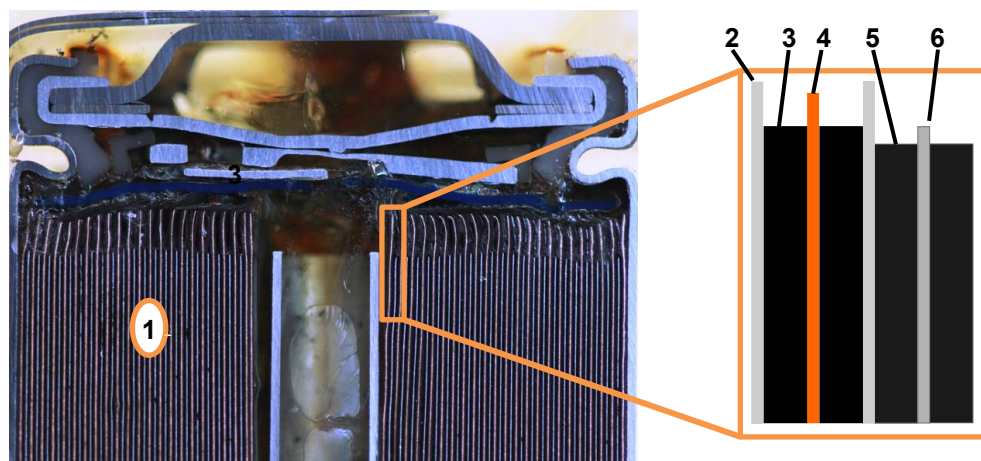
1 Jelly Roll

2 Separator

3 Negative active material

4 Negative current collector

5 Positive active material

6 Positive current collector

Figure 2.1 Cross section of a lithium-ion battery with schematic. A section of a deep-discharged lithium-ion cell is shown to illustrate the components. The schematic magnification shows the electrode stack wound into the jelly roll (1).

2.2 Components of modern lithium-ion batteries

2.2.1 Negative electrode

Graphite can be considered the most successful material for lithium-ion negative electrodes.[12,26–28] Its high theoretical gravimetric charge density of 372 mAh g^{-1},[21] which can be approached in practical applications,[29,30] exceeds the specific capacities of all known positive intercalation compounds, which will be presented in the next subchapter. This high gravimetric charge density and it's working potential below 0.5 V vs. Li/Li$^+$ make it an excellent choice for high energy applications. While lithium titanate excels in safety and aging properties, it's higher potential of approximately 1.5 V vs. Li/Li$^+$ limits its commercial use. In this work, only batteries with graphitic electrodes will be considered and readers interested in a broader overview on alternative materials are directed to a review on the topic[26] and more detail on lithium titanates can be found in reference[28] and[31].
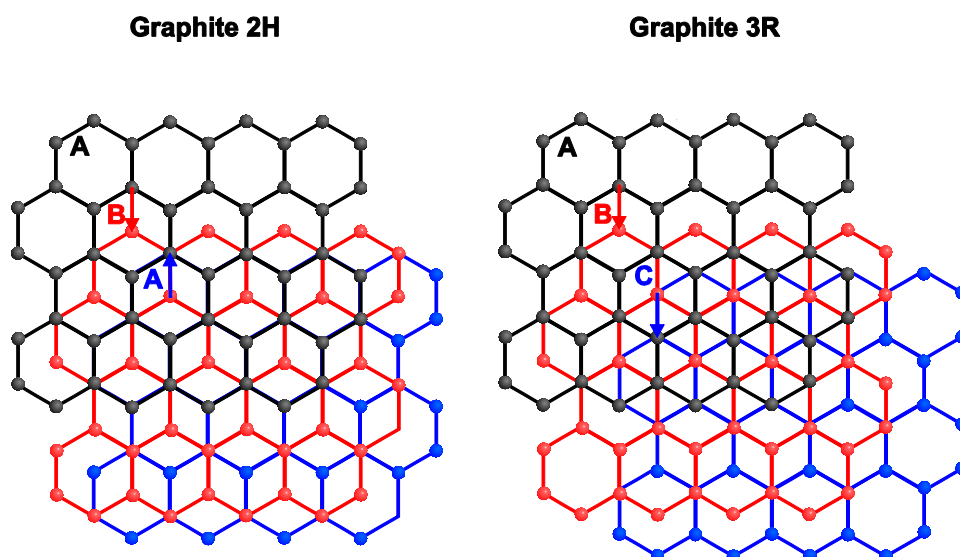
Graphite 2H **Graphite 3R**

Figure 2.2 Layer arrangement in graphite. Projections along the principal axis of the two crystal structures, graphite 2H and 3R that coexist in natural graphite.[32] The minor component graphite 3R is obtained by repeating the shift already found between A and B. As the energy difference is low, the phases can be transformed by mechanical and thermal influence, respectively.[33]

As many properties of graphite negative electrodes can be understood in terms of their crystallographic structure, its general properties are explained here. A general introduction to crystallography can be found in reference[34]. Natural graphite contains two modifications, the hexagonal graphite 2H and the rhombohedral graphite 3R, who share approximately the same bond-length of 0.142 nm and an interlayer spacing of 0.336 nm.[33] Figure 2.2 shows the difference in shifting. Graphite 2H is formed by alternately shifting the layers by ± 1/3 of the lattice parameter *a* or an equivalent movement, thus creating an A-B pattern.[32] Graphite 3R can be created by always shifting the layers in the same direction, therefore creating an A-B-C pattern.[32] Both phases are reported to provide indiscernible voltages in lithium-ion batteries.[33] On the other hand, the coexistence of the two phases may cause improved capacities and impedances due to favorable disordering at the phase boundaries.[29,30] Another important factor is the ratio of the surface areas of basal and edge planes, the basal plane being perpendicular to the principal axis of the crystal lattice, and the edge planes parallel to it. Lithium ions can insert into the graphite layers through the edge plane, while the basal plane is inactive due to the dense graphite layers[35]

The interlayer distance increases upon lithiation and the layer arrangement is changed to A-A layering.[36] Lithium intercalation takes place layer wise and in dilute stages two or more graphene layers are situated between two intercalated layers. Therefore, stages are characterized by the number of layers between intercalated lithium layers.[37,38] The electrochemical behavior is dominated by the coexistence of these stages.[37] The resulting voltage plateaus are shown in Figure 2.3.
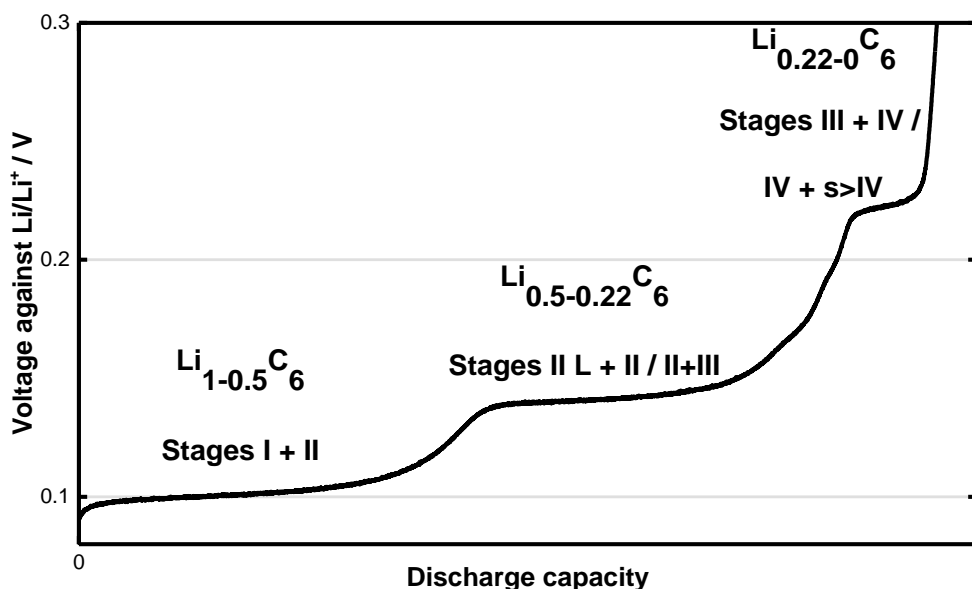
Figure 2.3 Staging observed upon delithiation of graphite. Lithium intercalation and deintercalation takes place in stages. Stages are characterized by the coexistence of two phases with different numbers of graphene layers *s* between lithiated layers which are written in roman numbers. Figure based on slow galvanostatic discharge with 0.02 C of a graphite electrode and inspired by[37].

The intercalation of lithium in graphite leads to volume changes.[36,39] These changes are not only a source of mechanical stress but also a valuable source of information on the state of the negative electrode. The resulting changes of thickness[40] and stress[5,41] allow to investigate the state of charge and health of lithium-ion cells. Furthermore, the change in mechanical properties such as modulus[42] and porosity[43] of the electrodes provides further possibilities for state estimation as will be demonstrated in chapter 6.

2.2.2 Positive electrode

Positive electrode materials are usually either lithiated transition metal oxides or phosphates.[44] The transition metal is chosen so that it can change to a higher valence when lithium is removed from the crystal structure. Lithium cobaltate forms layered crystal structures of the space group $R\bar{3}m$ that allow for facile lithium diffusion.[44,45] While its high theoretical capacity of 274 mAh g^{-1} and voltage are very advantageous, extraction of more than half of the available lithium leads to oxygen evolution and increased mechanic stress.[46] This drawback, thermal safety issues[47] as well as the high price of cobalt led to the development of a wide range of cathode materials. Reported discharge capacities and voltages are summarized in Figure 2.4 and Table 2.1. A rough categorization is attempted by grouping them into "state of the art" used today, "high voltage" and "high energy" materials. In general materials boasting high voltages suffer from poor cyclability,[48] while low voltage materials such as lithium iron phosphate lead to reduced energy densities.
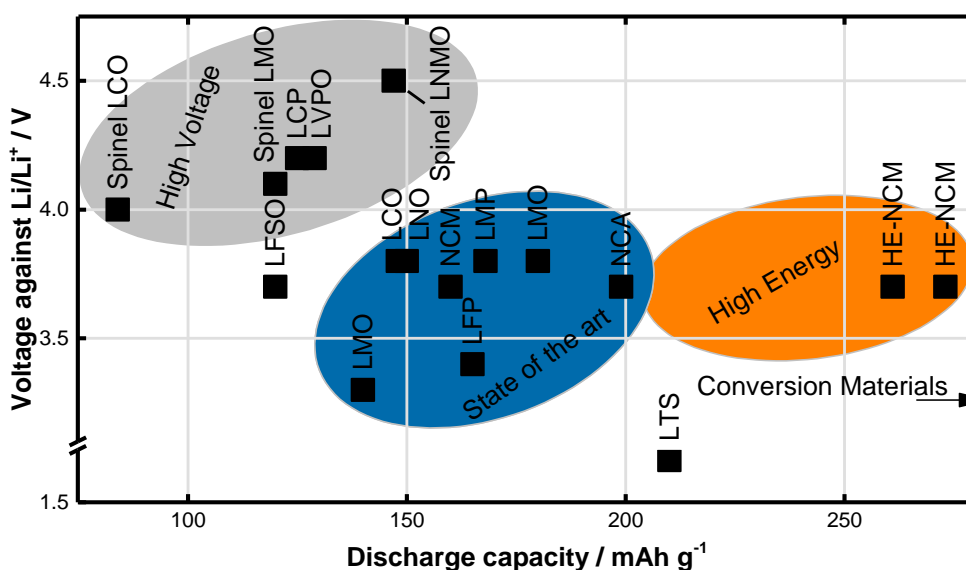
Figure 2.4 Discharge capacities and voltages reported for positive active materials. Graphic representation of voltages and capacities of materials listed in Table 2.1, which is mainly based on data from Nitta *et al.*[26] Materials are roughly categorized into "state of the art" materials used today, as well as the "high voltage" and "high energy" materials in development. Conversion materials such as sulfur would allow a leap in capacities but are still in early development.

In this work, positive electrodes of lithium nickel cobalt manganese oxide (NCM) with a stoichiometry of $Li_{1.11 \pm 0.02}Ni_{0.33 \pm 0.01}Mn_{0.33 \pm 0.01}Co_{0.33 \pm 0.01}O_2$ were investigated. Equimolar NCM was described in 2001 by Ohzuku *et al.*[49] and later improved[50] by increasing the lithium content. Its balanced properties regarding cost, safety and energy density have made it a material of choice for early automotive applications.[44]

The development of cheaper cells with improved energy density goes on. As of today, all positive active materials, except conversion materials such as sulfur,[26] exhibit lower gravimetric charge densities than graphite. These low gravimetric charge densities q limit the achievable specific energy w of modern lithium-ion batteries, as does the mean cell voltage U_{cell} as shown in Equation 2. While increased cell voltage has a direct proportional effect on specific energy, the gravimetric charge density has a more complex influence. Equation 3 shows the dependence of the cells theoretical gravimetric charge capacity q_{cell} on the gravimetric charge capacities of positive ($q_{positive}$) and negative ($q_{negative}$) mass. In practice, this value is further decreased by inactive components.

$$q_{cell} * U_{cell} = w_{cell}$$
Equation 2

$$q_{cell} = \frac{1}{q_{negative}^{-1} + q_{positive}^{-1}}$$
Equation 3

Based on the assumption of a balanced graphite counter electrode, the influence of the positive mass is visualized in Figure 2.5. The graph shows the potential benefit of high energy materials such as lithium and manganese rich layered lithium nickel cobalt manganese oxides, and the downside of high voltage materials listed in Table 2.1. Even based on moderate voltage windows as they are used today, high energy materials allow charge densities above 200 mAh g^{-1}.[51,52] Still, the gravimetric charge density of graphite is currently only surpassed by conversion materials such as sulfur.[26]
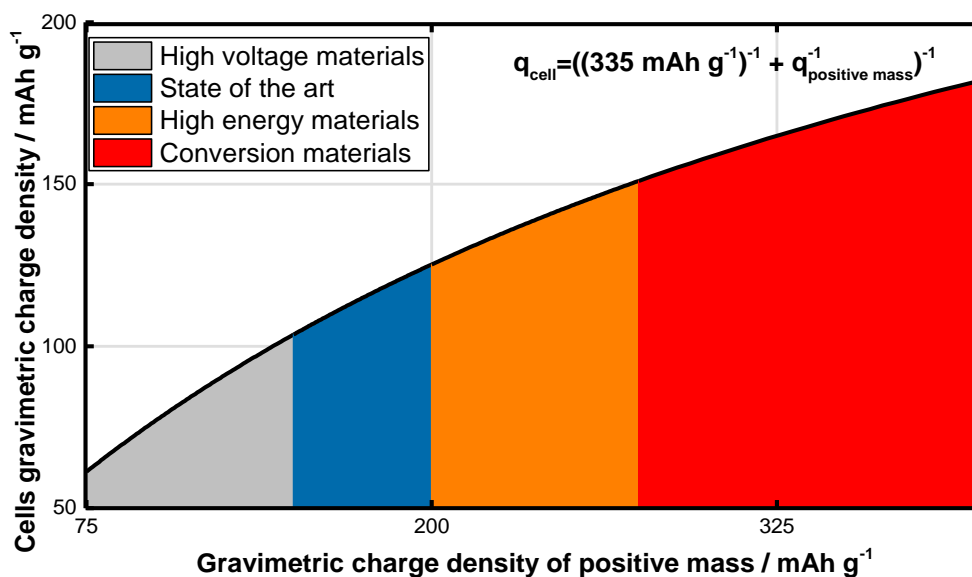
Figure 2.5 Theoretical gravimetric charge density using graphite as negative mass. The theoretical cell discharge capacity is calculated assuming the use of a balanced graphite electrode yielding a charge density of the negative mass of $372 \text{ mAh g}^{-1} \times 0.9 = 335 \text{ mAh g}^{-1}$. The example shows the steep increase in gravimetric charge density upon improvement of the positive mass.
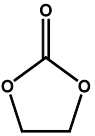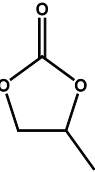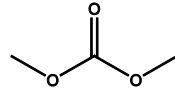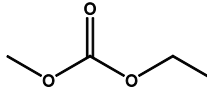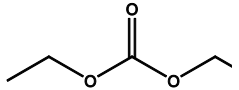
Table 2.1 Measured Capacities and nominal voltages of positive active materials. Capacity and voltage of different positive active materials are compared based on literature data. Expanded upon a table published by *Nitta et al.*[26]

Crystal structure	Abbreviation	Stoichiometry	Charge density / mAh g⁻¹	Voltage / V	Ref.
	LTS	$LiTiS_2$	210	1.9	[26,53]
	LCO	$LiCoO_2$	148	3.8	[26,54]
	LNO	$LiNiO_2$	150	3.8	[26,55]
	LMO	$LiMnO_2$	140	3.3	[26,56]
Layered	NCM	$LiNi_{0.33}Mn_{0.33}Co_{0.33}O_2$	160	3.7	[26,57]
	HE-NCM	$LiNi_{0.17}Li_{0.2}Co_{0.07}Mn_{0.56}O_2$	273	3.7	[51]
	HE-NCM	$Li_{1.2}Mn_{0.51}Ni_{0.19}Co_{0.1}O_2$	261	3.7	[58]
	NCA	$LiNi_{0.8}Co_{0.15}Al_{0.05}O_2$	199	3.7	[26,59]
	LMO	Li_2MnO_3	180	3.8	[26,60]
	Spinel LMO	$LiMn_2O_4$	120	4.1	[26,61]
Spinel	Spinel LCO	$LiCo_2O_4$	84	4.0	[26,62]
	Spinel LNMO	$LiNi_{0.5}Mn_{1.5}O_4$	147	4.5	[63]
	LFP	$LiFePO_4$	165	3.4	[26,64]
Olivine	LMP	$LiMnPO_4$	168	3.8	[26,65]
	LCP	$LiCoPO_4$	125	4.2	[26,66]
Tavorite	LFSO	$LiFeSO_4F$	120	3.7	[26,67]
	LVPO	$LiVPO_4F$	129	4.2	[26,68]

2.2.3 Electrolyte

Negative and positive active materials and the rocking-chair mechanism were discussed in the previous sections. The associated lithium migration relies on a suitable electrolyte with high diffusivity and excellent electrochemical stability. Today's electrolytes are complicated mixtures which are usually based on ethylene carbonate combined with linear carbonates such as diethyl carbonate, dimethyl carbonate and ethyl methyl carbonate to which lithium hexafluorophosphate, $LiPF_6$, is added. As shown in Table 2.2 the cyclic ethylene carbonate excels with high dipole moments, allowing solvation of the conducting salt, but its high viscosity limits ion mobility. Linear carbonates with lower viscosity are added to enhance low temperature rate capability.

Table 2.2 Viscosities and dipole moments of popular solvents. Viscosities and Dipole moments of standard carbonates are compared. The cyclic carbonates share excellent dipole moments but also high viscosities. The linear carbonates exhibit low viscosities but very low dipole moments. Therefore, mixtures of several solvents are used. Data based on reference [69].

Molecule Structure	Name	Dynamic viscosity at 25 °C / mPa s	Dielectric permittivity / ε_0
	Ethylene carbonate	Solid at 25 °C, 1.9 at 40 °C	Solid at 25 °C, 90 at 40 °C
	Propylene carbonate	2.5	65
	Dimethyl carbonate	0.59	3.1
	Ethyl methyl carbonate	0.65	3.0
	Diethyl carbonate	0.75	2.8

Other solvents such as propylene carbonate and esters such as those shown in Figure 2.6 are used to widen the useful temperature range.[70,71] The electrochemical stability of today's carbonate based electrolytes limits the useful capacity of both positive and negative electrodes. The energy of the highest occupied molecular orbital (HOMO) and the lowest unoccupied molecular orbital (LUMO) determine the thermodynamical stability window of the electrolytes. Based on the HOMO energy, cathode potentials above 4.7 V lead to oxidation and the cathodic limit due to the LUMO is as high as 1.0 V.[72] From a thermodynamic point of view, the cathodic limit should rule out the

use of graphite as a negative active material but the formation of a solid electrolyte interphase described in the next section provides metastability, allowing operation over thousands of cycles and many years of storage.[73] On the other hand, the practical anodic limit of commercialized lithium ion cells is well below 4.7 V, because surface reactions could be observed already at 4.3 V[74] and the anodic stability decreases above room temperature.[73] Interestingly, some studies point to the possibility of expanding the potential window even beyond 4.7 V by optimizing the stability of the positive electrode.[75] The development of new electrolytes is a very active field and makes use of the vast possibilities of inorganic and organic chemistry. The resulting variety exceeds the scope of this work and interested readers are directed to the comprehensive review by Xu.[70]

Also, additives help improving the protective films on the electrodes, the fire resistance and many other properties.[71,76,77,78,79] Interestingly, utilizing multiple additives in small quantities appears to be a promising method to increase the cycle life of modern batteries.[76] For example, linear esters help avoiding gelling at low temperatures[80] while polymerizable additives such as those shown in Figure 2.6 enhance the solid electrolyte interphase discussed in the next pages. Tailoring the solid electrolyte interphase using different additives helps improving impedance and aging properties of modern lithium-ion cells.

Cold cranking enhancers

Ethyl propionate

Propyl butyrate

Polymerizable additives

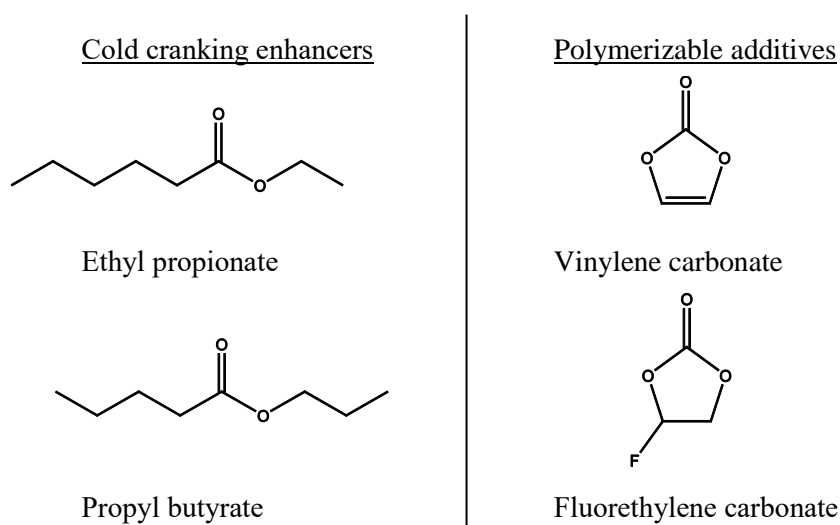Vinylene carbonate

Fluorethylene carbonate

Figure 2.6 Examples of popular additives. Polymerizable additives are added to enhance solid electrolyte interphase formation. Cold cranking enhancers are added to decrease viscosity at low temperatures. Interestingly, fluorethylene carbonate also improves the low temperature behavior.[78]

2.3 Aging of LIBs

Lithium-ion battery aging is a complex process with several influencing degradation mechanisms as shown by recent studies on commercial batteries.[8,9,81,82–84] The importance of battery life to many applications is reflected in a variety of studies. Recent reviews[3,85,86] provide a good overview on aging processes.

The lion's share of overall lithium loss in lithium-ion cells is generally attributed to the solid electrolyte interphase on the negative electrode, while passive films on the positive electrode are rather associated to rising resistance.[9,87] Loss of lithium is mainly associated to the loss of intercalated lithium, but also the lithium ions of the conductive salt $LiPF_6$ may be consumed. The loss of conductive salt does not influence capacity directly, but leads to increased diffusion resistance in the electrolyte and contributes to the formation of passive films.[88,89] In the following sections a concise overview of governing loss mechanisms is given.

2.3.1 Interface reactions on the graphite electrode and formation of the Solid Electrolyte Interphase

Both lithium and lithiated graphite electrodes operate outside the electrochemical stability window of the carbonate solvents presented in the previous section. Only by the formation of a protective film on the negative electrode's surface, metastability is achieved.[3,90] The presence of this solid electrolyte interphase (SEI) can therefore be considered the stroke of luck of lithium-ion technology. An ideal SEI impedes any further reaction of electrolyte with the electrode by blocking electrons and all mass transport but that of lithium ions.[88]

Reductive processes on the surface lead to the formation of organic and inorganic bicarbonates and radicals of which some examples are shown in Figure 2.7. The mechanisms behind the formation of those species are contested and it is not clear if one-electron or two-electron reactions dominate.[88] Still, the reductive formation of lithium alkyl carbonates and subsequent polymerization is generally accepted.[88] Also, radical intermediates that may lead to the formation of said bicarbonates were observed in electron paramagnetic resonance studies on irradiated carbonate solutions. [91,92] It was further shown in the same studies that radicals can quickly form secondary radicals, recombine and disproportionate. Interestingly, radical and anionic polymerizations may take place in parallel, yielding complex, branched oligomers and polymers on the graphite surface.[92]
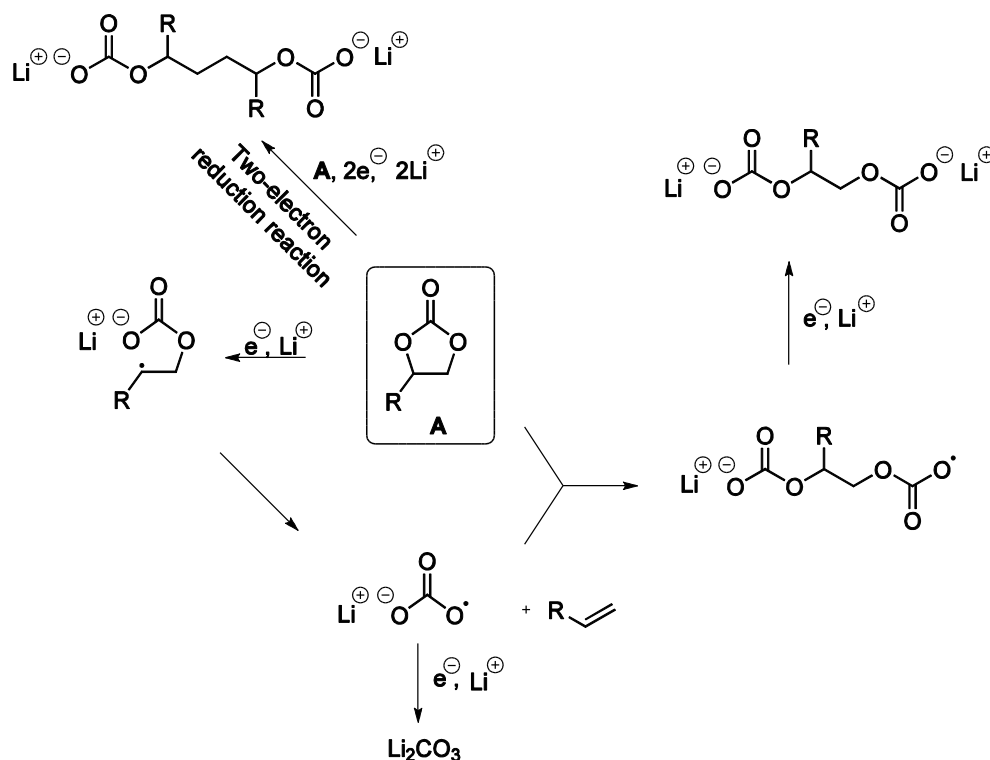
Figure 2.7 Possible reactions and intermediates leading to bicarbonate formation. The mechanisms of carbonate formation and subsequent oligomerization are still disputed as both one- and two-electron reactions may lead to the same products. R = CH$_3$, H.

While some reaction products are solvated by the electrolyte, inorganic salts as well as oligo- and polymers deposit on the graphite surface.[88] The resulting interphase hinders further reactions but maintains sufficient lithium transfer.[90,93] However, the formation of the SEI is accompanied by lithium loss. More so, the reductive processes never stop completely as the SEI is not completely impermeable and may also crack upon cycling.[94]

Studies on electrolyte aging have demonstrated the impact of carbonate and LiPF$_6$ decomposition.[95,96] The reaction of LiPF$_6$ with traces of water leads to the formation of lithium fluoride, fluorinated phosphates and their acidic forms which react with active materials and solvents, thereby leading to their degradation.[95] Except the reaction to lithium fluoride and phosphorus trifluoride,[88] typical degradation reactions of LiPF$_6$ do not take place on the negative graphite electrode but with impurities in the electrolyte[88] and on the positive electrode's surface[97].

The mitigating effects of additives such as those shown in Figure 2.6 have been thoroughly described in literature and the course of action of vinylene and fluorethylene carbonate is well understood.[76,79,88]

Using ab initio calculations[98] and experiments[99] it was shown that vinylene carbonate is reduced more readily than the popular carbonates shown in Table 2.2. The generation of a passive film at early stages of formation makes the use of propylene carbonate together with graphite electrodes possible by inhibiting its cointercalation into graphite and the resulting exfoliation reactions.[88] Fluorethylene shows comparable reactivity to vinylene carbonate. Furthermore, vinylene carbonate enhances the radical polymerization of ethylene carbonate. The reduction of fluorethylene carbonate yields lithium fluoride upon reduction which contributes to the formation of a stable passive film during the first cycle, a property especially useful in negative electrodes containing silicon.[100]

The complexity of the reactions that create the SEI is reflected in the strong dependence of SEI quality on cell formation strategies. As the quality of the SEI strongly determines the aging properties of the cell it is desirable to optimize the formation cycles to obtain a closed film. Besides temperature and wetting, the formation of the SEI is mainly influenced by the current densities and potentials on the graphite surface.[88] The SEI is mainly formed in a potential window between 0.8 V vs. Li/Li^+ and 0.3 V vs. Li/Li^+.[88] Unfortunately, the morphology of the formed film is current-dependent[101] and the SEI becomes increasingly porous at higher current density, which makes it necessary to use slow charging rates.[88] Also, changes to formation protocol may cause higher irreversible capacities and charge transfer resistances.[102] Due to the complexity of the lithium-ion cell formation process, it is generally considered a trade secret and little information on commercial procedures is known, a fact that complicates the comparison of different aging studies.[103]

The SEI deposited during formation does not remain static during cell operation. Especially at elevated temperatures, the metastable organic compounds formed by reduction and subsequent secondary reactions are further transformed.[3,102,104] The reactions involved lead to further capacity loss[105] and the resulting inorganic compounds such as lithium carbonate and lithium fluoride form a more stable SEI with improved thermal behavior[106] and solvent impermeability but also increased resistance to lithium transfer.[3]

2.3.2 Surface reactions on the positive active material

Just as is the case with the negative electrode, aging research on the positive electrode also focuses on the interface to the electrolyte, as the surface reactions taking place dominate the progression of capacity and power fade.[3,107]

Nonetheless, the processes on layered oxides differ significantly from those observed on the graphite electrode. In contrast to graphite, positive electrodes such as those based on NCM do not form an SEI as such, but a thin and permeable interphase that is often referred to as a solid permeable interphase (SPI).[87,107,108] Interestingly, both the SEI and SPI contain LiF embedded in an organic matrix and NCM also suffers from first cycle irreversible capacity loss. Due to the difficulties in analyzing the origin of the first cycle irreversible capacity loss, it is still disputed and has been attributed to surface reactions[57] but also to sluggish kinetics[109].

Just as the SEI on graphite is a dominant source of capacity loss, the SPI is the main source of power loss.[3,108] Compared to LCO, significant changes to NCM's lattice take place at higher degrees of delithiation which allows for a higher practical capacity use in NCM based cells.[110] Still, the degree of delithiation is also limited by electrode potential and thus growth of the SPI.

Also, products of electrolyte oxidation and transition metal dissolution are known to diffuse to the negative electrode were they deposit again and change the properties of the SEI.[87,109,111,112] For example, deposited manganese has been shown to deteriorate the kinetic properties of the SEI and to catalyze electrolyte decomposition on the negative electrode.[112–114]

2.3.3 Mechanical Aging

The intercalation of lithium in NCM and graphite leads to volume changes of 3 % and 10 %, respectively.[87,115] The cyclic expansion and contraction of lithiated graphite leads to mechanical damage that has been reported to be most severe upon deep delithiation of the graphite electrode.[116,117] The constant mechanical changes at the surface have been found to induce constant growth of the SEI, therefore causing additional lithium loss.[118]

Mechanical aging also leads to loss of contact of active materials. The effects of cyclic expansion and contraction are schematized in Figure 2.8. Delamination and particle insulation lead to lithium and active material loss when binders fail to accommodate the stress caused by cyclic expansion.[3,119] As particles grow they are displaced and during the consecutive contraction some particles may not return to their previous location. The newly exposed surfaces may then grow an SEI that electrically insulates them even if the particles come into mechanical contact later. Under some conditions

microcrack formation may lead to the disintegration of particles and subsequent contact loss and SEI formation.[120] Again, the newly formed SEI may then permanently insulate the particle.
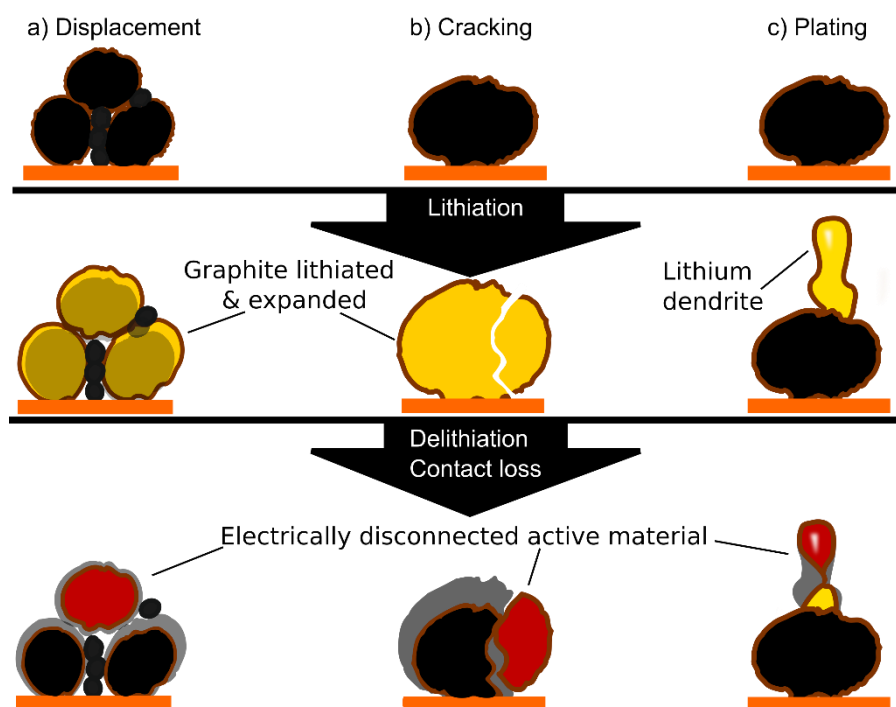
Figure 2.8 Main mechanical aging mechanisms on materials level. Formation of lithiated graphite and plated lithium (yellow) from unlithiated graphite (black) leads to particle growth. a) displacement, as well as b) cracking and c) plating and lithium dissolution upon discharge disconnects active material and lithium particles (red).

Finally, lithium plating is often accompanied by heavy losses of active lithium due to the shrinking of the base of dendrites and whiskers that may then cut off the tip of the lithium protrusions.[121] The extremely reductive nature of lithium metal then causes the formation of a dense SEI that disconnects the remaining lithium metal particles completely from the negative electrode. While counterintuitive, incomplete stripping of lithium metal is a well-described effect of the solid electrolyte interphase[15,17,90,122] and has been shown to lead to effective loss of lithium on model substrates[121,123] and on graphite electrodes in cycled batteries.[4,86,124,125]

Furthermore, graphite expansion may lead to increased pressure in some cell designs. The resulting compression may cause damages due to separator deformation.[41,125] On the other hand, uncompressed electrode stacks may have a tendency to delaminate.[41] Therefore, the optimal pressure depends on the cell design and the elastic moduli of separators and binders in wetted state.

Besides the mechanical effects of cycling, the mobile applications of lithium-ion cells are often associated with considerable external accelerating forces.[11,126,127] As of

today, vibrations and shocks are mainly considered in terms of a hazard occurring during transportation of cells and battery packs[128,129] but test protocols for batteries in electric vehicles have also been normalized.[130] Hooper and Marco reviewed the test protocols UN38.3,[129] ECE R100,[131] J2380[132] and BS62660[133] and concluded that their implicit assumptions on frequency distribution and peak loads do not reflect real conditions.[127] For example, the exclusion of frequencies lower than 7 Hz, does not seem to be backed up by real world data. Martin *et al.* compared the vibrational loads found in conventional cars and electrified vehicles.[126] In their work, they also pointed out the significance of excitation frequencies below 7 Hz in real use cases. Hooper et al. investigated cylindrical cells in a long term vibration study that simulated an automotive lifecycle and found considerable degradation, especially when resonance frequencies were exited.[134]

2.3.4 Capacity projections based on cyclic and calendric aging

In aging models, the capacity fade is mainly attributed to the formation of passive films, leading to lithium loss and resistance increase, as both negative and positive electrodes are usually operated outside the electrolyte's electrochemical stability window.[3] The calendric capacity fade resulting from passive film formation has been shown to have a square root dependency on time.[9,84,85,135] Nearly linear aging behavior has been reported to be influenced by additional aging factors.[8] It is usually reported that cyclic aging causes linear fading of capacity and square root dependencies on charge throughput are sometimes reported as well.[8,85,136,137]

SEI formation, causing lithium loss and increasing resistance, is reported to be the dominant source of capacity fade. The linear aging model may be used for projections of SEI growth and residual value of aged cells and battery packs, but reports on suddenly increasing aging rates put such projections into question.[8,9,137,138] This increase in aging rate may be connected to lithium plating. Interestingly, one study found the aging rate due to lithium plating to reduce after prolonged cycling.[139] The inflection point has been linked to partially irreversible lithium plating.[9,87] The occurrence of inactive lithium, which is not stripped upon full discharge of the cell, is noteworthy as it shows the possibility of irreversible capacity loss due to local disconnection of parts of the electrodes' electrochemically active materials. As inactive lithium is not in electrical contact to the electrode, it is difficult to be detected by electric means, while it is easily detected by Post-Mortem observation.

2.4 Theory of Ultrasonic probing

2.4.1 Signal generation

When materials are analyzed by ultrasonic behavior it is instructive to investigate their response to signals with different frequencies. At each frequency, properties of the transmitted signal such as amplitude and phase velocity can be used to characterize a material. For good resolution, the utilized signal waveform should have several properties:

- Short, to avoid overlap of different modes.
- Sharp spectral distribution.
- Begin and end with a zero value to avoid inter signal interference.
- Charge balanced, to avoid inter-signal interference.

A signal is called charge balanced, when the currents in positive and negative direction even out to give a net transferred charge of zero. The properties of sharp frequency distribution and short signal length in the time domain are conflicting, because short impulses have broad frequency distributions and vice-versa.[140,141] Therefore, it is useful to use impulses with several oscillations. While several filter windows exist, the Raised Cosine impulse with N oscillations, in short RC_N-impulse, is commonly used in ultrasonic experiments.[140] The RC_N-impulse shown in Equation 4 has an envelope function with a length of $2\pi N/\omega_0$, where ω_0 is the circular frequency.

$$RC_N(t) = \begin{cases} \left[\left\{1 + cos\left(\dfrac{\omega_0\,t}{N}\right)\right\} * cos(\omega_0\,t)\right] for\ |t| \leq \dfrac{N*\pi}{\omega_0} \\ \\ 0\ for\ |t| \geq \dfrac{N*\pi}{\omega_0} \end{cases}$$

Equation 4

With the Fourier transform given in Equation 5, the resulting spectra are available in algebraic form.[140]

$$RC_N(\omega) = (-1)^{N+1} sin\left(\frac{N\pi\omega}{\omega_0}\right) \left\{ \frac{\omega}{\omega^2 - \left(\dfrac{N+1}{N}\right)^2 * \omega_0^2} - \frac{2*\omega}{(\omega^2 - \omega_0^2)} \right.$$
$$\left. + \frac{\omega}{\omega^2 - \left(\dfrac{N-1}{N}\right)^2 * \omega_0^2} \right\}$$

Equation 5

In Figure 2.9 a) spectra and b) impulses with one to five oscillations are shown for a circular frequency of 100 kHz. It is obvious that increasing the number of oscillations improves the spectral resolution while decreasing the time-domain resolution.

Therefore, the number of oscillations N should be optimized for each individual application but values of N= 3 to 5 are often sufficient.
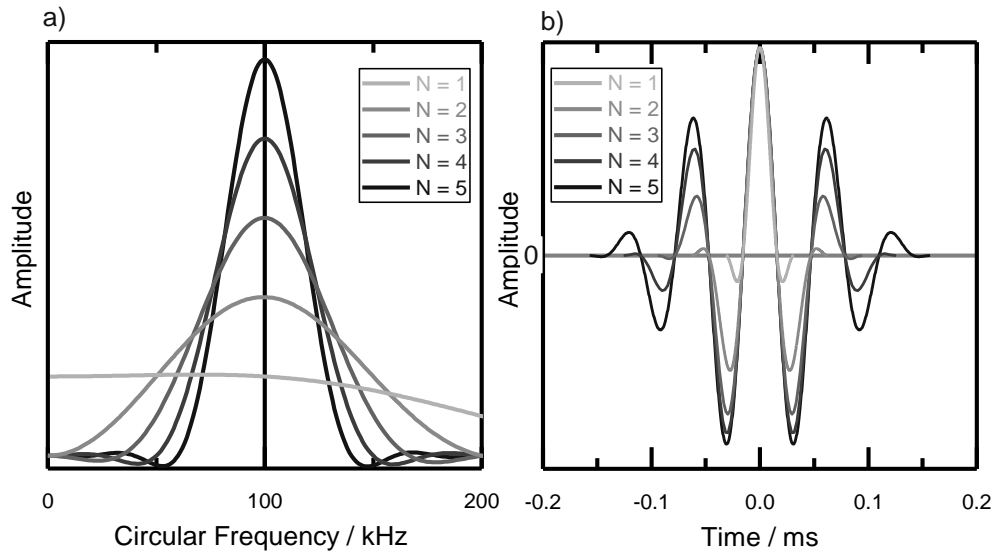

Figure 2.9 RC_N-impulse in a) frequency and b) time domain. The frequency distribution of the RC_N-impulse with $\omega_0 = 100$ kHz becomes sharper when N is increased as the envelope of the RC_N-impulse in the time domain becomes broader.

2.4.2 Propagation of acoustic waves in porous media

Sound can travel through heterogeneous materials in different modes. Acoustic waves can be classified into pressure and shear waves. In pressure waves, the particles are displaced longitudinally, while shear waves are characterized by transversal dislocation. The displacement of particles is illustrated in Figure 2.10.
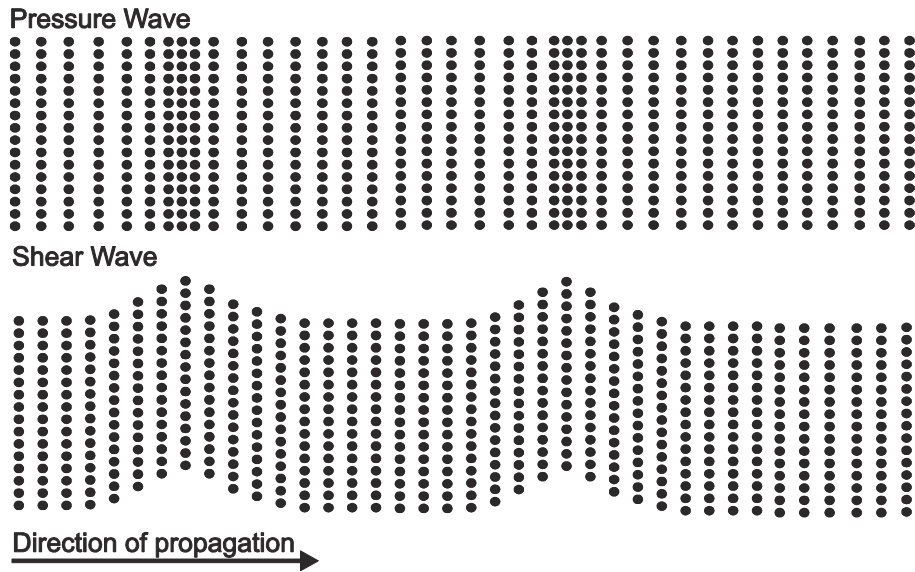
Figure 2.10 Illustration of pressure and shear waves. Pressure waves cause movement in the axis of propagation. Shear waves are characterized by dislocations perpendicular to the direction of propagation.

Treatments of acoustic waves in fluid-saturated porous media are complicated by the relative motion of the porous frame and the fluid. Due to the practical relevance in seismic and medical applications discussed in the introduction, several works have been published. The understanding of acoustics in porous media has been substantially advanced by Biot's "Theory of Propagation of Elastic Waves in a Fluid-Saturated Porous Solid".[142,143] Today it can be considered the standard work in the field of poromechanics. Using several assumptions, Biot showed that three waves exist in the absence of dissipative forces. Those assumptions include the following:

1. "The fluid-saturated porous material is constituted in such a way that the fluid phase is fully interconnected. Any sealed void space is considered as a part of the solid.
2. A so-called representative elementary volume element is defined, which is small compared to the relevant wavelength but large compared to the individual grains and pores of the system. Each volume element is described by its averaged displacement of the solid parts $\mathbf{u}(\mathbf{x}, t)$ and of the fluid parts $\mathbf{U}(\mathbf{x}, t)$.
3. The deformation of the elementary volume element is assumed to be linearly elastic and reversible. This implies that displacements for both fluid and solid phases are small. The governing equations can be represented in their linearized form.
4. The solid is considered to have compressibility and shear rigidity, while the fluid only has compressibility as it is assumed to be a Newtonian fluid: the fluid does not sustain any shear force for static displacements.
5. The solid and fluid are assumed homogeneous and isotropic, and all possible dissipation mechanisms related to the solid itself are not taken into account. Only dissipation due to viscous relative fluid-solid motion is incorporated.
6. Thermoelastic and chemical reaction effects are assumed to be absent and the system behaves adiabatically."[144]

27

Besides a shear wave, two pressure waves are predicted to exist. The amplitudes in solid and fluid of the first pressure wave, further on called "fast wave", are found to be in phase. A second mode with pressure amplitudes of solid and liquid in opposite phases constitutes the slow wave. As this wave can be shown to be slower, it is called the slow wave.

To estimate attenuation, Biot described dissipation by assuming Poiseuille flow in the fluid. The flow of a liquid remains laminar only if the dimensionless Reynolds number Re is sufficiently small.

$$Re = \frac{inertial\ forces}{viscous\ forces}$$ **Equation 6**

Biot established the transition frequency f_t based on a consideration of the quarter wavelength of the boundary layer above an oscillating planar surface. The critical frequency f_t is established based on kinematic viscosity ν and pore diameter d.

$$f_t = \frac{\pi\ \nu}{4\ d^2}$$ **Equation 7**

When this frequency is reached, or surpassed, Poiseuille flow is expected to break down.

To give a rough estimate of the critical frequency in lithium-ion batteries, typical viscosity and pore sizes are used and it is assumed that the pores are completely filled with electrolyte. Now, the standard electrolyte $EC/DMC/LiPF_6$ has a kinematic viscosity of $24\ \mu m^2\ s^{-1}$ at room temperature. Typical particle sizes are $10\ \mu m$ or smaller and electrode thicknesses are of the magnitude of 0.1 mm. Assuming the graphite particles would be spherical and close packed, the biggest pores would have diameter of approximately $4\ \mu m$.[145] Based on this rough estimation the transition frequency is found to be as high as 1.6 Mhz. Therefore, the ultrasonic frequencies utilized in this work can be considered "low" as they are at least one order of magnitude lower than the critical frequency.

As the shear and pressure waves discussed before can be considered to be uncoupled, Biot derived simple formulas based on further approximations valid for frequencies approximately one order of magnitude below the critical frequency. The attribution of the introduced constants to physical values is still a matter of scientific debate.[146] Jocker *et al.* relate the constants to readily accessible parameters.[146] The resulting approximations for the velocities of the shear wave Vs and the slow pressure wave V_{II} can be used to predict the acoustic properties of a range of materials and this thesis is based on the formalism presented by Biot.

As Biot found the deviations of V_I from V_c to be very small at low frequencies, they are assumed to be identical in this thesis.[142]

$$V_I \cong V_c \qquad\qquad \textbf{Equation 8}$$

With the reference Velocity V_c.[142]

$$V_c = \sqrt{\frac{H}{\rho}} \qquad\qquad \textbf{Equation 9}$$

The velocities V_{II} and V_s are calculated based on the parameters listed below, were σ denotes parameters defining elastic properties, γ parameters of dynamic properties, f the frequency, f_c the characteristic frequency and Nn the shear modulus of the drained porous matrix.[142]

$$V_{II} = V_c \sqrt{2\frac{f}{f_c}\frac{\sigma_{11}\,\sigma_{22} - \sigma_{12}^2}{\gamma_{12} + \gamma_{22}}} \qquad\qquad \textbf{Equation 10}$$

$$V_s = \sqrt{\frac{N_n}{\rho_{11}\left(1 - \frac{\rho_{12}^2}{\rho_{11}\,\rho_{22}}\right)}} \qquad\qquad \textbf{Equation 11}$$

The mass of solid per unit volume ρ_1 , mass of fluid per unit volume ρ_2, and the mean density ρ are given by the following equations, with the porosity β and the densities of fluid ρ_f and solid ρ_s,[142]

$$\rho_1 = (1 - \beta)\rho_s \qquad\qquad \textbf{Equation 12}$$
$$\rho_2 = \beta\,\rho_f \qquad\qquad \textbf{Equation 13}$$
$$\rho = \rho_1 + \rho_2 \qquad\qquad \textbf{Equation 14}$$

the mass coefficients ρ_{11} and ρ_{22}[142] as well as the coupling coefficient ρ_{12}[146] with the tortuosity α,

$$\rho_{11} = \rho_1 - \rho_{12} \qquad\qquad \textbf{Equation 15}$$
$$\rho_{22} = \rho_2 - \rho_{12} \qquad\qquad \textbf{Equation 16}$$
$$\rho_{12} = -(\alpha - 1)\,\beta\,\rho_f \qquad\qquad \textbf{Equation 17}$$

the effective porosity, with bulk moduli of fluid k_f, solid k_s and porous drained matrix k_b,[146]

$$\beta_{eff} = \beta + \frac{k_f}{k_s}\left(1 - \beta - \frac{k_b}{k_s}\right) \qquad\qquad \textbf{Equation 18}$$

the characteristic frequency containing the coefficient b.[142]

$$f_c = \frac{b}{2\,\pi\,\rho\,(\gamma_{12} + \gamma_{22})}$$

Equation 19

The coefficient b being a function of the dynamic viscosity μ of the fluid, the porosity β and Darcy's coefficient of permeability k,[142]

$$b = \mu\frac{\beta^2}{k}$$

Equation 20

the parameters of dynamic properties.[142]

$$\gamma_{11} = \frac{\rho_{11}}{\rho}$$

Equation 21

$$\gamma_{22} = \frac{\rho_{22}}{\rho}$$

Equation 22

$$\gamma_{12} = \frac{\rho_{12}}{\rho}$$

Equation 23

As well as the parameters defining elastic properties which are based on the Biot's parameters A, P, Q, R and H which correspond to the Lamé coefficients.[142,146]

$$\sigma_{11} = \frac{P}{H}$$

Equation 24

$$\sigma_{22} = \frac{R}{H}$$

Equation 25

$$\sigma_{12} = \frac{Q}{H}$$

Equation 26

Finally the Biot's coefficients are defined by the following equations.[146]

$$A = k_b - 2\frac{N_n}{3} + \frac{k_f}{\beta_{eff}}\left(1 - \beta - \frac{k_b}{k_s}\right)^2$$

Equation 27

$$P = A + 2\,N_n$$

Equation 28

$$Q = \frac{\beta\,k_f}{\beta_{eff}}\left(1 - \beta - \frac{k_b}{k_s}\right)$$

Equation 29

$$R = \frac{\beta^2}{\beta_{eff}}k_f$$

Equation 30

$$H = P + R + 2\,Q$$

Equation 31

The predictions of acoustic velocities in fluid filled porous media obtained by Biot's theory have been validated in several applications.[147] Their applicability, even in stratified porous media,[148,149] makes them useful for battery applications. Estimations of attenuation derived from the same theory are generally less successful. This can be explained by difficulties in defining the correct parameters[150] and competing loss mechanisms such as squirt-flow,[150,151,152] wave induced flow on larger scales[153] and viscous shear relaxation.[150,154] Especially in stratified media, the transmitted signal can be highly dependent on the ratio of wavelength and the periodic length of the material.[155]

2.4.3 Dispersive effects due to mesoscopic heterogeneities.

Theoretical studies predict heavy variations depending on the type of stratifications, leading to transitional regimes with abruptly increasing or decreasing attenuation[155,156] as well as attenuation peaks.[152,157] In slabs periodic effects can be observed.[146] Jocker *et al.* investigated the transmission of acoustic pulses through stratified, fluid-filled porous materials.[146] In their work, the wavelength λ_I of Biot's fast wave was of the same order of magnitude as the mean layer thickness *l*. By varying the frequencies, Jocker showed that the transmitted amplitudes of this wave vary periodically with the ratio $l\,\lambda_I^{-1}$. Jocker *et al.* concluded from their study that: "Since the slow compressional wave has the shortest wavelength, scattering effects will first affect this wavetype before affecting others."[146] Carcione *et al.* investigated the transition between nondispersive behavior of layered porous media as an equivalent medium to highly dispersive behavior upon wavelength variation.[155] Based on numerical analysis, they give estimations for the occurrence of a transitional regime with drastically changing attenuation:

1. "Depending upon the relation of wavelength to layer thickness, a stratified medium induces dispersion, scattering, and a smoothed transversely isotropic behavior.
2. The minimum ratio of wavelength to layer thickness for the long-wavelength approximation to be valid is highest in the midrange of compositions, as found recently in laboratory experiments.
3. The minimum ratio depends on material compositions through the reflection coefficients between the constituents. For instance, for epoxy-glass it is around R = 8, and for sandstone-limestone (which has a lower reflection coefficient) it is between R = 5 and R = 6.
4. 2-D numerical tests reveal that the more anisotropic the equivalent medium, the higher the minimum ratio. […]"[155]

While both theoretical and experimental studies show a great variety in observed attenuation effects, it can be concluded that effects on different length scales may lead to pronounced changes in transmitted and reflected signals due to changes in properties such as porosity, permeability or elastic modulus, especially in the layers with the slowest phase velocity.[149] As has been shown in Section 2.2.1, these properties are known to vary greatly upon lithiation and delithiation of graphite.

3   Experimental[1]

3.1   Test samples

Different lithium-ion cells with graphite electrodes were used to investigate the chemo-mechanical interactions of the graphite electrode.

In the cyclic aging tests and vibration studies, lithium-ion cells with Lithium-Nickel-Cobalt-Manganese oxide (NCM) based positive and graphite based negative electrodes were investigated. The cylindrical Molicel IHR18650A by E-One Moli Energy Corp. has a nominal capacity of 1.95Ah.

For vibration studies, pouch cells with a nominal capacity of 0.7 Ah were investigated additionally to compare the behavior of pouch and cylindrical cells under vibrational stress. To ensure unbiased interpretation of the results, the analytical team at Fraunhofer ISC handled the cells based on a coded name and was not informed on the history of each cell before the study was finished.

To develop a new method to determine the state of charge based on ultrasonic detection of graphite's volume expansion commercial cells with state of the art energy and power density were chosen. While the method was tested on different pouch type cells, all results shown in this work were obtained from high power pouch-type cells from Conrad-energy. The cells with the part number 683562-1200-20C had a nominal capacity of 1.2 Ah and dimensions of approximately 7 mm x 36 mm x 54 mm.

Lithium iron phosphate based pouch cells with graphite electrodes were gathered from a dissected small battery pack for further testing of ultrasonic detection of state of charge. The cells had a nominal capacity of 2 Ah and dimensions of approximately 6 mm x 42 mm x 120 mm.

All cells called pristine in this article have undergone formation procedures at the discretion of the manufacturer.

---

[1] This chapter has been published in parts under creative commons licence CC BY 4.0: T. C. Bach, S. F. Schuster, E. Fleder, J. Müller, M. J. Brand, H. Lorrmann, A. Jossen, G. Sextl, Nonlinear aging of cylindrical lithium-ion cells linked to heterogeneous compression, Journal of Energy Storage (2016), in press, http://dx.doi.org/10.1016/j.est.2016.01.003.

3.2 Cell test routines

In this thesis, cells were cycled by constant current (CC) and constant voltage (CV) steps as exemplarily depicted in Figure 3.1. Charging and discharging was performed by CC steps with a fixed current $I_{ch/dis}$ until either the upper cutoff voltage U_{max} or the lower cut-off voltage U_{min} was reached. In some cases, a CV step was applied, which consisted of holding the voltage until the magnitude of the current decreased below $|I|_{min}$. Finally, open cell voltage (OCV) steps between half cycles allowed the cells to relax for the time t_{OCV}. To give a quick indicator of the timescales, the currents are given in C, which is defined as follows:

$$1\,C = \frac{I}{\frac{Q_{nominal}}{1\,Ah}} \qquad \textbf{Equation 32}$$
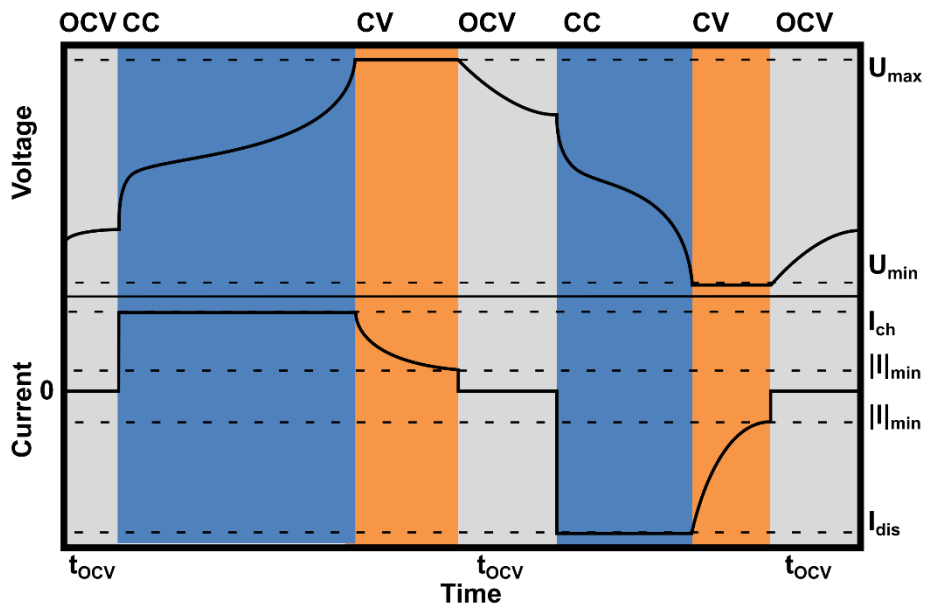

Figure 3.1 Schematic of defining parameters in cycling protocols. The cycling protocols utilized in this thesis can be defined by few parameters. This schematic represents the case of CCCV charge and discharge with rest periods between each CCCV step.

Inhomogeneous aging behavior was investigated in cells cycled at the Institute for Electrical Energy Storage Technology, Technische Universität München. The Molicel IHR18650A were cycled in climate chambers set to 25 °C. As shown in the flow chart depicted in Figure 3.2 a), each full cycle consisted of CC charging at 0.5 C and CC discharging with 1 C between 3.0 V and 4.2 V.

Vibration and shock testing was carried out at the Institute for Electrical Energy Storage Technology, Technische Universität München and at TÜV SÜD Battery Testing GmbH. Details on the experimental setup and electrical testing are given in a joint publication.[11]
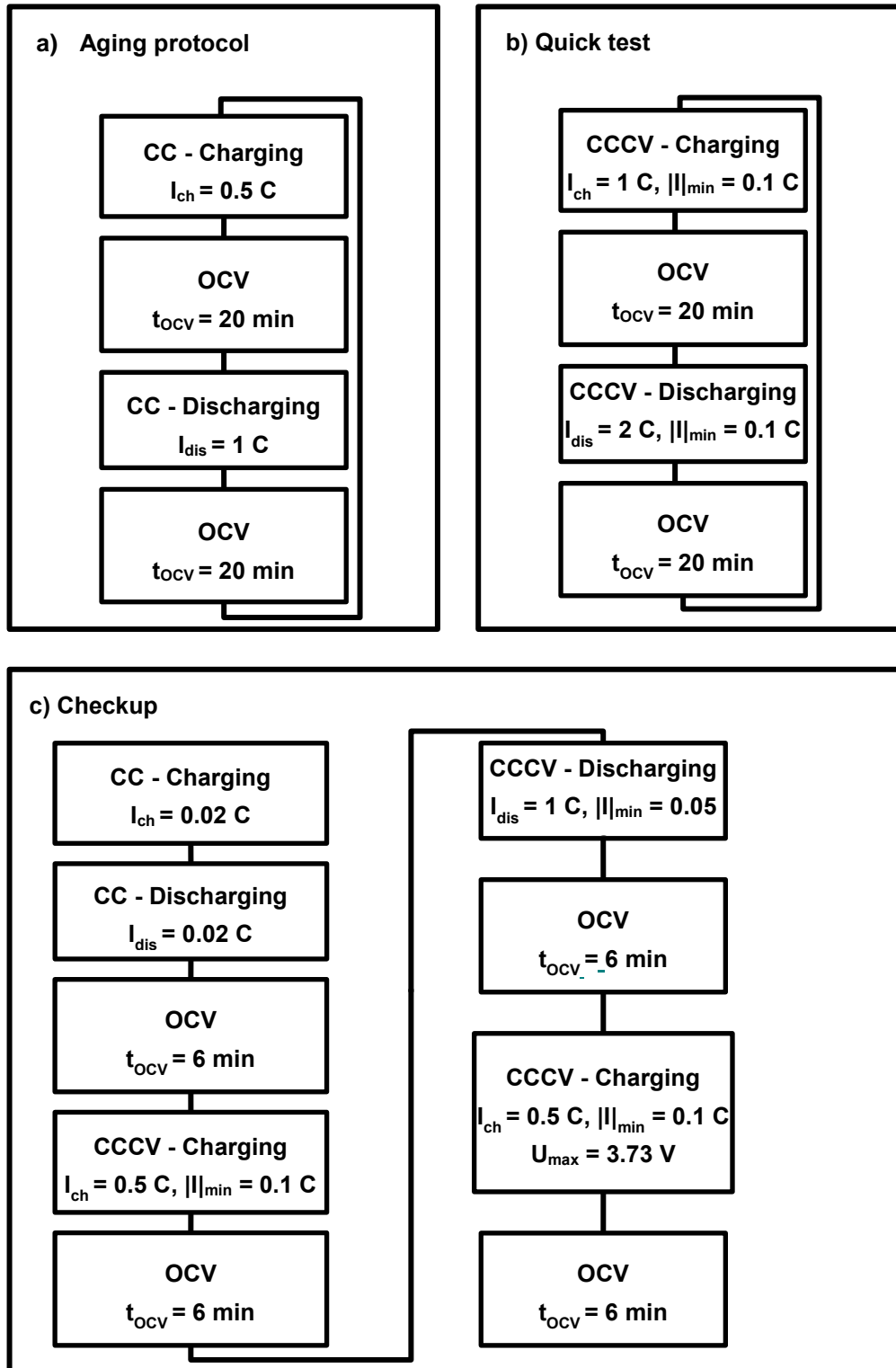
a) Aging protocol

CC - Charging
$I_{ch} = 0.5$ C

OCV
$t_{OCV} = 20$ min

CC - Discharging
$I_{dis} = 1$ C

OCV
$t_{OCV} = 20$ min

b) Quick test

CCCV - Charging
$I_{ch} = 1$ C, $|I|_{min} = 0.1$ C

OCV
$t_{OCV} = 20$ min

CCCV - Discharging
$I_{dis} = 2$ C, $|I|_{min} = 0.1$ C

OCV
$t_{OCV} = 20$ min

c) Checkup

CC - Charging
$I_{ch} = 0.02$ C

CC - Discharging
$I_{dis} = 0.02$ C

OCV
$t_{OCV} = 6$ min

CCCV - Charging
$I_{ch} = 0.5$ C, $|I|_{min} = 0.1$ C

OCV
$t_{OCV} = 6$ min

CCCV - Discharging
$I_{dis} = 1$ C, $|I|_{min} = 0.05$

OCV
$t_{OCV} = 6$ min

CCCV - Charging
$I_{ch} = 0.5$ C, $|I|_{min} = 0.1$ C
$U_{max} = 3.73$ V

OCV
$t_{OCV} = 6$ min

Figure 3.2 Flow charts of cycling protocols for a) aging, b) quick test and c) checkup. Unless otherwise stated, the voltage limits U_{min} and U_{max} were set to 3.0 V and 4.2 V, respectively.

The constant current, constant voltage scheme shown in Figure 3.2 b) was used for a quick test to evaluate the vulnerability towards plating and for thermography. Both charge and discharge procedures contained constant voltage phases to exert maximal stress. The maximum permissible conditions as described by the manufacturer's datasheet were used. The charging current was chosen to be 1 C, while the discharge current was set to 2 C. Constant Voltage steps at 3.0 V and 4.2 V were maintained until the current dropped below 0.1 C for more than one second. Ambient temperature was held at 20 °C.

Prior to destructive analysis, cells were characterized with a 0.02 C full cycle between 3.0 V and 4.2 V, as well as a checkup procedure shown in Figure 3.2 c). The 18650 cells were discharged to 3.0 V with a constant voltage step held until the current dropped below 0.1 C. Then, they were opened in a glovebox with controlled argon atmosphere.

3.3 Post-Mortem electrochemical analyses
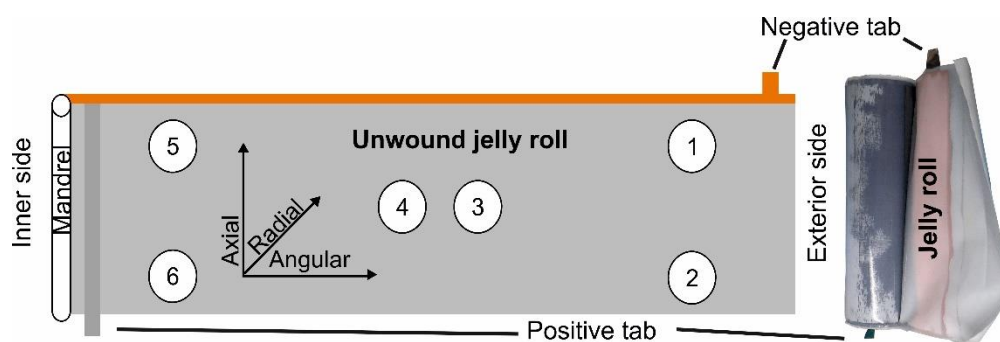
Figure 3.3 Sample positions for spatially resolved electrochemical analysis. The schematic representation of the unwound jelly roll shows the sample positions for spatially resolved electrochemical analysis on the unwound jelly roll. A partially unwound real jelly roll is shown for orientation. The schematic representation is not to scale.

For locally resolved electrochemical characterization, small test cells with reference electrodes were constructed from different parts of the jelly roll. Using a hollow punch, samples of 18 mm diameter were taken from the locations shown in Figure 3.3 from negative and positive electrodes, respectively. By combining cell identification and sample location, an unambiguous nomenclature is provided. Samples are named by the letter (A, B, C) of the respective cell and the number of the sampling location (1-6). The active material coating was scratched off on one side of the electrode discs to contact the current collector. The coordinate system in Figure 3.3 shows the naming conventions used for directions. Based on the cylindrical form of the cell, the direction of the mandrel, around which the electrode is wound, is called axial. The vector pointing through the electrode layers is called radial and the vector parallel to the long side of the electrode is called angular.

The electrode discs obtained where used to construct laboratory cells with a glass fiber separator, standard electrolyte and a lithium reference as shown in Figure 3.4. Commercial three-electrode laboratory cells (El-Cell Ref) were used. A 1.5 mm thick glass fiber separator was necessary for the placement of a reference electrode. In contrast, the separator in the original cell has a thickness of only 25 μm. As the separator was one order of magnitude thicker than the one in the commercial battery, diffusion overpotentials differed. This error was limited by applying low current densities only, therefore minimizing this systematic error. A standard electrolyte, containing 1 mol l^{-1} $LiPF_6$ in 1:1 EC:EMC (Selectipur LP50, MERCK) was used for laboratory cells. These cells were cycled on a Maccor Series 4000 multichannel galvanostat. The same 0.02 C full cycle between 3.0 V and 4.2 V as used for the original cells was applied to the test cells. Using an auxiliary voltmeter, the voltage of the negative electrode with respect to the lithium metal reference electrode was

monitored. By controlling test cells in the same way as original ones and keeping current densities low, results from test cells could be used to understand processes in the original cell.
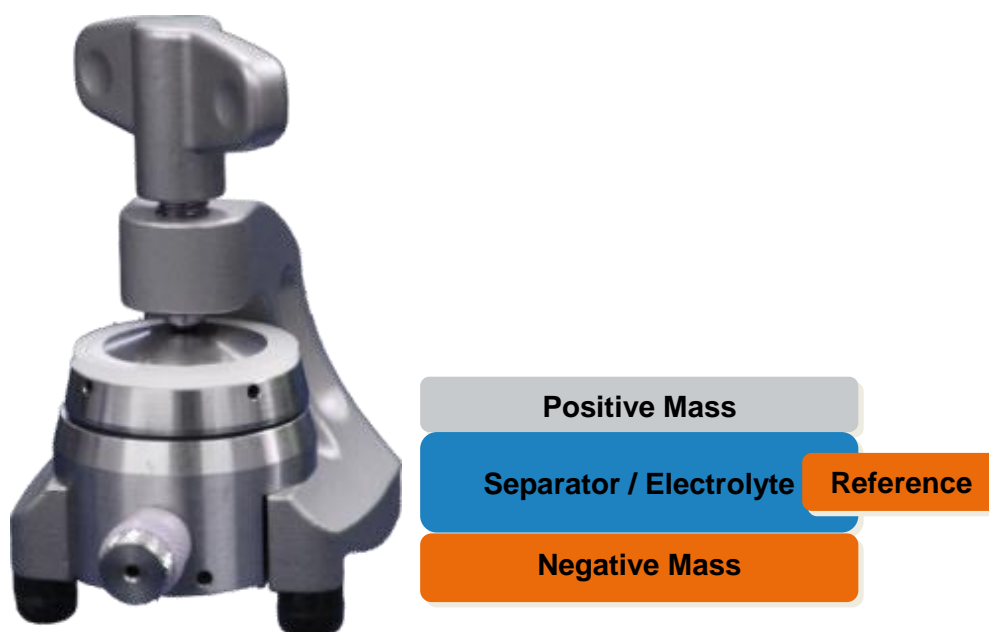

Figure 3.4 Electrode setup used in the laboratory cells. A photograph of the cells used is shown on the left. A schematic representation of the electrode setup is shown on the right.

Charge and discharge behavior of the overall cell and individual electrodes are represented using incremental capacity analysis, a method providing figures very similar to cyclic voltammetry. Incremental capacity was calculated using the differential quotient of the charge Q and the voltage U with respect to the time t:

$$Incremental\ capacity\ =\ dQ\ dU^{-1}$$
$$=\ [Q(t_2) - Q(t_1)][U(t_2) - U(t_1)]^{-1}$$

Equation 33

with $\quad U(t_2) - U(t_1) \geq dU_{min}.$

When dU is calculated directly from the time series, small voltage increments combined with measurement noise may lead to amplified noise.[158] Therefore a minimum potential increment of dU_{min} = 5 mV was set for cathode and anode incremental capacity analyses. Accordingly, the full cell minimum increment was set to dU_{min} = 10 mV to obtain a comparable number of increments. The minimal increments were ensured for each step by increasing the time step until the condition was met.

3.4 Materials characterization

Preparation for electrochemical analysis and scanning electron microscopy (SEM) was entirely carried out under argon and samples for SEM were transferred under vacuum without washing steps or contact to air using a custom sample holder. Samples for inductively coupled plasma optical emission spectroscopy (ICP-OES) and X-ray diffraction (XRD) were handled in air.

Samples for ICP-OES from both negative and positive electrodes were taken, washed and dried under argon atmosphere. Washing was performed by soaking samples in dimethyl carbonate (MERCK SelectyLite™) for 60 minutes, renewing the dimethyl carbonate solution and soaking for another 30 minutes. The samples were then dried under vacuum using the antechamber of the glovebox and weighted under argon atmosphere. Samples were then exposed to air and dissolved using *aqua regia*. *Aqua regia*, a strong oxidizing acid, was obtained by freshly mixing three volume parts of concentrated hydrochloric acid (fuming 37 %, for analysis, MERCK) with one volume part of concentrated nitric acid (concentrated 65 %, p.a., Th. Geyer). The samples were stirred in *aqua regia* overnight. All metal parts and active materials were oxidized and dissolved so that only graphite and binder remained as solid residue. The solid residue was filtered off and weighted. The obtained clear solutions containing the metal species were then analyzed using a Varian Vista-PRO optical emission spectrometer. ICP-OES-measurements were run using a glass cyclonic-action spray chamber with glass concentric nebulizer for the sample introduction and a radially viewed plasma. The interpretation of signals was performed using repeat measurements of samples and calibration standards prepared in 1 % hydrochloric acid. The wavelengths used for the analysis of element concentrations are shown in Table 3.1. The output was averaged over all monitored wavelengths.

Table 3.1 Wavelengths used for ICP-OES Analysis.

Element	Wavelengths monitored / nm
Lithium	610.4
Manganese	257.6, 259.4, 260.6, 294.9
Nickel	216.6, 221.6, 230.3, 231.6
Cobalt	228.6, 230.8, 237.9, 238.9

XRD of positive electrode samples was performed under air using an Empyrean diffractometer produced by PANalytical. The Cu Kα line was used. Polarization microscopy was used as a standard method to examine changes in the crystallinity of polymers.[159] An Aristomet light microscope of the Leitz Messtechnik GmbH equipped with a polarizer, an analyzer and a first order retardation plate was used to visualize changes in birefringence of the investigated separator materials.

3.5   Non-destructive imaging

Temperature gradients were investigated using a FLIR T650 thermal camera. As the battery was covered by polymer based shrink wrap, its emissivity was estimated to be 0.95. Thermal images and temperature values from three points on the surface were collected while the battery was cycled.

To detect damages in lithium-ion cells exposed to different mechanical vibrations and shocks, they were inspected by computed tomography. Before and after vibration tests full 3-D volume information was collected by computed tomography with a resolution of 20 μm or better. Measurements were performed by Jan-Marcel Hausherr on a custom-built tomograph at the Fraunhofer Center for High-Temperature Materials and Design. The tomograph consists of a 225 kV X-Ray source, a movable rotating stage and a flat-panel detector with a resolution of 2048 x 2048 pixels.

The 3D-Volumina obtained from cells before and after vibration were overlaid and compared to detect displacements and damages.

3.6   Ultrasonic detection of state of charge

3.6.1   Laboratory measurements

To probe the changes in ultrasonic transmission due to intercalation and deintercalation of lithium in graphite, short ultrasonic pulses were used. Raised cosine filtered impulses so called RC_N-Impulses were used because of their favorable frequency and time domain properties. Separate transducers were used for signal generation and detection of the answer. Their placement is shown in Figure 3.5.

The piezo elements *"Piezokeramisches Element EPZ-Serie - 6400 Hz"*, were obtained from Conrad Electronic SE. Key specifications of the transducers are listed in Table 3.2.

Table 3.2 Manufacturer's specifications of utilized piezo transducer. Specifications of the piezo element *"Piezokeramisches Element EPZ-Serie - 6400 Hz"*, "EPZ-20MS64W", Best.-Nr.:710385-05

Materials	Ceramic on brass
Impedance	350 Ω
Resonance frequency	6400 Hz
Outer Diameter	20 mm
Electrode Diameter	15 mm
Thickness	0.19 mm
Capacitance	13 nF

The transducers were glued centrally on the large surfaces of the prismatic cells using the epoxy resin based glue "*UHU plus endfest 2-K-Epoxidharzkleber*".
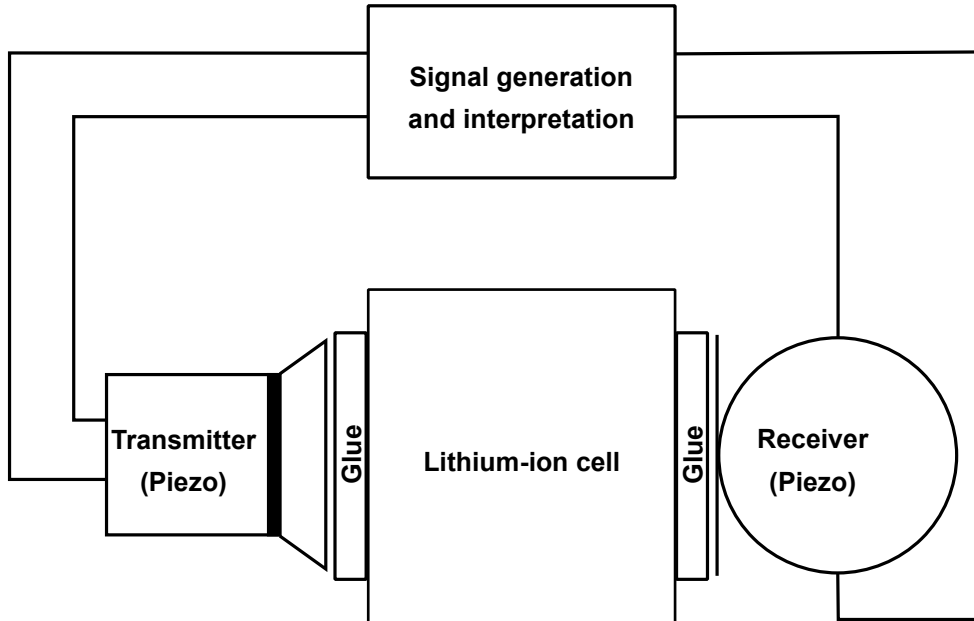

Figure 3.5 Schematic of the setup used for ultrasonic probing. Transmitter and receiver are placed in the center of the large faces of the cell to avoid edge effects. The piezo elements used as transducers are glued to the surface for improved reversibility.

Using a custom ultrasonic sending and receiving unit with variable gain and digital control of the waveform, as well as the proprietary software CANWARE08_ISC, an RC$_N$ impulse, with the number of oscillations $N = 5$ was then sent by the transducer acting as a microphone and transmitted through the battery. The transmitted response was received after hardware triggering by the transducer placed opposite to the piezo buzzer creating the signal pulse. The sent signal was sampled with 18.75 MSa s^{-1} and amplified with 18 dB. The received answer signal was recorded from 9,6 µs before the trigger and 1 ms after the trigger and was amplified with a gain of 18 dB and a sample rate of 4.17 MSa s^{-1}.

The pouch-type cells from Conrad-energy were charged and discharged in steps of 20 % of nominal capacity using a current of 2 C and 4 C, respectively. The lithium iron phosphate based pouch cells were also discharged in steps of 20 % of nominal capacity, using a current of 2.5 C. The last discharge step was cut off when the lower voltage limit was reached.

Cyling of batteries as well as ultrasonic measurements were performed at room temperature (25 °C).

3.6.2 Practical implementation

The estimation of state of charge via ultrasonic probing can be divided into subtasks. An overview of the process is shown in Figure 3.6. First, an electric signal of convenient frequency has to be generated. Second, this signal must be amplified and converted to sound. Then the signal must be transmitted through the lithium-ion cell, where it is modified in function of the materials properties and geometry.
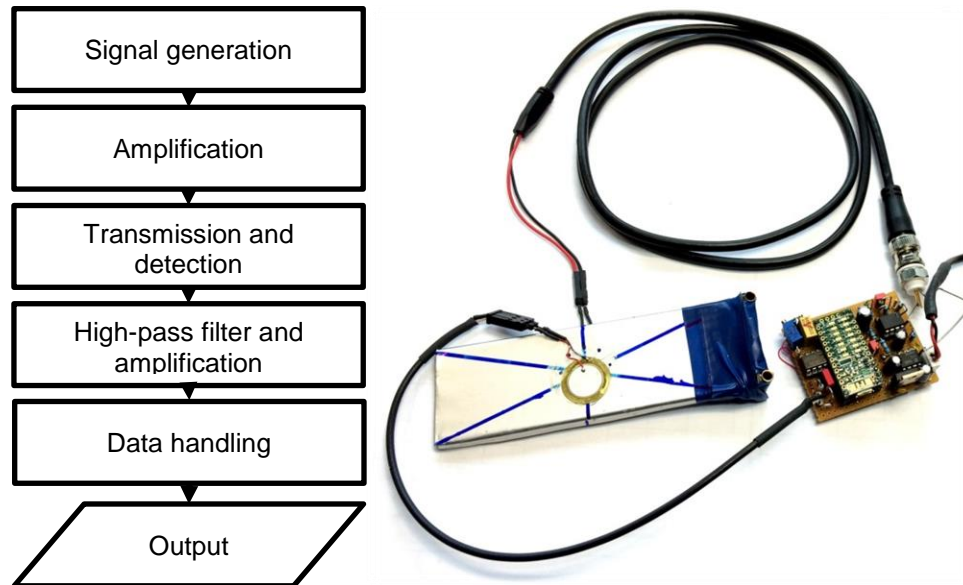

Figure 3.6 Flow chart and proof of concept for ultrasonic state of charge estimation. The flow chart visualizes the necessary steps. Signal generation and data handling are performed in the microcontroller, while auxiliary circuits are necessary for amplification, signal treatment and power supply. The electronic circuitry of the low-cost proof of concept for ultrasonic state of charge estimation is shown connected to the lithium iron phosphate cell. The stripboard is mainly occupied by power supply and unused features of the utilized development board. Photograph reproduced with kind permission of Lukas Gold, Fraunhofer ISC.

When the modified signal has been converted back by a transducer, it has to be amplified and it is useful to exclude low frequency noise by a high-pass filter. The signal can be interpreted and translated into an estimated value of state of charge.

A more practical implementation of the necessary steps was constructed as a part of this thesis. For control measurements, a DS1052E digital oscilloscope by RIGOL with a sampling rate of 50 MSa s^{-1} was used.

The device shown in Figure 3.6 was based on a *Teensy USB Development Board* which gives access to the capabilities of the commercial-off-the-shelf microcontroller MK20DX256VLH7 by Freescale Semiconductor Inc. Only two of the 64 pins of the microcontroller of the Cortex-M4 family had to be used. The electronic layout was

designed by Wolfgang Virsik at Fraunhofer ISC. The digital to analog converter is used to generate a signal, which is then amplified by an operational amplifier. The transmitted signal is then filtered by a high pass and once again amplified so that it can be detected by the analog to digital converter. Finally, the collected signal and peak to peak values of a selectable timeframe are sent via a serial port.

The source code is given in Annex A. The amplifier circuit for the sender was AC-coupled and set to a gain factor of approximately three to increase the peak-to-peak amplitude from the chips 3 V to approximately 25 V. The receiving amplifier was offset above ground by a voltage-adder integrated into the operational amplifier and set to a gain factor of approximately 24 to raise the answer signal from a few millivolts around ground to values between 0 V and 2 V against ground, therefore optimizing the signal for the chip's analog to digital converter. Furthermore, the amplifier contained a high pass filtering out lower frequency noise.

4 Inhomogeneous effects in 18650 Cells[1]

4.1 Introduction

Second-life applications of automotive lithium-ion batteries are currently investigated for grid stabilization. The reutilization of used automotive batteries depends on reliable projections of the remaining useful life. However, reports on sudden degradation of lithium-ion cells near 80 % state of health challenge these extrapolations.[8–10,87,138,160] This failure was demonstrated for different positive active materials. In this chapter, the causes of the degradation effect are elucidated in detail.

The regimes leading to sudden degradation in lithium-ion batteries were investigated on cell level by Simon Schuster at the Institute for Electrical Energy Storage Technology of TU München.[87] Control regimes causing sudden degradation were identified and guidelines for avoidance were given. The identified factors leading to the sudden degradation of useable capacity are high depth of discharge, high charging currents and low temperatures. Cells cycled between 3.0 V and 4.2 V with constant current charging at 0.5 C and constant current discharging with 1 C exhibited normal behavior up to 800 equivalent full cycles as shown in Figure 4.1. Based on the observed behavior it appears reasonable to predict several hundred additional cycles above 60 % residual capacity. However, a sudden increase in degradation rate occurs at about 80 % residual capacity. Only 150 cycles later the cell has lost more than half of its initial capacity.
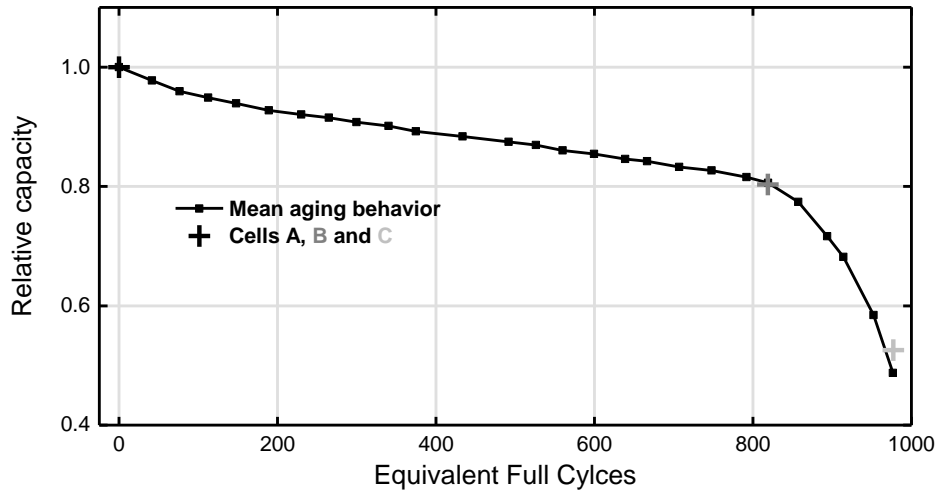

Figure 4.1 Overview of aged cells and their relative capacities. The cells show a strong increase in aging at about 80 % residual capacity. Cells are further analyzed in uncycled state (A), as they just start to age faster (B) and after the kink in capacity (C).

Cells exposed to this cyclic aging protocol at three different stages of aging are investigated. Uncycled, pristine cells (A) are compared to cycled cells that have just started to increase their aging rate (B) and cells that have already degraded significantly (C). Causes and effects are investigated in detail. Using destructive analysis, so called Post-Mortem studies, cells are characterized on the component level by electrochemical methods and chemical analyses. The influence of cell design on aging is discussed. Furthermore, possible mechanisms of sudden rapid aging are explained on component level. The breakdown of capacity is found to be triggered by the appearance of lithium plating confined to small characteristic areas, generated by heterogeneous compression. Thereby it is shown that the graphite electrode is the critical component for lifetime optimization. Moreover, the reasons for sudden degradation, as well as design and control countermeasures are explained. It is shown that graphite lithiation is the most critical control factor. Finally, a quick test for the vulnerability of cell designs towards nonlinear degradation is proposed.

4.2 Materials characterization

In this section, the changes on materials level will be discussed. To do so, the properties of the unaged cells are discussed as a baseline and to define the materials examined. Then, the changes are discussed component by component.

4.2.1 Unaged cells

The negative active material is found to consist of non-spherical graphite particles with sizes in the order of 10 μm as determined by scanning electron microscopy. The initial composition of the positive active material before formation is estimated to be $Li_{1.11 \pm 0.02}Ni_{0.33 \pm 0.01}Mn_{0.33 \pm 0.01}Co_{0.33 \pm 0.01}O_2$ by summing up total lithium, nickel, manganese and cobalt contents of the positive and negative electrode of the pristine cell as measured using ICP-OES. The composition of the positive active material in the pristine cell is found to be $Li_{1.06 \pm 0.02}Ni_{0.33 \pm 0.01}Mn_{0.33 \pm 0.01}Co_{0.33 \pm 0.01}O_2$. The errors are derived from measurement uncertainty. Oxygen content is inferred from crystal structure.

The positive electrode, and therefore the cell, has a capacity of 3.0 mAh cm^{-2}. 4.5 % of total lithium content is found in the negative electrode of the discharged pristine cell. This initial lithium content can be attributed to the SEI deposited during formation and to intercalated lithium that remains in the negative electrode after formation. The separator is based on polyethylene and polypropylene layers with an overall thickness of 25 μm. The electrodes are wound into a jelly roll on a stainless-steel mandrel with the positive tab on the inside and the negative tab on the outside of the roll. The graphite electrode is 2 mm wider than the positive electrode ensuring an overlap of about 1 mm on both sides of the strip.

4.2.2 Positive electrode

Visual inspection of the positive electrode does not reveal any changes except delamination effects upon unwinding of the jelly rolls. The SEM micrographs in Figure 4.2 confirm the absence of major changes in NCM morphology. The typical hierarchical structure, consisting of spherical particles several micrometers in diameter with a substructure showing a feature size below one micrometer appears unchanged even at pronounced aging states of the battery.
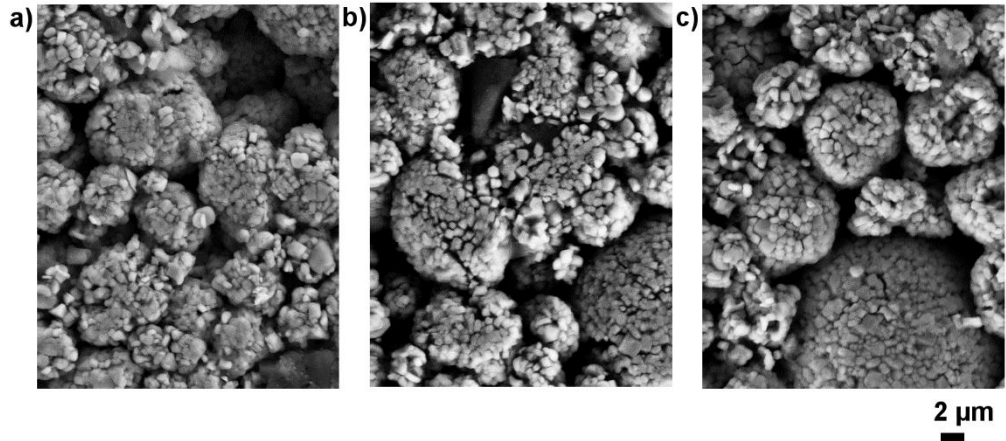
Figure 4.2 Scanning electron micrographs of cathodes from cells a) A, b) B and c) C.
The micrographs show no changes in morphology of the samples. In all three samples the
fine particulate structure is retained and the agglomerates are intact. Micrographs reproduced
with kind permission of Elena Fleder, Fraunhofer ISC.

The XRD patterns in Figure 4.3 show the good stability of the NCM host lattice that is also
known from previous studies.[114,123,161,162] Based on XRD patterns of pristine NCM published
by Choi *et al.*[110], peak positions and relative heights for NCM in different states of lithiation
have been compared to the aged samples. The two lithiation states closest to those found in
this study are used for comparison. Literature spectra of fully lithiated NCM
($LiNi_{0.33}Mn_{0.33}Co_{0.33}O_2$) and partially delithiated NCM ($Li_{0.7}Ni0_{.33}Mn_{0.33}Co_{0.33}O_2$) compare
well to samples A, B and C.
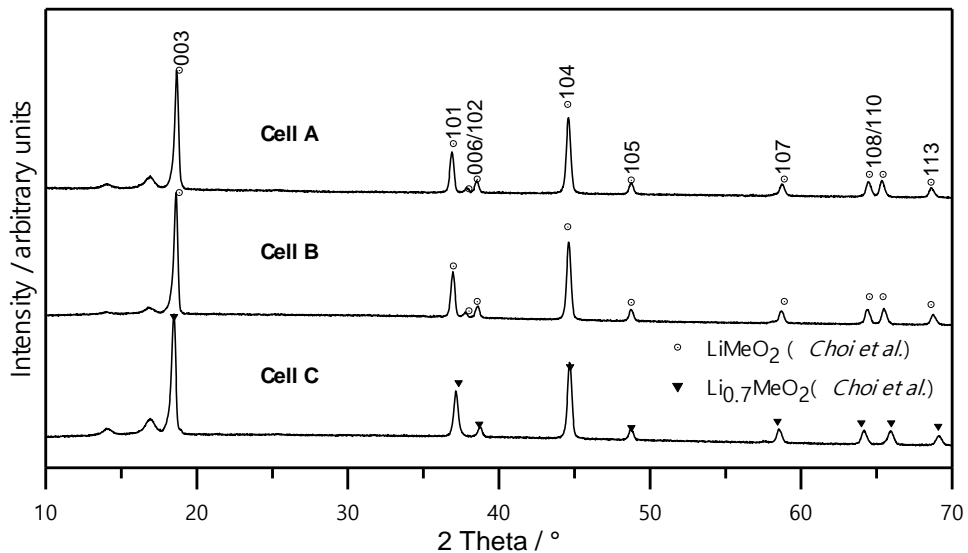
Figure 4.3 XRD patterns of NCM taken from cells A, B and C. NCM active material XRD
patterns of samples taken from discharged cells A, B and C. Comparison to data from Choi *et
al.*[110] shows that variations are due to a change in state of charge, not degradation.

The crystal structure of all samples is intact and all peaks can be attributed to their respective miller indices. Rietveld refinement based on a reference pattern[163] yielded the lattice parameters given in Table 4.1.

Table 4.1 Lattice parameters and deduced lithiation of electrode samples. Lattice parameters for $R\overline{3}m$ phase obtained by Rietveld refinement of reference pattern,[163] as well as lithiation x and lithium loss in $Li_xNi_{0.33}Mn_{0.33}Co_{0.33}O_2$ as deduced from Figure 4.4. Given uncertainties are estimated by the standard deviations of the refinement and of the predictions based on calibration curves in Figure 5.2.

Sample	Parameter a / nm	Lithiation x deduced from a	Li-loss deduced from a / mAh cm⁻²	Parameter c / nm	Lithiation x deduced from c	Li-loss deduced from c / mAh cm⁻²
Cell A	0.2853 ± 0.0001	1.0 ± 0.1	0	1.4242 ± 0.0002	1.0 ± 0.1	0
Cell B	0.2847 ± 0.0002	0.9 ± 0.1	0.44 ± 0.04	1.4276 ± 0.0002	0.9 ± 0.1	0.33 ± 0.02
Cell C	0.2832 ± 0.0002	0.7 ± 0.1	1.5 ± 0.2	1.4387 ± 0.0003	0.7 ± 0.1	1.40 ± 0.08

Lattice parameters reported from pristine cells show an approximately linear dependency on lithiation.[82,110,164] Therefore, the change of lattice parameters can be used to determine the lithiation of NCM as shown in Figure 4.4 and, combined with the initial lithium content c_0 of 5.59 mAh cm⁻², the loss of lithium:

$$Li_{loss} = \Delta[\text{Lattice Parameter}] \, \text{Slope}^{-1} \, c_0 \qquad \textbf{Equation 34}$$

The results shown in Table 4.1 point to considerable lithium loss. In contrast, degradation was not detected. Thus, morphology and crystallographic structure are found to be unchanged by SEM and XRD. Loss of lithium is the only change found at the NCM electrode. A thin passive layer inducing increased resistance might have formed, but is not detectable by the utilized methods.
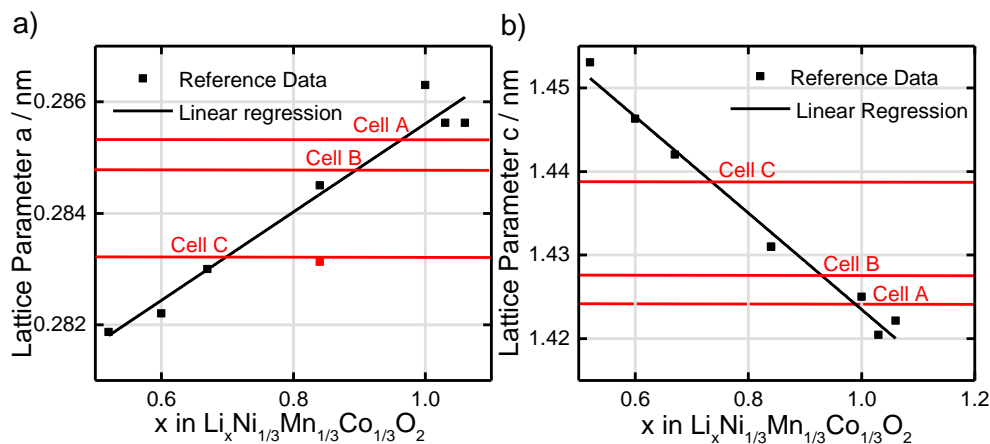

Figure 4.4 Lattice parameters used to determine the lithiation of NCM. Lattice parameters a) a and b) c are used to determine the lithiation of NCM. Published reference data[162,165,166] is used to calculate calibration lines a= $[(0.0079\pm 0.0008) \, x + (0.2777 \pm 0.0006)]$ nm and c= $[(0.058\pm 0.003) \, x + (1.481 \pm 0.003)]$ nm. One outlier from[165] was masked (red).

4.2.3 Negative electrode

Figure 4.5a) shows photographs of the graphite electrodes of cells A, B and C. The graphite electrode of cell A appears totally black, as is expected from a functional discharged carbon based active material. A small area exhibiting lithium plating is found on the graphite electrode of cell B. Much larger areas of cell C are covered by metallic lithium and other residue. The finding of inactive lithium confirms the previous work by Broussely *et al.*, who also linked the finding of inactive lithium to the appearance of sudden degradation.[9] The photograph of the negative electrode extracted from Cell B shows well defined plating patterns. A thin stripe in angular direction, an area in the middle of the electrode and a regular pattern of axial stripes are much brighter than the surrounding graphite. The central area and the stripe pattern exhibit a metallic sheen.
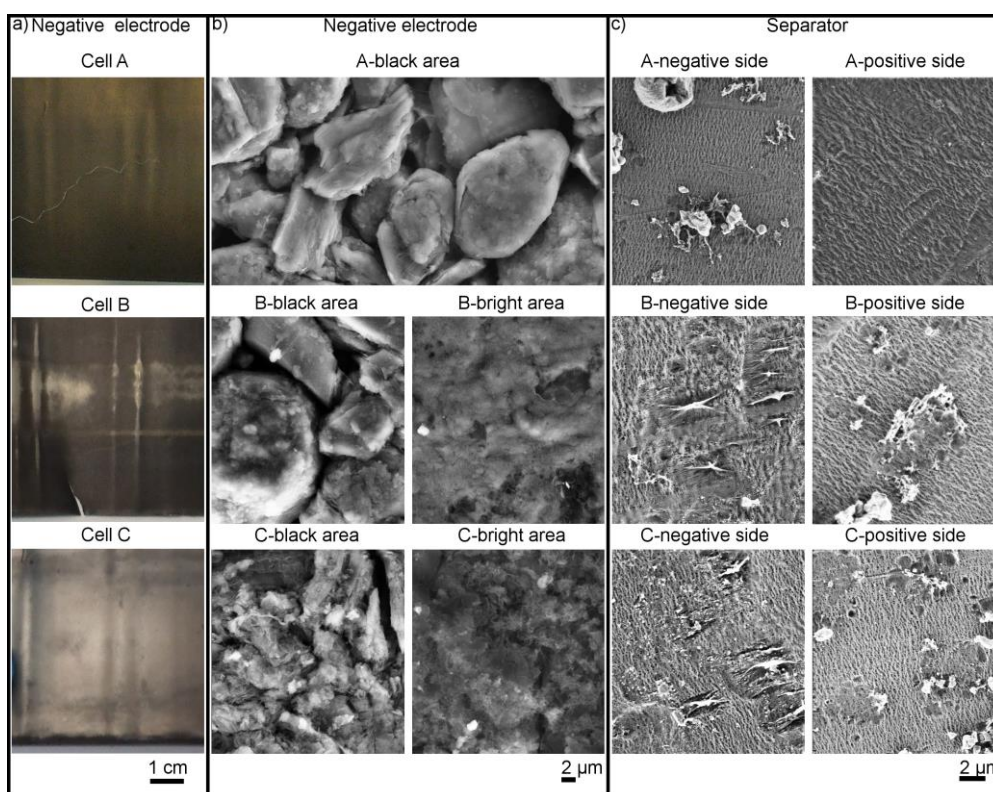
Figure 4.5 Degradation of negative electrode and separator. a) Plating on aged graphite electrodes: No plating is observed on pristine cell A. Cell B shows first plating as it has just started to degrade suddenly and cell C shows extended plating. b) Scanning electron microscopy shows that black areas B-black area and C-black area resemble the pristine graphite of cell A, while B-bright area and C-bright area are degraded. c) SEM micrographs of the separators of cells A, B and C. Areas of the negative facing side that came into contact with plated lithium show degradation. Photo- and micrographs reproduced with kind permission of Elena Fleder, Fraunhofer ISC.

Chemical analyses by ICP- OES are utilized to investigate the passive layers found on the aged and pristine samples. Increased values of manganese, nickel, cobalt and lithium are found on the negative electrode of cell B shown in Table 4.2. The negative electrode of cell C exhibits even higher levels. The loadings of washed out metals increase with aging. As manganese is associated with increased SEI formation[114,167] and as nickel and cobalt show similar behavior, only manganese and lithium contents are discussed here. A baseline manganese content of 11 nmol cm^{-2} is found in Cell A. In cell B, the manganese loading of the graphite electrode has risen to 33 nmol cm^{-2}. Due to the small size of the regions covered by plated lithium, they have not been sampled separately. On the other hand, in Cell C, the areas covered by plating were sufficiently large to be sampled and analyzed separately from the areas appearing unchanged. The loading found in areas appearing black has risen to 46 nmol cm^{-2}, approximately four times more than in the pristine sample. The sample taken from a region covered by a plated lithium moss is found to contain 139 nmol cm^{-2}, about twelve times more than in the baseline value and about three times than the quantity found in other areas of the same cell. The findings on inactive lithium shown in Table 4.2 follow the same trend. To illustrate the electrochemical impact, the findings are converted from nmol cm^{-2} to mAh cm^{-2}. In the pristine cell A, only 0.25 mAh cm^{-2} of inactive lithium are found on the graphite electrode. Furthermore, in cell B the amount of inactive lithium has more than doubled to 0.55 mAh cm^{-2}. In cell C 0.85 mAh cm^{-2} of inactive lithium are found on dark parts of the negative electrode. In an area with a visible surface film and a metallic sheen, 1.87 mAh cm^{-2} are found. The increase in inactive lithium amounts to about half of the initial active lithium content of the positive active material. The dramatic loss of lithium in degraded areas causes an important part of the overall loss of lithium inventory.

Table 4.2 Lithium and Manganese contents on negative electrodes of cells A, B and C. Metal concentrations were detected using ICP-OES. Errors are based on measurement uncertainty of IPC-OES. Possible systematic errors caused by non-complete digestion add to uncertainty. Nonetheless, a clear trend in metal contents is observed.

Sample	Lithium Content / mAh cm^{-2}	Manganese Content / nmol cm^{-2}
Cell A	0.25 ± 0.01	11 ± 1
Cell B	0.55 ± 0.01	33 ± 2
Cell C Dark Areas	0.85 ± 0.02	46 ± 2
C Bright Areas	1.87 ± 0.04	139 ± 7

SEM observations confirm that areas appearing black are only slightly changed, while areas with visible plating are covered by a thick layer of degradation products. The degradation of the graphite electrode is shown in Figure 4.5b). The graphite particles of the negative electrode of cell A appear pristine. The black areas of cells B and C are covered by a thin passive layer only. Bright areas with visible plating are shown on the right. The surface film completely covers all graphite features in plated areas. Table 4.2 resumes the elevated amounts of NCM dissolution products found in plated areas. Traces of nickel, manganese and cobalt are known to dissolve from the positive electrode and deposit on the graphite electrode, as the lithiated graphite quickly reduces most metal ions to their metallic form.[57] Such deposits are believed to strongly influence graphite aging and the formation of surface films, explaining the faster aging of graphite electrodes in actual batteries than in half cells consisting of graphite electrodes and lithium metal.[114] As reaction products of positive active material degradation are deposited on the negative electrode by reduction and as baseline contents are low, chemical analysis of the negative electrode is a good way to probe surface reactions of the positive electrode.[82,83]

4.2.4   Separator

The separator was inspected for clogging and degradation using scanning electron microscopy. Figure 4.5c) shows micrographs of both sides of the separators taken from cells A, B and C. No changes are found on the side pointing to the positive electrode and in areas facing black parts of the negative electrode. The separators retain the original oriented porous structure with some minor imprints likely caused by compression. In contrast, where the separator was exposed to plated lithium, craters several micrometers in diameter can be observed in the micrographs. Those craters, visible on micrographs on the negative side of the separator taken from cells B and C, exhibit thick string-like aggregates. Their aspect points to localized melting or chemical degradation. This effect may have been caused by localized heating, mechanical causes or chemical interactions and shows the impact of lithium plating on the separator.[86,168] Plated lithium and the damaged separator influence the safety of lithium-ion cells in thermal and mechanical abuse scenarios.[169]

4.3   Main degradation mechanism for lithium loss

Figure 4.6 compares the capacity loss found during cycling to the lithium content found on the graphite electrode using chemical analysis by ICP-OES and to the lithium loss deduced by XRD measurements. Lithium found on the discharged electrode can be attributed to three main types.

1.   Active lithium which is not extracted from the graphite upon discharge as voltage cutoff limits the potential of the negative electrode.
2.   Lithium compounds deposited on the graphite surface forming the so-called SEI.
3.   Lithium loss due to lithium plating, as described in literature.[3,85,170]

Chemical analysis does not differentiate inactive lithium from buffered, potentially active lithium intercalated in the active graphite. Still the increasing lithium content of the negative electrode can be related to lithium loss, as the discharge potentials of the negative electrode increase over aging, which points to a loss of buffered lithium. Cell capacity and lithium loss found by XRD and ICP-OES show a similar trend upon aging. Additionally, analysis of the anode shows the importance of lithium plating. The lithium content found in samples of cells A and B as well as a sample from a dark area of cell C (C dark) show a trend similar to the linear part of the capacity evolution. Lithium loss found in a sample taken from a bright area of cell C (C bright) explains the acceleration of the capacity loss. The inactive lithium found in this area is excessive. The deposition of inactive lithium species is the main aging mechanism observed and acceleration is caused by the defective areas.
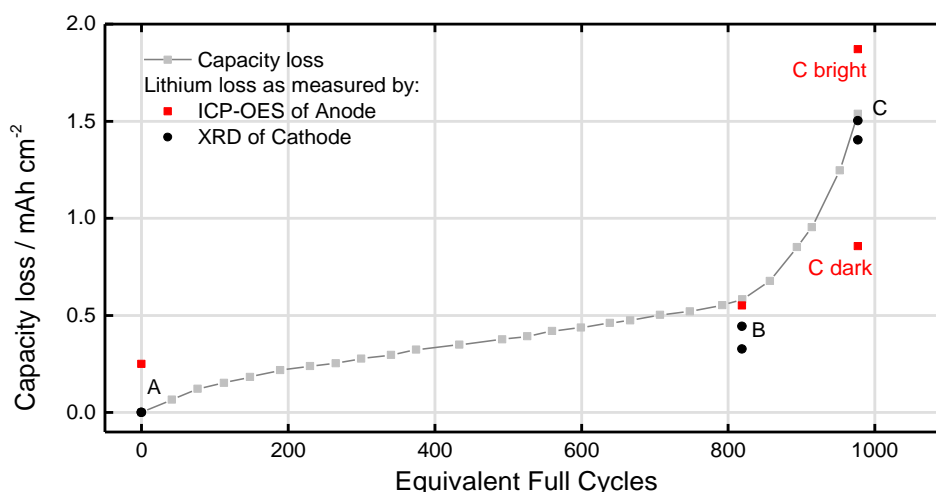
Figure 4.6 Comparison of capacity loss and loss of lithium. Mean capacity loss of cycled 18650 cells compared to lithium content on the graphite electrode and delithiation of the cathode as found by XRD measurements. Lithium loss is given in mAh cm^{-2} for comparability.

4.3.1 Evolution of electrochemical behavior

In Figure 4.7 the slow galvanostatic charge and discharge cycle (a) of the original cells, as well as the corresponding incremental capacity curves (b) are depicted. Cell A shows one major and three minor peaks, corresponding to the superposition of the characteristic peaks of the graphite electrode and the broad curve of the NCM electrode. The characteristic peaks flatten out slowly during normal aging but vary rapidly as the battery changes its degradation behavior. Interestingly, the voltage region above 3.9 V appears nearly identical for all three aging states, with only a slight decrease in discharge voltage and incremental capacity. The peaks corresponding to the voltage plateaus in the range between 3.4 V and 3.9 V become smaller for cell B and partially disappear for cell C. A pronounced loss of incremental capacity in the range between 3.4 V to 3.9 V can be noticed. In the lower voltage region below 3.4 V no major changes are visible. It should be stressed that the charge and discharge profiles at the beginning of rapid degradation are only slightly changed compared to the pristine cell, making detection of this phenomenon very difficult without known history. Once the aging rate increases, the capacity in the lower voltage range drops heavily and the peaks almost disappear. A recent incremental analysis study on different commercial batteries reported very similar behavior, although a different positive active material was used.[171]
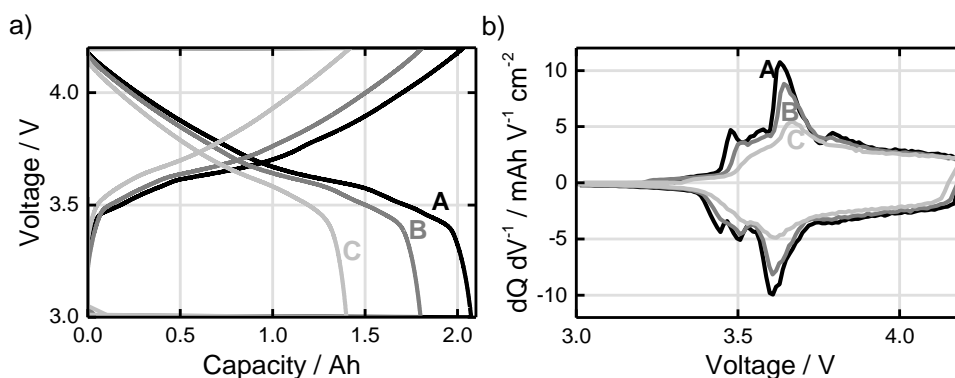
Figure 4.7 Full cell characterization by incremental capacity analysis. a) 0.02 C full charge and discharge cycle performed before dissection of the original cells A, B and C. b) Incremental capacity curves calculated from the same data.

To understand the observed phenomena, three-electrode laboratory cells from six locations on the unrolled jelly roll are constructed as described in the experimental section. The laboratory cells are controlled by current and terminal voltage, while the reference electrode is used for monitoring of electrode potentials only. The same slow charge and discharge profiles as on original cells are applied. Based on the obtained potentials, incremental capacity analysis of the two electrodes' behavior is carried out. Samples are numbered based on the sampled cell and the specimen location by adding the number of the sampling spot as shown in Figure 3.3 to the cells' abbreviation.

An overlay of incremental capacity curves obtained from pristine original and laboratory cells is shown in Figure 4.8. Sample A6 is omitted due to excessive noise caused by a bad connection. Original and laboratory cells show similar behavior. Peak positions and capacity distribution as well as overall capacity compare well. The curves superimpose as expected from a homogeneous electrode. Results from laboratory cells are representative of the behavior in the commercial cells investigated.
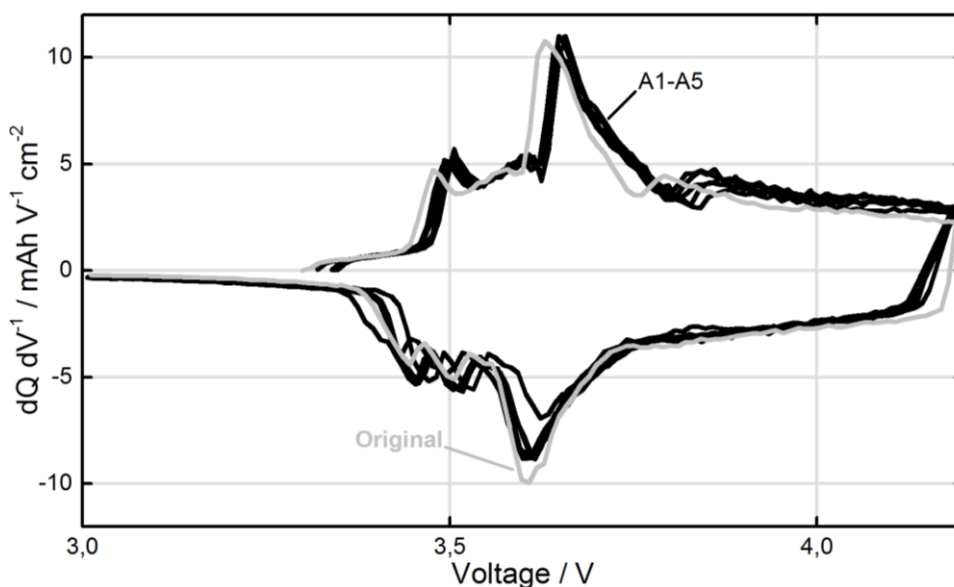

Figure 4.8 Incremental capacities of aged full cells compared to sampled areas. Incremental capacity curves of sampled areas of a pristine cell are compared to the overall incremental capacity of the full cell.

Figure 4.9 shows incremental capacity curves based on graphite and NCM electrode potential comparing B2 and B3 to pristine sample A5. With less than 25 % capacity loss, sample B3 is representative of areas showing lesser extents of degradation, while sample B2 has lost more than 55 % of its capacity. The NCM capacity curves do not change their shape but are cut off at lower lithium content upon aging. No signs for positive active material loss or changes in electrochemical behavior are visible in the samples. Capacity curves of the graphite electrode change in a more complicated manner. Sample B2 has suffered heavy degradation. Peak heights above 0.15 V are about one third smaller than in the pristine cell, a clear sign for pronounced active material loss. The peak at 0.10 V has vanished nearly completely. As this peak corresponds to highly lithiated states, this is a prominent sign for lithium loss, possibly due to nearby lithium plating. The loss of lithium content manifests in a shift to lower lithiation in the corresponding NCM electrode as is evident from the more positive cutoff potential. Sample B3 shows only slightly depressed peaks both for charging and discharging. Peak heights above 0.15 V are depressed by only about one eighth, indicating less active material loss. The peak at 0.10 V, corresponding to the high lithiation stage, is present.

The conservation of this peak shows that lithium loss is slow in comparison to active material loss in areas that are not yet affected by rapid capacity loss. Therefore, it appears that slowly aging regions lose some active material and lithium, while areas degrading faster start to lose higher amounts of active graphite and excessive amounts of lithium.
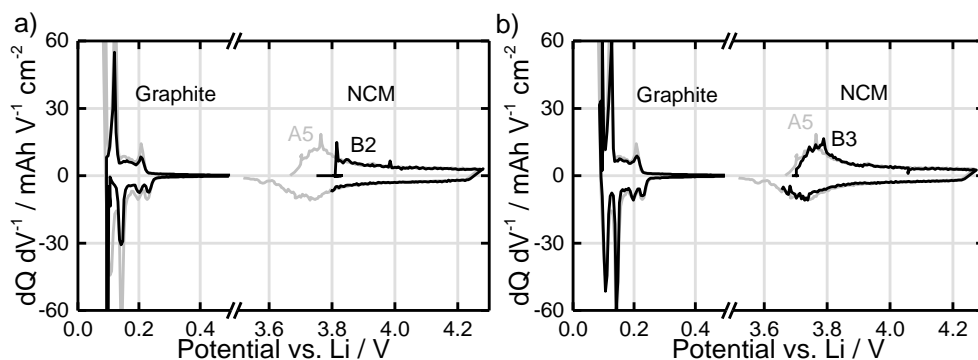

Figure 4.9 Incremental capacities of two electrode areas of cell B. Incremental capacities of samples B2 and B3 compared to sample A5 of the pristine cell. The incremental capacities of the more negative graphite and the more positive NCM are resolved for each sample.

The potential of graphite electrode discs sampled from the discharged cells and built into laboratory cells is compared in Figure 4.10. The negative electrode discharges to higher potentials in more degraded areas. Samples with low capacity loss show unspecific behavior. Due to remaining lithium reserves and moderate discharge potentials, degradation of samples with low capacity loss is thought to be dominated by other factors. As the lithium reserve is consumed and the final discharge potential of the graphite electrode is increased by lithium loss, a positive correlation seems to appear. Final discharge potential and capacity loss show a trend that can be explained by fast active material loss. There is some evidence in our previous studies and in literature that high depth of discharge may lead to increased material loss in graphite electrodes.[8,87,117] The volume changes associated with lithiation and delithiation are reported to cause contact loss by mechanical action and increased SEI formation.[3,94,138] Active material loss leads to lower potentials upon charging and therefore to higher lithium loss. Both the change in balancing and the increased overpotentials due to lower active surfaces and SEI formation may contribute to the more negative potentials during charging. Since less active graphite is available, remaining graphite does not only have to accommodate more lithium but also experiences higher current densities leading to higher overpotentials. Losses become more accentuated as the negative electrode reaches the potential of metallic lithium. The resulting irreversible lithium plating leads to further increased discharge potentials and a vicious circle ensues. Areas with initially less active graphite loss and lower current density are increasingly affected as lithium is consumed by defective areas thus also changing their final discharge potentials.

Also, Oldham has shown that the edge of an electrochemically active area adjacent to an insulated area experiences excess currents.[172] The area experiencing plating rapidly expands and overall battery capacity drops. The resulting trend can be observed in Figure 4.10 with some samples showing extreme capacity losses accompanied by high maximum potentials upon discharge.
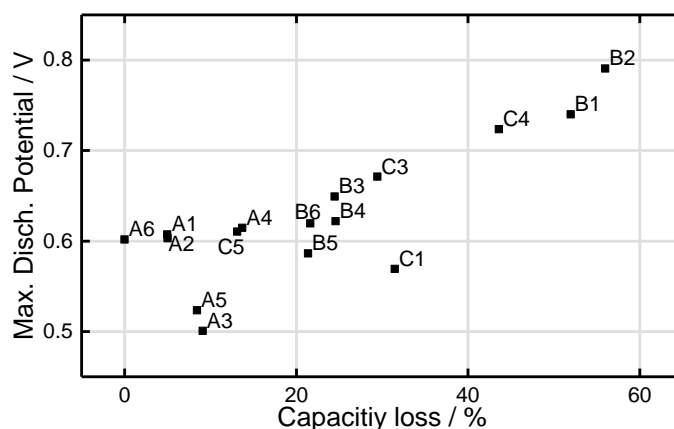

Figure 4.10 Negative electrode discharge potential related to capacity loss. The maximum potential of sampled graphite electrode discs increases with capacity loss. Deep delithiation of graphite can be linked to active material loss.

4.3.2   Heterogeneous cell behavior

As pointed out in section 4.3.1, some peaks in incremental capacity curves of aged cells start to disappear as degradation accelerates. In Figure 4.11 incremental capacity curves of the sampled laboratory full cells are compared to the respective aged original cells. In Figure 4.8 it was shown that in pristine cell A all areas show uniform behavior with nearly no variation in peak position. Although aged, most areas of cell B show a comparable behavior. Samples collected from areas affected by lithium plating show different peak patterns with changed peak positions and greatly decreased capacities at lower voltages. Accordingly, the overall behavior below 3.9 V is slightly altered, too.

The effects on overall charge and discharge behavior of cell C are already very pronounced as a substantial portion of the battery has been affected by lithium plating. Sampled areas show marked differences in peak position and capacity in the lower voltage region. Highly altered profiles are found in five of six samples leading to peak smearing and a strong decay of capacity at lower voltages. For comparison, only two samples show altered capacity curves in cell B, but their aspect is already the same as found for many samples in cell C.

A simplified model of the cell is helpful to explain the changes in the original cell. Viewing the jelly roll as a parallel connection of degraded and nearly unaffected areas, its overall capacity is the sum over all areas. The overall incremental capacity per area is a function of several incremental capacity curves of areas in different stages of degradation. As increased aging begins, only a very small part of the surface exhibits changed behavior. Therefore, the impact on overall charge and discharge behavior is small, although local changes are dramatic. As rapid aging proceeds, more and larger parts of the electrode are affected. The impact of altered areas on the overall curve becomes more important due to their larger surface fraction. The broad variation of peak positions leads to a smeared overall behavior.
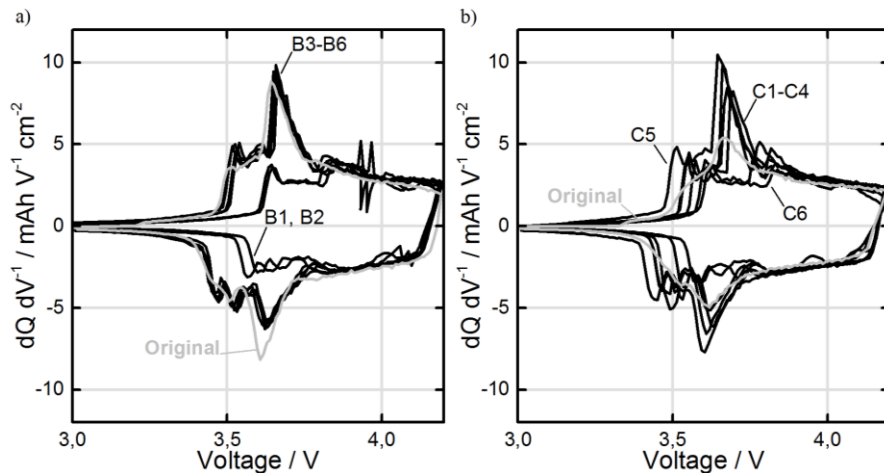
Figure 4.11 Incremental capacities of aged full cells compared to sampled areas. Incremental capacity curves of sampled areas of cells a) B, b) C are compared to original cells.

4.4 Identifying the cause for heterogeneous cell behavior

The initial onset of plating causes a sharp increase in aging rate. As this coincidence may explain the change in aging rate, the origin of the different patterns described in paragraph 4.2.3 were investigated by thermography, computed tomography and Post-Mortem studies. A thin line is already present on pristine negative electrodes. This potential plating area is attributed to an unknown imperfection in the production process. Waldmann *et al.* recently showed that the pattern formed by axial stripes is caused by current collectors in cylindrical cells.[4] Lithium plating first appears in the central area of the electrode and on the edges of the regular axial stripes. For that reason, it should be possible to identify the cause for plating by explaining the stripe pattern. Several reports on heterogeneous aging have been published recently and a number of possible explanations are given. The authors propose temperature, pressure and potential variations as possible causes of local plating.[4,10,173] However, potential variations caused by the resistance of the current collectors are not expected to cause patterns such as the regular axial stripes found in this study.

4.4.1 Temperature distribution compared to aging patterns

Temperature gradients upon fast cycling of a pristine cell are investigated by thermal imaging. Figure 4.12 shows the electrical power and voltage profiles during a full cycle together with the surface temperature measured on the three points shown in the thermograph below. The thermographic image shows the battery at peak temperature. The surface of the battery is heated up to more than 48 °C. Surface temperatures appear homogeneous. A small axial variation is visible; in contrast, no angular variation was detected. While radial gradients may have occurred,[4,174] the stripe pattern found on the graphite electrodes is caused by angular variations. Such angular variations should be expected to be observable on the surface of the battery. Since no such variation is detected and due to the nature of the pattern, the pattern of axial stripes appears to have been caused by some other influence.
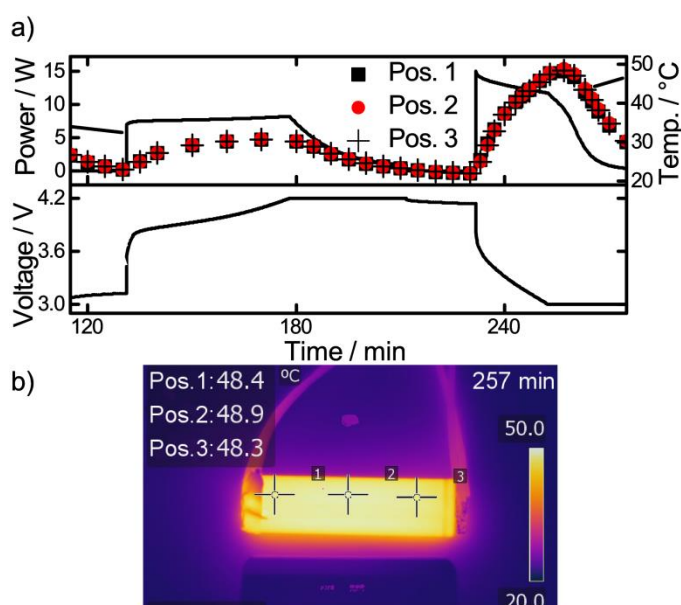
Figure 4.12 Temperature evolution during fast cycling. Voltage, power and temperature evolution of an 18650 cell. Temperature of three surface points is logged using thermography. The thermograph shows the distribution at maximum temperature of the cell and position of the logged surface points.

Besides the stripe pattern, plating also appears earlier in central areas than in the axially outer parts. The axial distribution of the surface temperature is investigated in order to discuss its possible influence on heterogeneous plating. To quantify the axial distribution, three measurement points are tracked over time. At the three points maximal temperatures of 48.4, 48.9 and 48.3 °C are found, respectively. The surface temperature varies by 0.6 °C only. Compared to the overall temperature swing, the observed spatial temperature variation is small. Such a small variation is not expected to induce significant electrochemical differences.

Nonetheless, already six cycles of the fast cycling protocol cause the stripes shown in Figure 4.13a) and b). The observed temperature gradients do not seem to explain the double stripe pattern or axial variation of plating produced.
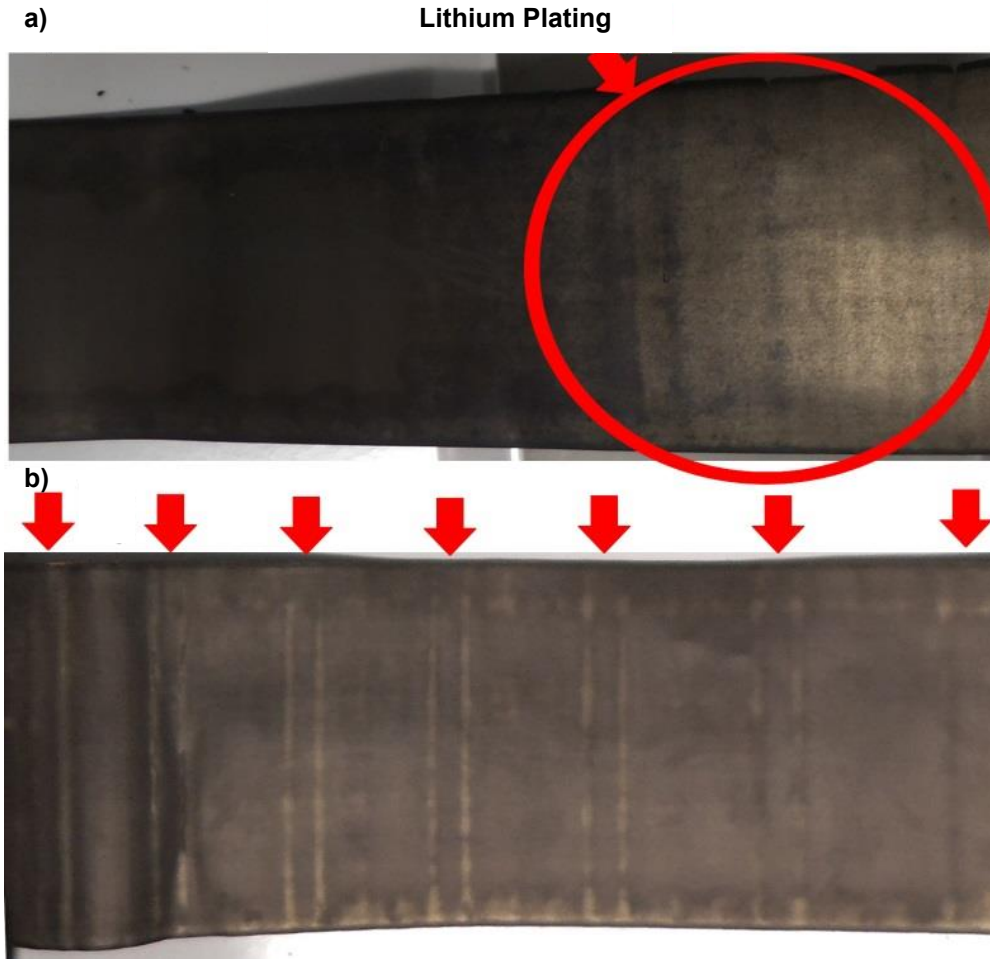

Figure 4.13 Lithium plating caused by fast cycling. a) Outer part of the negative electrode exposed to 6 fast cycles. b) Inner part of the same electrode showing a stripe pattern. Plating is marked by an ellipsis and arrows. Photographs reproduced with kind permission of Elena Fleder, Fraunhofer ISC.

4.4.2 Compression

The computed tomographic image in Figure 4.14 shows deformation of the jelly roll in a pristine cell. Figure 4.13a) and b) show plating patterns after fast, deep cycling. Plating occurs in comparable regions as in cells B and C and the regular stripe pattern already shown in cell B is reproduced. The current collector tab of the positive electrode marked as (1) in Figure 4.14 creates a bulk close to the mandrel. The aluminum and separator foil surrounding the tab appear black in the tomographic image but cause further bulk.

As the jelly roll is confined in the cylindrical stainless steel case, this bulk and the resulting deformation cause increased variations in compression. The bulk created by the negative current collector tab marked as (2) in Figure 4.14 is less pronounced. Therefore, a minor effect is expected.
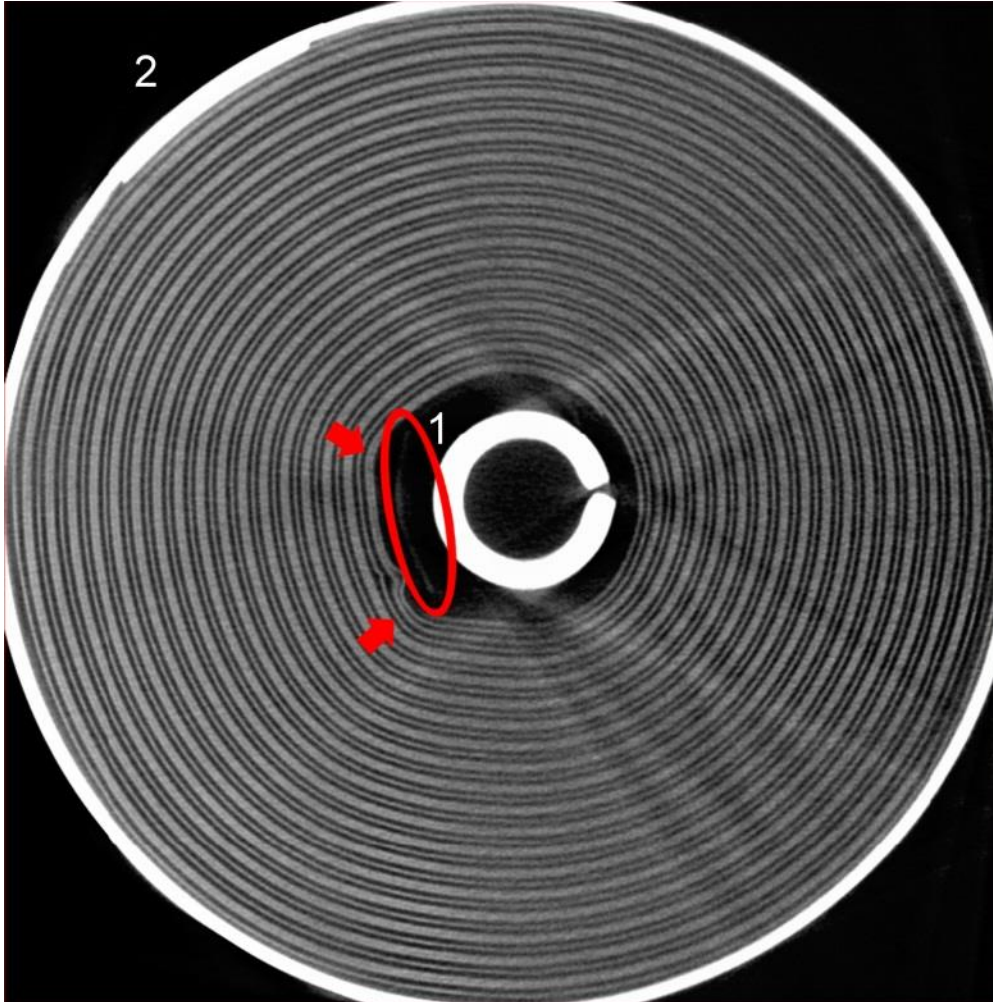
Figure 4.14 Heterogeneity due to current collector. a) Computed tomographic crosscut of a pristine cell. The positive (1) and negative (2) current collector tabs are visible. The positive current collector is marked by an ellipsis, resulting deformations to the jelly rolls are marked by arrows. The positive current collector deforms the jelly roll.

The stripe patterns shown in Figure 4.13b) can be clearly linked to the positive current collector tab (1) by their regular arrangement and occurrence in the inner part of the jelly roll.[4] As shown in Figure 4.13a), the negative current collector creates a much less pronounced effect, which is overlaid by the current gradient caused by the nearby positive current collector and the resistance of the copper foil.

The tabs are found to deform the jelly roll and therefore create spatial variations leading to plating especially near the edges of the imperfections. Heterogeneous pressure has been shown to have an effect on lithium-ion diffusion through the separator[125,175] and to lead to localized defects in controlled experiments.[41] In general, increased pressures are expected to show detrimental effects, even if slight compression might be beneficial.[125,175,176] Additionally, the shape of an electrode has an influence on the diffusion regime in front of it. Oldham has shown that ridges may experience an excess current, while grooves experience reduced currents.[177] Variations in lithium concentration are known to contribute to overpotential.[178]

As the battery ages and NCM potentials are shifted to higher potentials due to lithium loss, graphite maximum potentials rise, too. Deep discharge is reported to lead to active material loss in graphite electrodes.[8,117] Consequently, the capacity balancing of the two electrodes is gradually altered until the negative electrode becomes capacity limiting in some areas. Since the negative electrode operates very closely to lithium potential, plating may occur if the graphite capacity becomes inferior to locally available lithium in a given part.

4.5   Control experiment for plating susceptibility

It is expected that large currents and voltage windows as well as low temperatures facilitate the occurrence of local plating. This localized plating is believed to cause subsequent rapid degradation. As a quick test, cells can be cycled at maximum permissible voltage swing and charge and discharge currents, exhausting the limits stated in the datasheet. Using constant voltage steps both upon charge and discharge of the cell, maximal states of charge can be obtained. Especially when soft packages are used, the cells should be tested in their final fixture. For a quick test for plating, cells are opened as soon as aging accelerates, or after a determined number of cycles. Using visual inspection, the negative electrodes are checked for plating.

Figure 4.13a) and b) show the outer and inner part of the graphite electrode of a cell subjected to such maximum strain cycling. The cell was cycled only 6 times and retains nearly 99 % of its initial capacity. Already after 6 cycles plating has occurred. Patterns are found near the negative current collector tab and the positive current collector tab in the center of the cell. As can be seen in Figure 4.13a), the plated lithium near the negative current collector shows a slight stripe pattern but it is unclear if the plating is due to imprints from the negative current collector, or to the resistance gradient. A well-defined pattern of axial stripes is visible in Figure 4.13b), showing the inner part of the negative electrode. Plating occurs on the stripe pattern imprinted by the positive current collector, pointing to compression as the cause.

Figure 4.15 Localized plating due to external compression. a) A hose clamp is placed on a cell. b) Plating is visible on the overlap of the current collector imprints and the clamp which are visualized by black and red rectangles respectively.

In a next step, a control experiment for the hypothesis on the influence of heterogeneous compression on plating is carried out. Local compression is applied by a clamp fixed around the diameter of cylindrical cells as shown in Figure 4.15a). The onset of lithium plating becomes even more localized and pronounced when a clamp is applied on a pristine cell, as shown in Figure 4.15b). Patches of plated lithium appear on the overlap of the clamp and the current collector. These spots show highest compression and hence the strongest tendency to plating. This control experiment verifies the theory of compression induced plating and shows the detrimental effect of heterogeneous compression. The demonstrated induction of local plating by external compression qualitatively shows the influence of cell and pack design and mechanical constraints, as caused by unsuitable mounting and potting methods. Furthermore, this work shows how easily such defects can be detected by Post-Mortem inspection in sharp contrast to the complex detection using electric measurements on cell level which is often subject to interpretation.

5 Impact of vibrational stress on cylindrical and pouch cells[1]

5.1 Introduction

Apart from static pressure, vibrations are another aspect of mechanical aging. Contrary to pressure effects discussed in the previous chapter, their occurrence depends on the actual usage scenario of the battery. Still, vibrations are an unavoidable companion of mobile applications. However, as of today, vibrations and shocks are mainly investigated in the scope of possible dangers occurring during the transport of lithium-ion cells. The Institute for Electrical Energy Storage Technology of the Technische Universität München and TÜV SÜD Battery Testing GmbH subjected pouch and cylindrical cells to vibrations and shocks. After the test protocols including the UN 38.3 test as well as long-term vibrations, they were characterized by electrochemical impedance spectroscopy and galvanostatic experiments.

While UN 38.3 uses generic vibration profiles to assure the safety of cells and batteries during transportation, the long-term vibration profiles were based on real life measurements.[150] The cells were then investigated in detail by Fraunhofer ISC to reveal damages that may not be detected by visual and electric inspection alone.

Figure 5.1 Directions of strains on a) pouch and b) cylindrical cells. a) Pouch Cells were shocked in y- and z-direction. b) Cylindrical cells were shocked in axial and radial directions. Photographs reproduced with kind permission of Elena Fleder, Fraunhofer ISC.

For details on cell level electrochemical investigations carried out by the Institute for Electrical Energy Storage Technology of the Technische Universität München, the reader is directed to the reference[11].

Strains were applied in different directions and it was found that damages depend heavily on the direction of shocks and vibrations. The terminology used to describe these directions is visualized in Figure 5.1.

Note that this terminology departs from terminology used in the joint publication to maintain consistency with chapter 4. In this chapter, defects caused by short term vibrations (UN 38.3 T3), shocks (UN 38.3 T4) and long term vibrations are discussed in detail, the found damages are put into perspective and design considerations are derived.

5.2 Effects caused by sine sweep vibrations according to UN 38.3 T3

While all other cells were found unchanged by sine sweep vibrations applied according to UN 38.3 T3, cylindrical cells strained in axial direction showed some changes that could be visualized by X-Ray tomography and Post-Mortem inspection.

Albeit not critical for the operation of the cells, the observations are instructive regarding the cell components involved and the methods used. Only a superposition for these cells is shown in Figure 5.2, but the approach was followed for all cells inspected in the studies. Superimposed 3-D volumes recorded before and after vibration testing are shown for a cylindrical cell shaken in axial direction and a pouch cell. The state before testing is shown in grey while the volume recorded after vibration testing is shown in green. All features, i.e. current interrupt device A, positive current collector B, anodes C, cathodes D and mandrel E, were inspected in each cell. The only effect caused by the sine sweep vibrations was a displacement of the mandrel E, as made obvious by the relative shift visible in Figure 5.2. All other areas appear nearly completely green, thereby showing the good superimposition.

Post-Mortem inspection of the cylindrical cell shaken in axial direction confirmed the observation made by tomography. The mandrel was found to be loose, while no further changes could be observed.
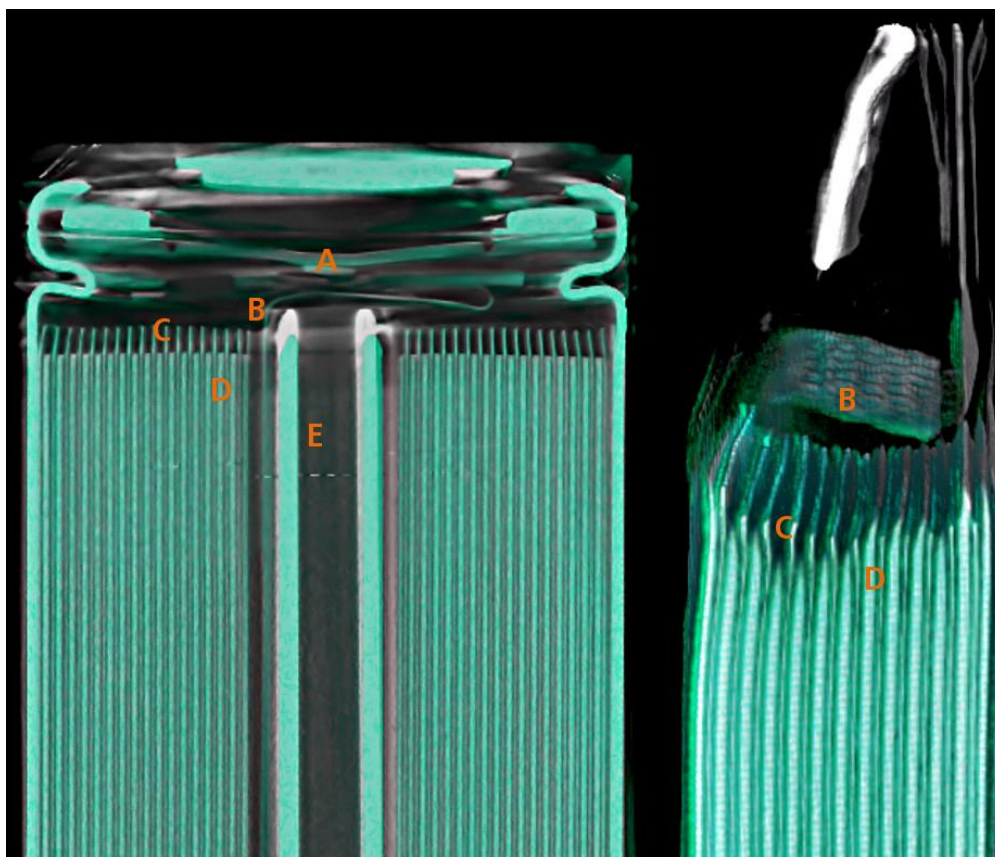
Figure 5.2 False color rendering of computed tomographies. Superimposed 3-D volume information of lithium-ion cells before (grey) and after (green) vibration in z-direction. While current interrupt device A, positive current collector B, anodes C and cathodes D remained unchanged, the mandrel E of the cylindrical cell was moved by vibrations. The superimposition is nearly complete so that underlying grey is readily visible only on the mandrel E of the cylindrical cell.

5.3 Current interrupt device damaged by vertical shocks

Cylindrical cells shocked in axial and radial direction as well as pouch cells shocked in y- and z-direction were investigated by computed tomography and Post-Mortem analytics. Shocks were carried out according to UN 38.3 T4. Damages could only be found in cylindrical cells shocked in axial direction while pouch cells showed no damage at all. Using µ-CT it could be shown that the current interrupt device of one cell was damaged. A comparison of the intact device before shock testing in Figure 5.3a) and the orange-marked magnification of the damaged device after shock testing in Figure 5.3b) shows considerable displacements.

The purpose of this device is highly relevant to security and merits a quick review. An intact current interrupt device consists of an upper inwards-curved metal cap with a weaker ring at the outer edges and lower perforated ring that are welded to the positive collector. If pressure is created inside of the cell, the upper cap is supposed to bend outwards, while the lower cap is supposed to remain in position as the gas passes

through its perforations. Due to the relative motion of the two plates, the current collector tab is to be torn of the upper plate, therefore opening the electric circuit. Should pressure build up further, the weak ring of the upper cap is then supposed to break, allowing gases to vent through the holes in the outer cover. Therefore, the mechanical placement of all its parts is critical to the safety of the cell.

As highlighted in the orange magnification in Figure 5.3b) both the upper and the lower caps of the current interrupt device were bent outwards. As no sufficient relative motion occurred, the current collector was not torn of the upper cap.

The damages on the current interrupt device have to be considered critical as the damages were detectable neither by visual inspection nor by means of electrical measurements and the cell would have passed the UN 38.3 T4 test. However, the device might have failed to disconnect the cell in a subsequent event such as an external shortcut or heating.
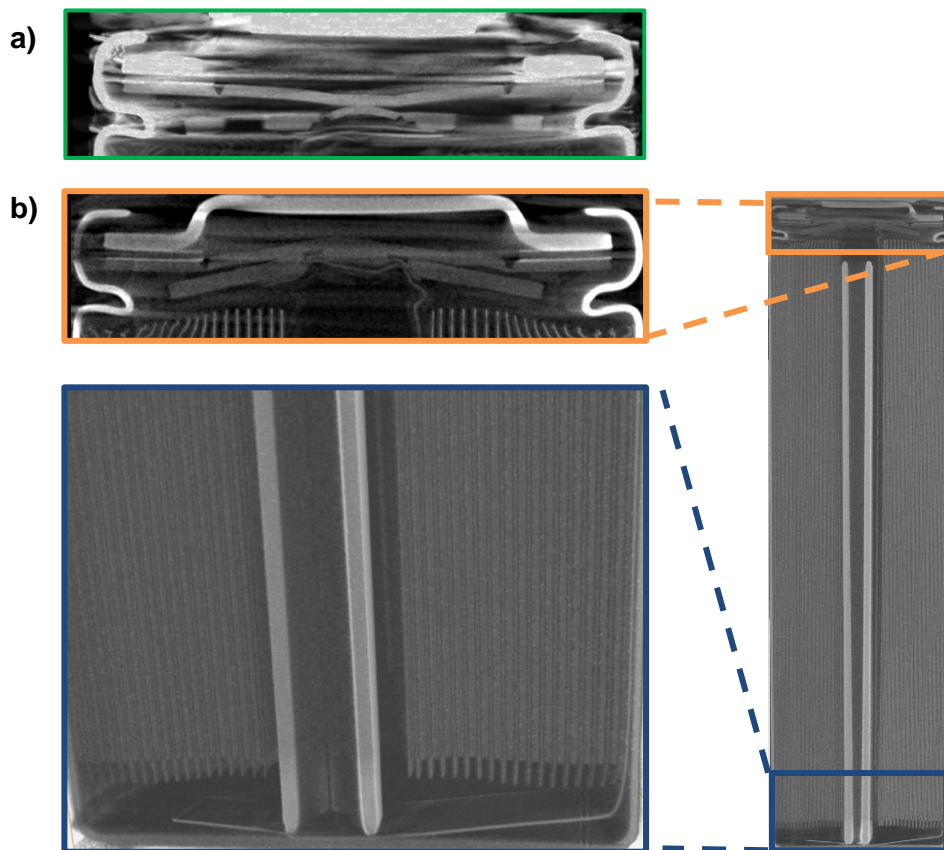
Figure 5.3 Current interrupt device a) before and b) after shock test. The computed tomographic image a) of an intact current interrupt device (green) is compared to b) a cell with damaged current interrupt device (orange). The damage was caused during shock testing according to UN38.3 T4. The mandrel acted as a battering ram and pierced the positive current collector tab (blue).

Close inspection showed that the displacement was caused by at least one forceful impact of the mandrel. Also, the jelly-roll was displaced upwards, deforming the separator, the current collector and parts of the electrodes. These observations show the potentially negative influence of voids inside a lithium-ion cell. Only due to this void could the mandrel gain the kinetic energy necessary to damage the current interrupt device.

5.4 Internal short-circuits caused by long-term vibrations

Pouch and cylindrical cells subjected to long term vibrations as described in a joint publication[11] were investigated. Once again, only cylindrical cells strained in axial direction were damaged, while pouch cells remained completely unchanged. Interestingly, the long-term vibrations caused a different damage pattern compared to the shock tests. While the shocks caused deformations of the current interrupt device, long-term vibrations caused damage to internal insulators.

Once again, the movement of the mandrel could be linked to the damages. Both the lower polymer insulation cap shown in Figure 5.4 a) and the polymer wrapping of the positive current collector tabs shown in Figure 5.4 b) were pierced. Figure 5.4 c) shows damages to the separator. As the insulators separating the jelly roll from the current collectors were damaged, a conductive pathway could be created by the mandrel. Damages to the negative separator visible in Figure 5.4 c) are evidence that an internal short-circuit through the mandrel took place.

The damage scenario, which was observed on both cells shaken in axial direction, was further corroborated by polarized light and scanning electron microscopy. The scanning electron micrograph of the damaged area shown in Figure 5.5 directly visualizes areas that appear to be molten. The polarized light micrograph also points to melting and subsequent changes in crystallinity. Using a first order retardation plate, changes in birefringence are visualized as changes in color.
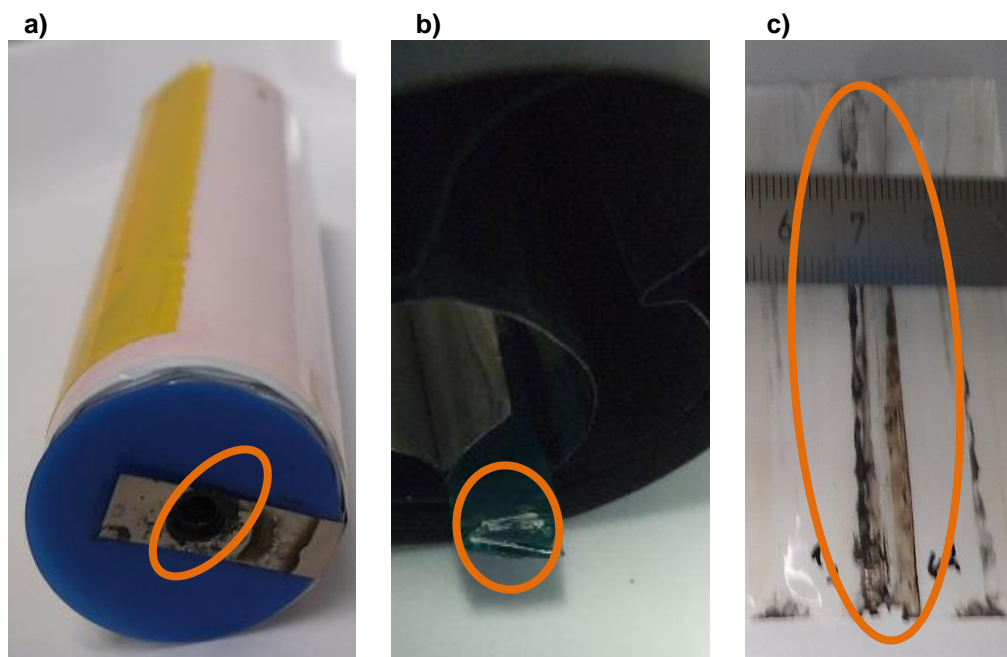
Figure 5.4 Damages to a cylindrical cell subjected to long-term vibrations. Movement of the mandrel caused damage to a) the blue insulation cap and the negative current collector tab as well as b) the insulation of the positive current collector tab. Damages to the separator shown in c) display signs of a thermal event. Photographs reproduced with kind permission of Elena Fleder, Fraunhofer ISC.

As visible in Figure 5.5 and Figure 5.6 a), the damaged areas appear colored while undamaged areas appear grey. This effect could be reproduced by manually causing a local short circuit in an otherwise undamaged cell. The result of this artificial short circuit, which was accompanied by sparking and visible melting of the separator, is shown in Figure 5.6 b). Similar color variations are produced. Polarized microscopy is a suitable tool for quick detection of thermal events in polyolefin separators that does not require any sample preparation. As several insulators were damaged and particulate matter was found in the cell, the exact pathway of the internal current is difficult to identify. The current may have passed from tab to tab, crossing the mandrel and debris. As the separator was damaged, direct electrical contact of an electrode to another electrode or to the mandrel was also possible. This result shows the risks associated with mechanical imperfections inside a cell.
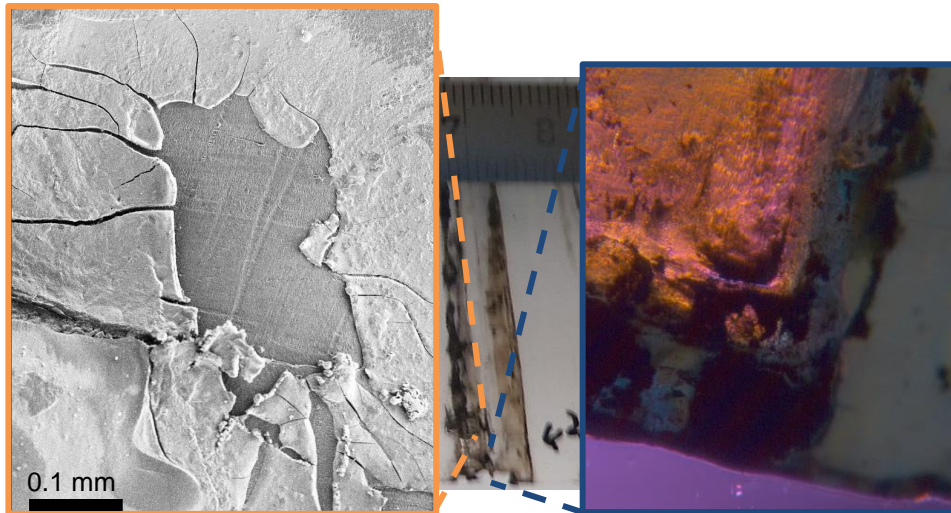
Figure 5.5 Evidence for thermal event in cell subjected to long-term vibrations.
Scanning electron (orange) and polarized light (blue) microscopy show that a thermal event took place in the vibrated cell. Molten areas are visible in the scanning electron image. Colored areas visible in the polarized light microscope point to local melting, as changes in crystallinity are linked to melting. Photograph and scanning electron micrograph reproduced with kind permission of Elena Fleder, Fraunhofer ISC.

The discussed damages were also found on the second cylindrical cell strained in z-directions. Once again, evidence for internal short circuiting was found. The short circuit also manifested in a sudden increase in resistance and a drop in retrievable capacity, that were measured at Technische Universität München.[11] Therefore it can be concluded that the investigated cylindrical cells are sensitive to long term axial vibrational strains. The resulting internal short circuits could be reproduced and linked to mechanical damage caused by the mandrel. Internal short circuits are a typical cause of thermal events[179,180] that is recognized to be especially dangerous because external circuitry cannot provide protection against it[181].
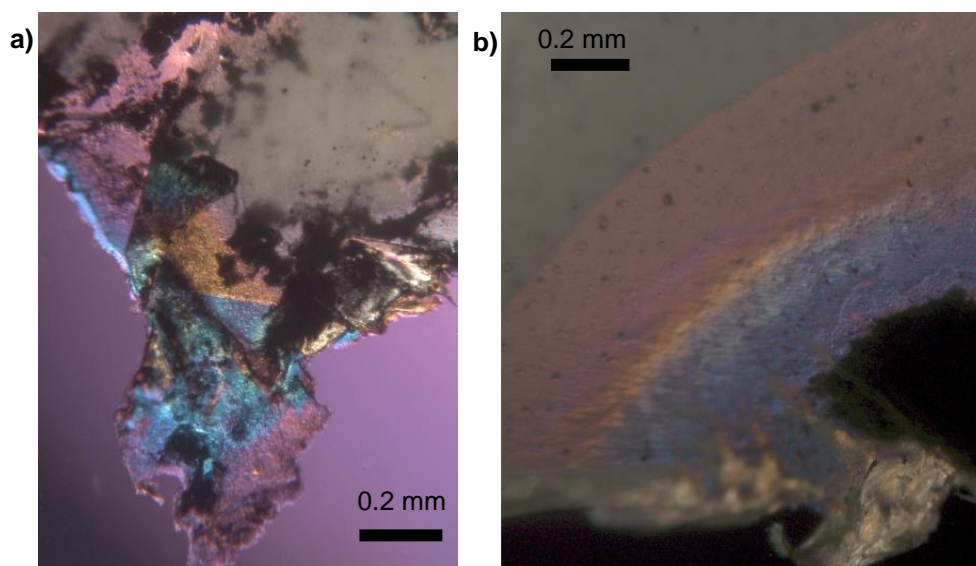
Figure 5.6 Separators with changed birefringence. Changes in birefringence of separators from a) a long-term vibrated cell and b) a cell with artificial short circuit are symptoms of localized thermal events.

5.5 Discussion

Investigations of cells subjected to vibrational strain clearly showed the robustness of the pouch cell design. Regardless of the orientation and nature of the vibration, no damages were caused to the internal structure of these cells. Considering the very harsh experimental conditions, reaching accelerations up to 150 g, it can be concluded that this cell type is not expected to be damaged by vibrations experienced in typical mobile applications. Pontus *et al.* investigated the impact of vibrations on bigger pouch cells with a nominal capacity of 12 Ah based on ISO16750-3[182] and also found all cells undamaged.[183] The cylindrical cells investigated in this study performed less favorable. While radial vibrations did not cause damage to the cells, axial shocks and vibrations caused diverse damages. Shocks according to the UN 38.3 T4 test protocol caused deformation of the current interrupt device, possibly destroying its safety-critical function. While this event is especially critical, the extreme accelerations with a magnitude of 150 g applied to small cells in the UN 38.3 T4 protocol are not expected to occur in bigger packs. This is reflected in a reduced test criterion for bigger batteries in the same protocol.[129] During long term vibrations, internal short circuits occurred. Using computed tomography and Post-Mortem analyses, the event was linked to the metallic mandrel. In the cells studied, a void above the mandrel formed a free pathway that allowed the steel tube to accelerate and build up momentum. The impacts and friction with current interrupt device, insulator caps and separator are shown to have caused the observed damages and security risks.

These reproduced faults reveal the mechanical weak spot of the design employed in the investigated cells. The unconstrained mandrel acted as a battering ram.

Furthermore, the metal tube may have acted as a conductive bridge in short circuit events. From the viewpoint of robustness to vibrations and shocks, the mandrel can be identified as the main safety threat. Using nonconductive, lighter materials and constraining its movement by filling out voids can effectively reduce the discussed risks.

Of course, the observed damages cannot be generalized to other cell types but general concepts can be derived. The advantages of lightweight, form fit design are visible in the pouch design. Despite the less sturdy design, the pouch cells performed more favorable. On the other hand, this design provides less protection against intrusion of exterior impactors. While this failure mode was not investigated in this work, it is recognized to be a considerable risk when electric vehicles crash and has been extensively studied in literature.[184] When packs are designed for applications with known vibrations, as is the case in power tool and mobile applications, cylindrical cells should be aligned perpendicular to the main axis of vibration, as cylindrical cells can be expected to be form fit in radial but not necessarily in axial direction.

Furthermore, the investigations carried out in this study show that the test protocols detailed UN 38.3 are successful in ensuring the mechanical safety of lithium-ion batteries. All cells could not only be safely stored and discharged but were also found to be free from defects that would lead to a later safety-critical event. On the other hand, they do not ensure long term stability as was shown by the long-term test carried out as well. Therefore, cells should be subjected to long-term vibration tests when indicated by the use-case.

The behavior at different states of charge and thus varying internal compression as well as the impact of resonance frequencies was not addressed in this work. While a first study on pouch cells concluded that both factors should have little impact on pouch cells,[185] other cell types might react differently. Furthermore, the robustness of connectors and packs are also an issue to be considered.[186]

6 Determination of battery state by ultrasonic probing[1]

In Sections 2 and 4 the state of charge, and more specifically the lithiation of graphite, was found to be a main aging factor in lithium-ion batteries. Furthermore, the determination of state of charge is of great importance for usability. Therefore, state of charge estimation is one of the most important features of battery management systems.[179,187] As laid out in the theoretical section 2.2.1, it is well known that the mechanical properties of lithium-ion batteries correlate with graphite lithiation and can be used to determine the state of charge. In contrast to other studies that rely on measurement of thickness[6,40] and stress[5,41] a new route is tested in this chapter. Using piezo transducers, ultrasonic pulses where transmitted through pouch cells and the responses were studied for possible changes upon charging and discharging of the battery.
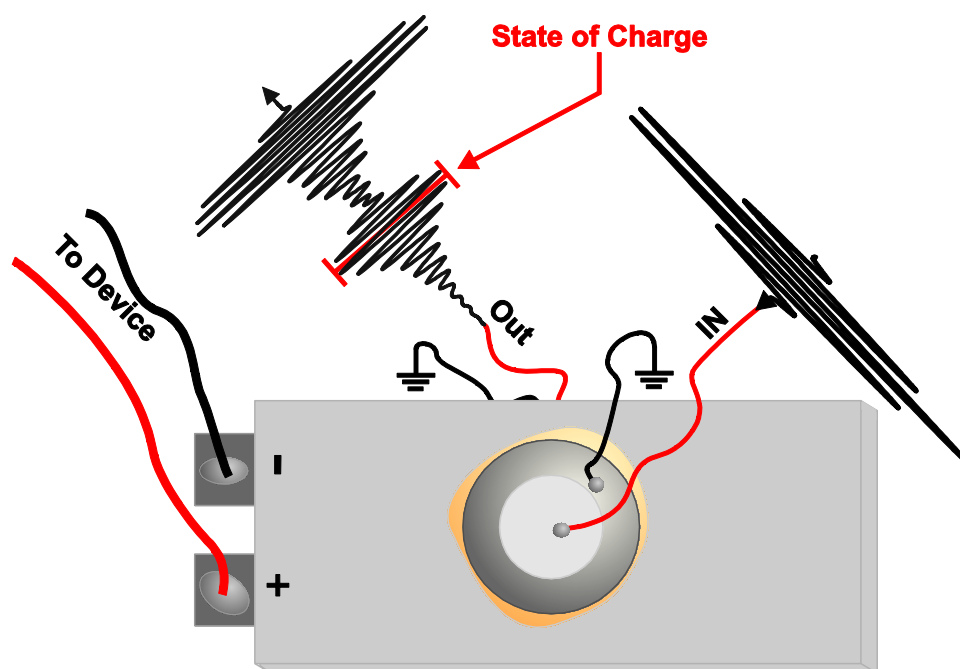
Figure 6.1 Principle of ultrasonic state of charge estimation. Off-the-shelf piezo transducers where glued on commercial pouch-type cells to characterize their state of charge by acoustic measurements. The transducers where placed in the center of the large faces of the cells to obtain optimized signals. A RC_N-impulse transmitted through the cell gives rise to two wave packages. The slower waves' amplitude is a linear measure for the state of charge.

6.1 Transmitted signals contain a measure for state of charge

6.1.1 First steps

A pouch-type lithium-ion cell with a capacity of 1.2 Ah was fitted with two piezo transducers by gluing them onto the surface as shown in Figure 6.1 and detailed in Section 3.1. Care was taken to ensure coaxial, central placement of the transducers. After solidification of the glue pulses with different frequencies between 100, 150 and 200 kHz were passed through the cell in fully discharged and charged state. In Figure 6.2, the measured signal amplitude is plotted as a function of time relative to the pulse emission. Two major wave packages were obtained in the charged state for all frequencies. Closer inspection of the signals shows that those signals contain useful properties.
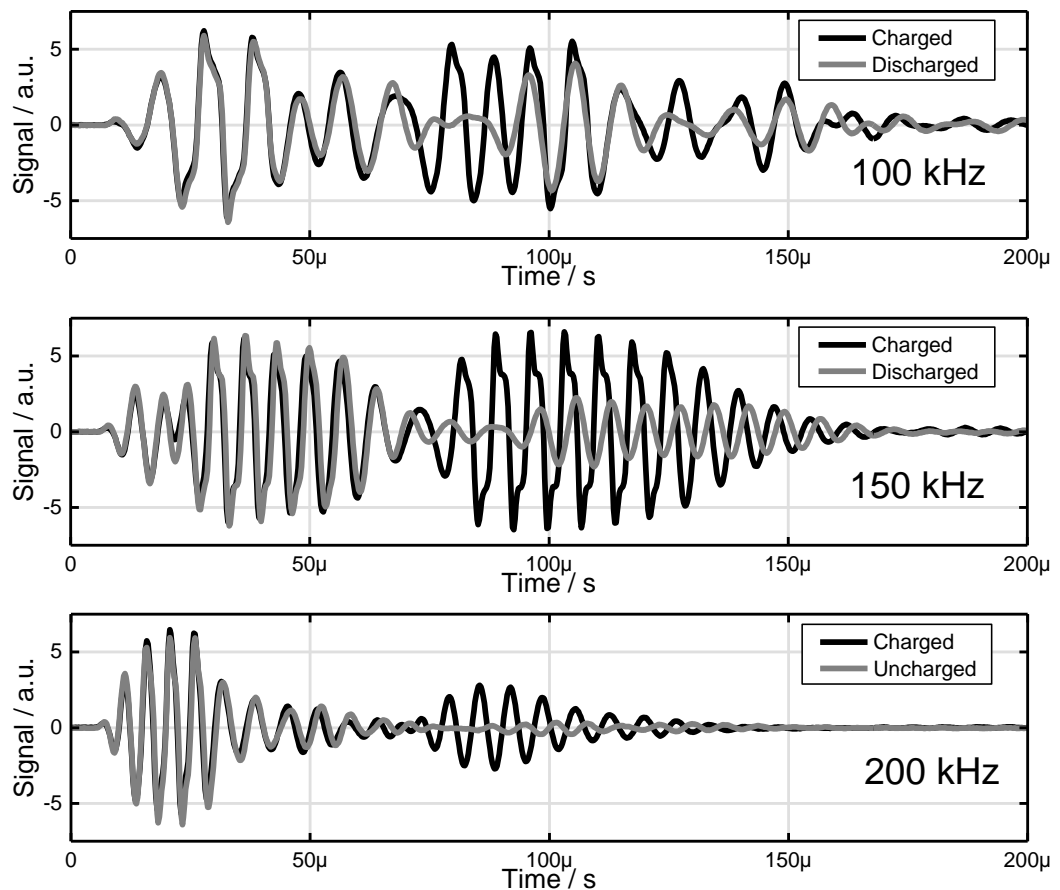
Figure 6.2 Response to raised-cosine pulses at 100, 150 and 200 kHz. The different pulses are transmitted through cells in charged and discharged state. The obtained waveforms contain invariant and responsive parts. Undesired pulse overlap depends on frequency, with best wave package separation at 200 kHz.

The signals at 100 kHz and 150 kHz are distorted, while the signal at 200 kHz appears to consist of two undistorted signals with different velocities. In the discharged state, the first wave amplitude is unchanged at all frequencies. In contrast, the second wave shows a dependence on frequency and state of charge. At 100 kHz, the second wave is only slightly depressed and the waveform is distorted. At 150 kHz, the second wave is diminished to about half of the amplitude when compared to the charged state.

At 200 kHz, the maximum amplitude is reduced to a tenth compared to the charged state. The maximum in the discharged state lays around 100 µs, while the maximum in the charged state can be found at approximately 85 µs. The waves are well separated in time making it easy to distinguish them. This behavior appears to be most favorable and has been examined in more detail.

6.1.2   Amplitude of the answer signal shows linear behavior

The important change in amplitude, the undistorted pulses and the difference in travel time at 200 kHz allow for easy discrimination between charged and discharged state. For robustness and facile automatic interpretation, it appears most advantageous to process the signal using basic operations. To simplify the data, it is converted to an unsigned format. Smoothing with a 24 µs wide Savitzky-Golay filter of second plynominal order further simplifies the signals and increases robustness against high frequency noise. While these operations could be carried out using analogue circuitry, they were carried out by digital post processing in this work. A smoothed representation of the signals modulus is shown in Figure 6.3. For the charged state three peaks are visible. The first peak is completely conserved in the answer signal generated by the cell in discharged state. The small shoulder with a delay of 50 µs is also virtually unchanged. In contrast, the third peak with an approximate delay of 90 µs has vanished.

It can be concluded from the presented measurements that the change in amplitude of the second mode within the investigated frequency range is most accentuated at 200 kHz. Furthermore, the obtained waveforms are easy to process. Therefore, additional tests were carried out using this signal frequency.
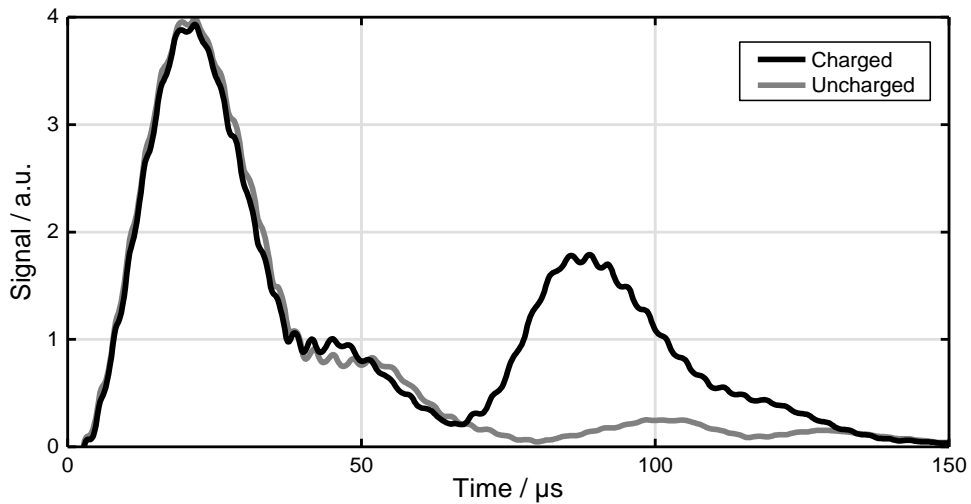
Figure 6.3 Smoothed signal modulus of a cell in charged and discharged state. A pulse with a frequency of 200 kHz was transmitted. The resulting answer signal was rectified and smoothed with a 24 µs wide Savitzky-Golay filter. The digital treatment highlights the invariant and state-dependent parts of the signals.

To prepare the cells for ultrasonic experiments, they were charged and discharged in steps of 20 % of nominal capacity using a current of 2 C and 4 C, respectively. After each step, the cells were probed using an ultrasonic pulse and the answer signals were rectified and smoothed. This smoothing was again obtained with 24 µs wide Savitzky-Golay filter of second polynomial order. Figure 6.4 shows the processed signals collected during charging. The answer signals obtained show a clear positive correlation.
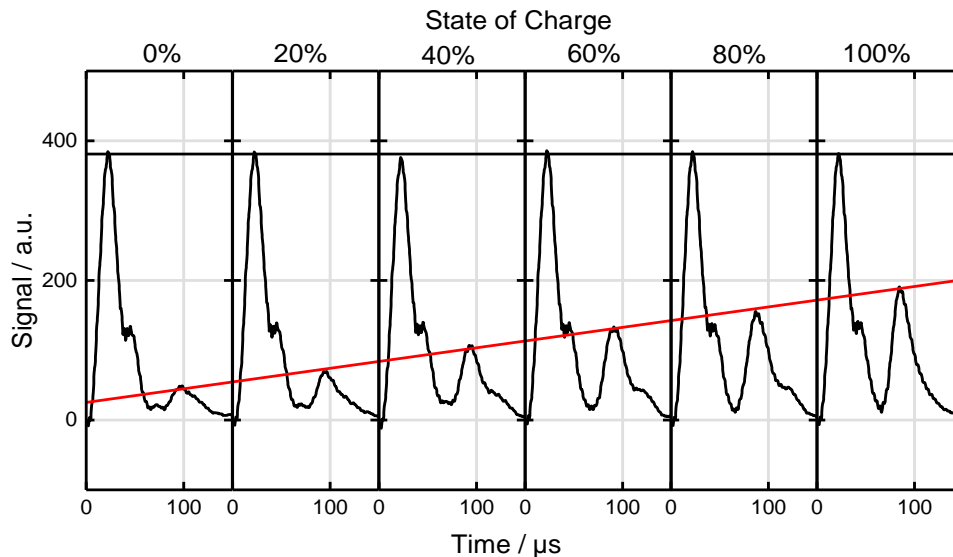
Figure 6.4 Rectified and smoothed responses to RC_N impulses at varied state of charge. As illustrated by a black and a red line, the peak height between zero and seventy microseconds is invariant to state of charge, while the peak height of the slower wave varies linearly.

The response can be divided into two parts: The early response with delays up to 70 μs and the later response which contains information on the state of charge up to 120 μs after the pulse has been sent. As illustrated by the black line, the first part of the signal is invariant with respect to the state of charge of the cell. On the other hand, the red line drawn over the slower peaks shows the dependence of the second part of the answer signal on the state of charge.

6.1.3 Integral signal and time-of-flight methods

To investigate the state of charge, other signal properties besides the maximum peak value after 70 μs may be used. The peak areas are accessible by integration and the apparent delay of the peak also shows dependence on the state of charge. Different methods may be preferable depending on the application and hardware situation.

When the voltage of the transducer is measured directly, or when current amplifiers are used, it is most straightforward to use signal levels. When very high sampling rates are available or analog peak hold circuits are used, the peak values may be detected directly. As this method uses only one discrete measurement, it is very sensitive to noise. Mild smoothing, for example using a low pass filter or digital methods such as moving averaging, can provide better noise rejection. Obtaining the modulus of the signal before smoothing allows for lower threshold frequencies, further improving noise rejection. Such a moving average was used in Figure 6.4. The moving average of the modulus with a bandwidth of 24 μs simplifies the data and makes it possible to use classic peak interpretation algorithms. Alternatively, the whole signal may be integrated, either by digital addition or using charge amplifiers. The integrated signals in Figure 6.5 exhibit two steps. The first step can be attributed to the fast wave, while the second one can be attributed to the slow wave. The integrated signal shows very low noise levels. Therefore, the sampling rate of the analog to digital circuit may be much lower than in direct methods. Using integration, it might be sufficient to sample once only. Once again, the relative stability of the first step is visualized by a black line, while the correlation of the second step height is visualized by a red line. Therefore, the integrated signal can also be used for determining the state of charge.
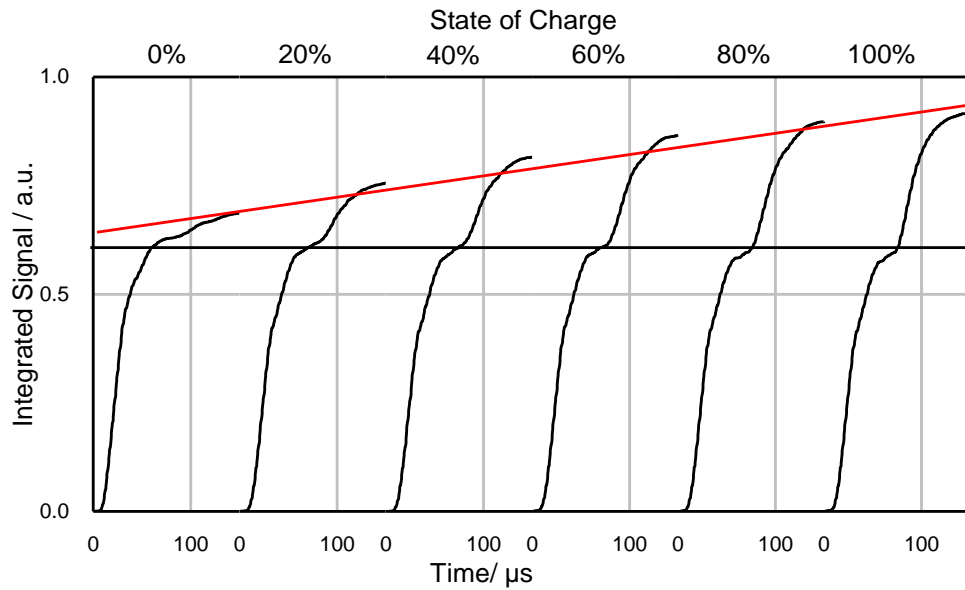
Figure 6.5 Integrated response signal at different states of charge. The red and black lines visualize the trends of the two steps. The steps are poorly distinguishable due to insufficient separation of the responses.

However, as the time separation of the two waves is relatively small, the steps are not well separated. Furthermore, the plateaus show considerable skewing. Both poor separation and skewing of the plateaus call for exactly defined evaluation times. This requirement is further complicated by a shift in the delay time of the second wave.

Interestingly, the relative delay of the peaks can also be used in a time-of-flight analogy. To illustrate this dependency, it is instructive to tilt the signal graphs already shown in Figure 6.4. Figure 6.6 shows the graphs with interchanged abscissa and ordinate. In Figure 6.6, the first wave is shown below, while the second wave is shown on top. The time of flight of the fast wave once again appears constant, while the delay of the slow wave varies with state of charge.
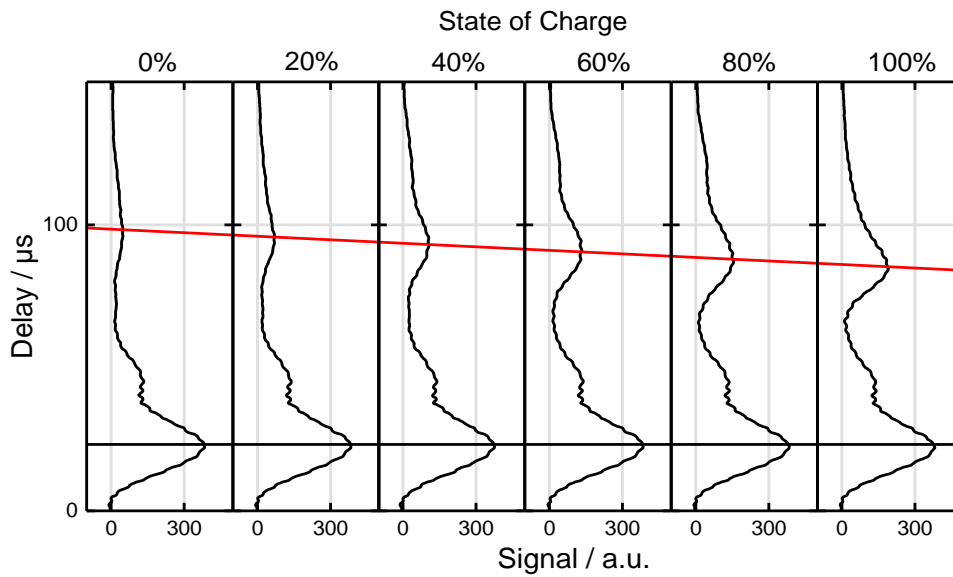
Figure 6.6 Evolution of the delay of the invariant and dependent responses. The slow wave shows a linear dependence on state of charge, while the delay of the faster wave appears to be constant.

To quantify the delays as a function of state of charge, the delays were estimated by peak picking of the smoothed and rectified raw signal. The obtained response delay of the fast wave is invariant to state of charge while the delay of the slow wave is proportional to the state of charge.

6.1.4 Synthesis of changing signal properties

The results from quantifying peak height, integral value and time-of-flight are compared in Figure 6.7. The obtained answer signals all contain a linear measure of the state of charge and a reference value. The first part of the responses shown in Figure 6.7 a) to c) can thus be used as an internal standard allowing to account for changes in the generated signal that are not attributable to state of charge as they could be generated by varying adhesion of the transducers and unstable voltage levels in the circuitry. The second part of the responses shown in Figure 6.7 d) to f) contains a measure for state of charge. In this work, peak height could be quantified with the best precision, as the integrated signal showed poor step separation and time-of-flight determination suffered from noise related deviations and insufficient sampling rates.
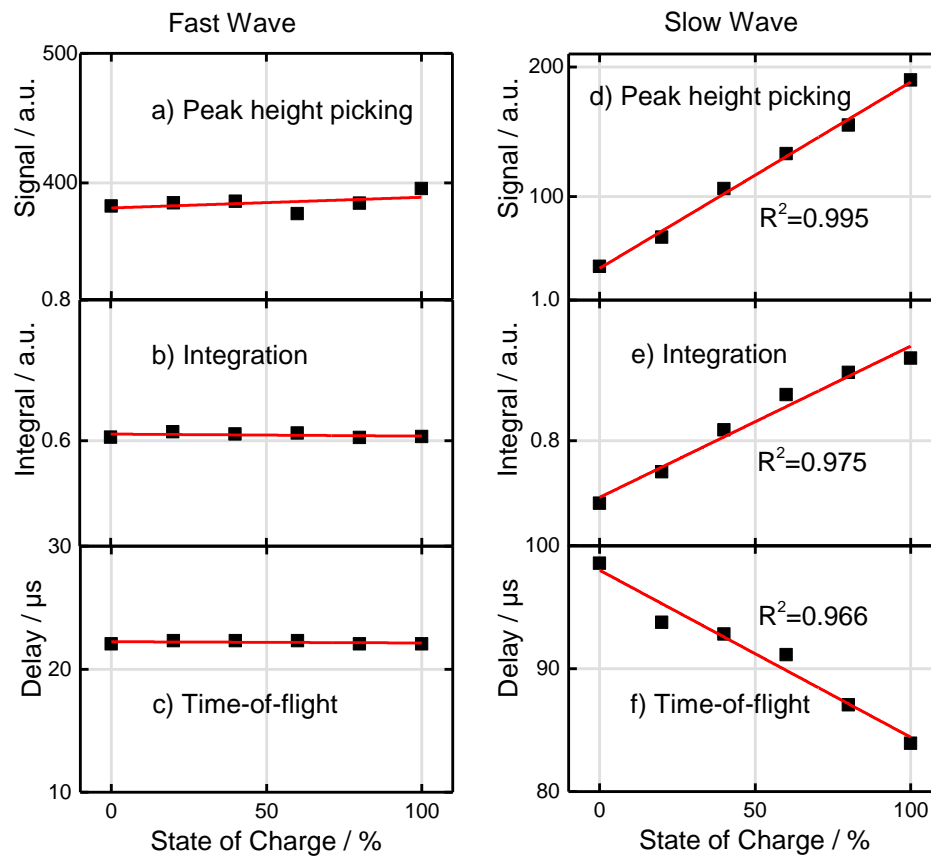
Figure 6.7 Comparison of different responses at varying state of charge. Peaks assigned to fast and slow wave are are compared in terms of peak height, peak area and delay. a) to c) show the invariance of peak height, integral signal and time-of-flight of the fast wave, while d) to f) show the linear dependence on the state of charge of the slow wave.
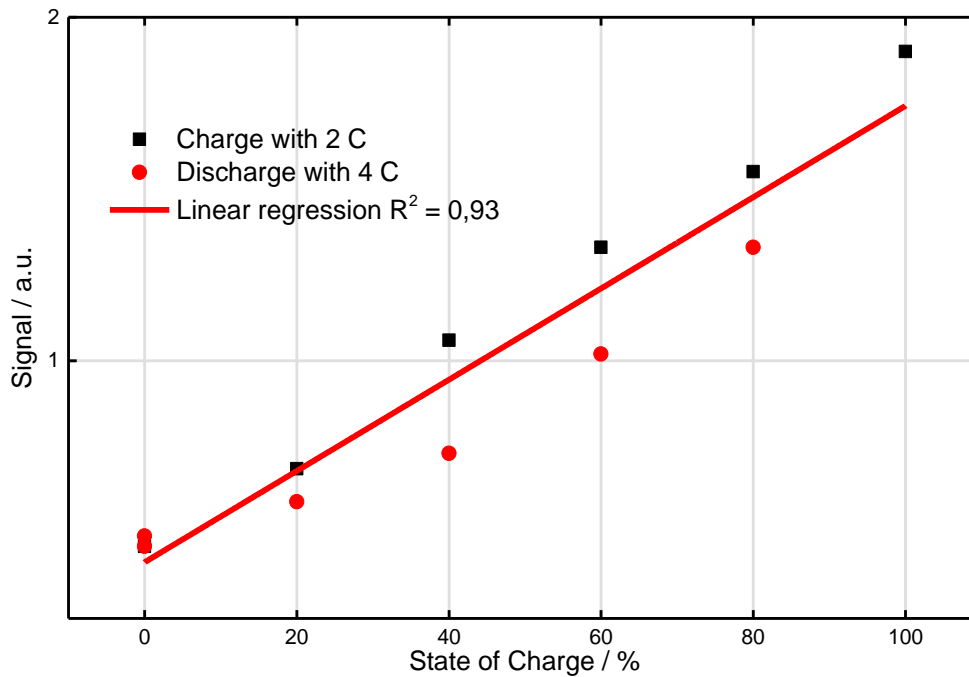
Figure 6.8 Signal height of the slow compressional wave plotted as a function of the state of charge The signals obtained from stepwise quick charging at 2 C (black) show a linear dependence on the state of charge while the signals obtained from stepwise discharging at 4 C (red) after a 30 minute rest period at 100 % state of charge show hysteresis.

In Figure 6.8 the signal height of the slow wave obtained by stepwise charging at 2 C is compared to those obtained from discharging at 4 C after a 30 minutes rest period at 100 % state of charge. A certain hysteresis is visible but the values near 0 % state of charge show good agreement. Hysteresis is common both in mechanical[40,188] and electrical[26,189] properties of lithium-ion cells. Therefore, knowledge about the impact of hysteresis on the discovered phenomenon is desired. Also, the dependence of hysteresis upon C-rates and cycling history is of interest and currently under investigation. The coefficient of determination obtained from overall regression is $R^2 = 0.93$ and the residuals are fairly distributed.

6.2   Explanation of the acoustic effects of state of charge

6.2.1   Effects on different scales

Body waves in fluid-filled porous media have been studied extensively and several attempts have been made to model them mathematically. Biot's theory is especially successful in predicting the observable parameters of transmitted waves. As discussed in Section 2.4.2, Biot's *Theory of Propagation of Elastic Waves in a Fluid-Saturated Porous Solid* establishes the presence of three waves in fluid-filled porous media and predicts their respective velocities and attenuations based on the mechanical properties of the porous frame and the liquid.[142,143] Based on mechanical properties of lithium-ion cells reported in literature, the theory will be used to understand the observed effects. As a first step, velocities predicted for the porous graphite electrode will be compared to experimental values. Then, the wavelengths will be compared to the characteristic length scales found in lithium-ion batteries. Based on these considerations a hypothesis for the underlying attenuation mechanisms will be developed.

To give the phase velocities of the waves, it is necessary to establish their respective path. Body waves are the easiest case, especially when the signal is focused along the normal axis of the transmitter. As the transducer planes are sufficiently large, placed parallel and centered, the travelled distance of the pulses can be approximated by the distance of the transducers. Surface waves and reflected signals complicate the received signal, as they may travel along different trajectories, possibly giving rise to several arrivals. For the following treatment, it will be assumed that both slow and fast wave packages are body waves travelling along the normal axis, an assumption that will be corroborated in the following section 6.2.3. Surface waves and reflected modes may also be present as additional minor oscillations but were neglected in this work because of their weak signal strength.

6.2.2   Velocity change predicted by Biot's theory

As discussed in Section 2.2.1, it is well known that graphite electrodes change their mechanical properties during charging, leading to near linear variation of crystallographic cell parameters and moduli. Here, the phase velocity of the slow wave and the variations caused by changing properties of the graphite are predicted. To show the general trends, Biot's low frequency approximation as discussed in Section 2.4.2 is applied only to the graphite electrode, and effects stemming from the layered structure of real cells are disregarded. For this rough estimation, ultrasonic properties of the cell are thus assumed to be uniform over the whole cell and equal to the graphite electrode's properties. All parameters and values for materials parameters of a graphite electrode are listed in Table 6.1. Most values were obtained from literature, while the shear modulus N_n as well as the bulk modulus k_b of the drained

matrix were estimated from fast wave's V_I and shear waves V_s velocities, which were found to be 3220 m s^{-1} and 460 m s^{-1}.

To understand the propagation of ultrasonic waves through the complex structure of real lithium-ion cells, the velocities in a graphite electrode are given as a function of porosity. In good correlation to the observed values, the fast wave is found to be nearly constant with respect to porosity. A change from 40 % porosity to 15 % leading only to a slight decrease from 3220 m s^{-1} to 3098 m s^{-1}. Once again in good accordance with experimental findings, the velocity of the slow wave is found to vary significantly. The estimated slow waves phase velocity in the graphite electrode as well as expected delays calculated from the velocity,

- the thickness of the cell of 7 mm,
- the approximated dead time of 4.8 µs,
- and the half peak broadness of 19 µs,

are represented in Figure 6.9. While the exact porosity change in the investigated cell is unknown, the observed change in delay time from 99 µs to 84 µs would imply a variation of porosity from 30 % to 20 %. This result compares well to typical porosities of approximately 30 % in unlithiated state and absolute variations in the range of 15-20%.[42]
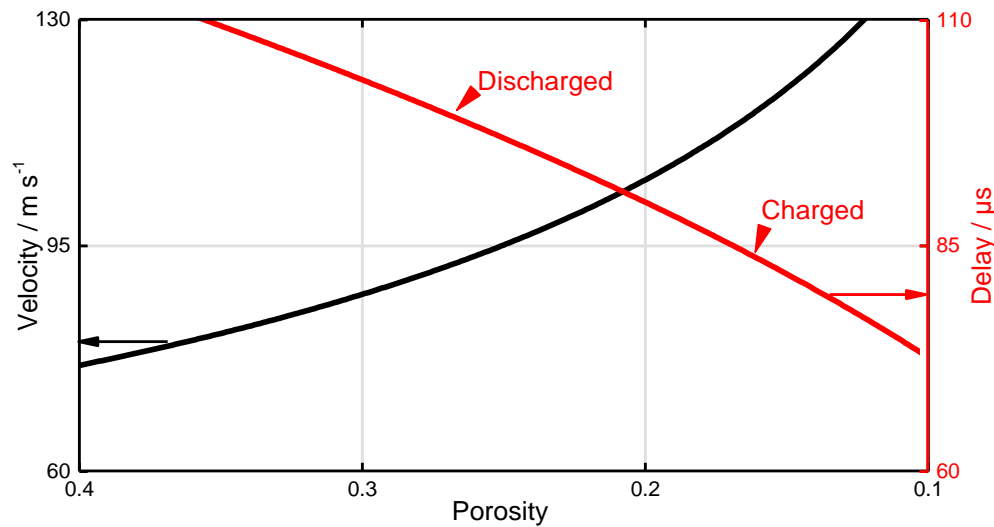
Figure 6.9 Phase velocity V_{II} in graphite electrodes as predicted by Biot's theory. Based on literature values resumed in Table 6.1, the phase velocity V_{II} of Biot's second wave is predicted as a function of porosity. From the velocity V_{II} and the cell thickness, 7 mm, the expected delay is approximated by taking a dead time of approximately 4.8 µs and a peak front broadness of approximately 19 µs. For this rough estimation, ultrasonic properties of the cell are assumed to be uniform for the whole cell and equal to the graphite electrode's properties. The observed trend compares well to experimental data obtained in Section 6.1.

As discussed in Sections 2.4.2 and 2.4.3, Biot's theory has been successful in estimating phase velocities but the apparent attenuation of the waves generally deviates from the predicted values due to the heterogeneity of real media. Therefore, the attenuation effects will be correlated to the change in wavelength induced by the velocity variation explained in this section.

Table 6.1 Parameters used for Biot theory. To investigate the behavior of the slow wave in a graphite electrode during charge, parameters from literature and own estimations were used. It was found that the second wave velocity is very sensitive to porosity changes.

Parameter	Abbr.	Value	Value obtained from
Shear modulus of drained matrix	N_n	0.392 GPa	Velocity of shear wave
Density of solid	ρ_s	2100 kg m^{-3}	Approximate value derived from[190]
Electrolyte Density 1.0 M LiPF6 in EC/EMC 1/1 (vol)	ρ_f	1270 kg m^{-3}	[191]
Tortuosity	α	2.5	Rough estimate due to anisotropy[192]
Darcy's coefficient of permeability	k	4.0 10^{-14}	[193]
Fluid viscosity	μ	42 mPa s	[193]
Porosity	β	10 % - 40 %	[42]
Bulk modulus of fluid	k_f	1 GPa	[193]
Bulk modulus of solid	k_s	29.3 GPa;	Based on[194]
Bulk modulus of porous drained matrix	k_b	17.4 GPa	Fast wave's velocity
Pore diameter	d	4 μm	Conservative Approx. from scanning electron measurements, section 4.2.1, Figure 4.5
Parameters depending on porosity change	**Abbr.**		**Value obtained from**
Mean density	ρ		Equation 12
Mass of solid per unit volume	ρ_1		Equation 13
Mass of fluid per unit volume	ρ_2		Equation 14
Mass coefficients	ρ_{11}, ρ_{22}		Equation 15 and Equation 16
Coupling coefficient	ρ_{12}		Equation 17
Coefficient b	b		Equation 20
Effective porosity	β_{eff}		Equation 18
Characteristic frequency	f_c		Equation 19
Parameters of dynamic properties	γ_{11}, γ_{22} and γ_{12}		Equation 21, Equation 22 and Equation 23
Parameters defining elastic properties	σ_{11}, σ_{22} and σ_{12}		Equation 24, Equation 25 and Equation 26
Reference velocity	Vc		Equation 9

6.2.3 Changing wavelengths lead to scattering effects on boundaries

In 1991, Carcione summarized the general behavior of acoustic waves in stratified media: "Wave propagation effects in stratified media depend on the wavelength of the signal. For wavelengths short compared to the dimensions of the layers, scattering in the form of coda waves is present. Thus, these wavelengths show dispersive behavior, i.e., the velocity is frequency dependent. On the other hand, at long wavelengths or low frequencies, the medium behaves as a nondispersive, smoothed, transversely isotropic material."[155]

Electrodes in lithium-ion batteries generally exhibit pore sizes in the order of few micrometers and layer thicknesses in the order of magnitude of a tenth of a millimeter.[195] From the measured delay times shown in Figure 6.7, the velocities and thus the wavelengths can be estimated, given the thickness of the cell of 7 mm, a dead time of approximately 4.8 µs and a peak front broadness of approximately 19 µs.

At 200 kHz, the wavelengths of the observed modes can be estimated to be greater than 20 mm for the fast wave and greater than 2 mm for the shear wave. The wavelength of the second pressure wave varies between 0.59 mm and 0.73 mm upon cycling of the state of charge.

According to the treatment provided by Carcione[155], the layered electrodes of the battery should appear as a smooth effective material to the fast compressional wave and the shear wave. However, as the slow pressure waves' wavelength at the utilized frequencies is close to the layer thickness in lithium-ion batteries, it is to be expected that a change of wavelength, either by frequency or velocity, leads to changes in behavior.

As shown in section 6.2.2, charging and discharging the battery varies the velocity and thus the wavelength of the slow pressure wave. By varying the frequency, the range of the ratio of the wavelength over the layer thickness can be scaled. So, by optimizing the frequency, it is possible to place the ratio in a monotonously increasing range. Then, an increase in velocity causes an increase in transmitted amplitude.

In this section, it will be shown that a variation of the ratio of wavelength over layer thickness does indeed yield comparable results, regardless whether it is caused by a variation of frequency or phase velocity.
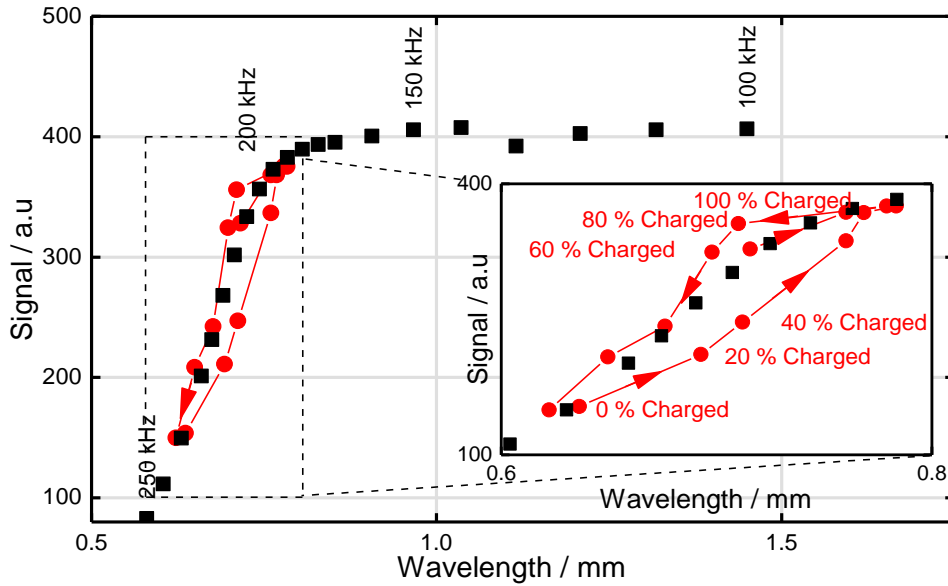
Figure 6.10 Height of the slow wave's peak plotted versus its wavelength λ_{II}. Signal heights are compared upon variation of excitation frequency on a cell as received from the manufacturer (black) and a subsequent full charge cycle (red). Wavelength was varied by change of frequency and velocity, respectively. The inlay visualizes the similar effect of varying wavelength by cycling and frequency change. Once more hysteresis induced by cycling is visible.

The comparison of changes induced by frequency change and cycling in Figure 6.10 explains the observed behavior. When the frequency is increased, the signal is constant up to 150 kHz, but as the wavelength approaches the order of magnitude of the layers, its attenuation suddenly increases dramatically. As discussed in the theoretical section 2.4.3, this behavior is well known and has been explained by scattering at the boundaries.[155] While the dispersive behavior depends on the complex properties of the porous materials and the interfaces, dispersion can be observed when the wavelength is sufficiently small compared to the effective periodic length of the heterogeneity.[146,155]

The inlay in Figure 6.10 shows that the change of velocity induced by cycling the cell leads to comparable effects as changing the frequency. This finding supports the theory that lithium intercalation changes material parameters, which in turn lead to velocity and wavelength variations that can finally result in dispersive effects. Therefore, this result implies that the method should be transferable to other cells containing non-zero-strain materials. Furthermore, this understanding helps finding the optimum frequency, as most useful signal variation can be obtained by choosing an excitation frequency yielding a wavelength in the transition to the scattering regime. This frequency can easily be found by a frequency variation experiment on a cell with known state of charge.

6.2.4 Application of the method to a lithium iron phosphate cell

In the previous chapters, it became clear that any cell chemistry should be accessible to ultrasonic charge estimation, as long as the cell features a layered design, porous electrodes and at least one active material with charge dependent properties. Therefore, the application to cells based on lithium iron phosphate and graphite is a logical step. Lithium iron phosphate features a very flat voltage plateau which makes it a very good power source.[196] On the other hand, the flatness of the voltage curve combined with voltage hysteresis effects makes estimation of state of charge based on voltage measurements very difficult.[179,196] Fortunately, many commercial lithium iron phosphate cells use graphite as the negative active material, which should allow for facile determination of state of charge by the ultrasonic methods developed in this work, therefore providing a new alternative to complicated model and filter based estimation technologies.

To demonstrate the methods applicability, a 2 Ah prismatic lithium iron phosphate cell with a graphite based negative electrode was equipped with piezo transducers and fully charged. As shown in Figure 6.11, the transmitted answer signal once again contained fast and slow modes. Given the cell thickness of 6 mm and a typical layer thickness of 10^{-4} m, the slow mode with a maximum near 100 µs is promising for charge determination. As the behavior is well comparable to findings in Figure 6.2, the developed method was transferred to the new cell type.
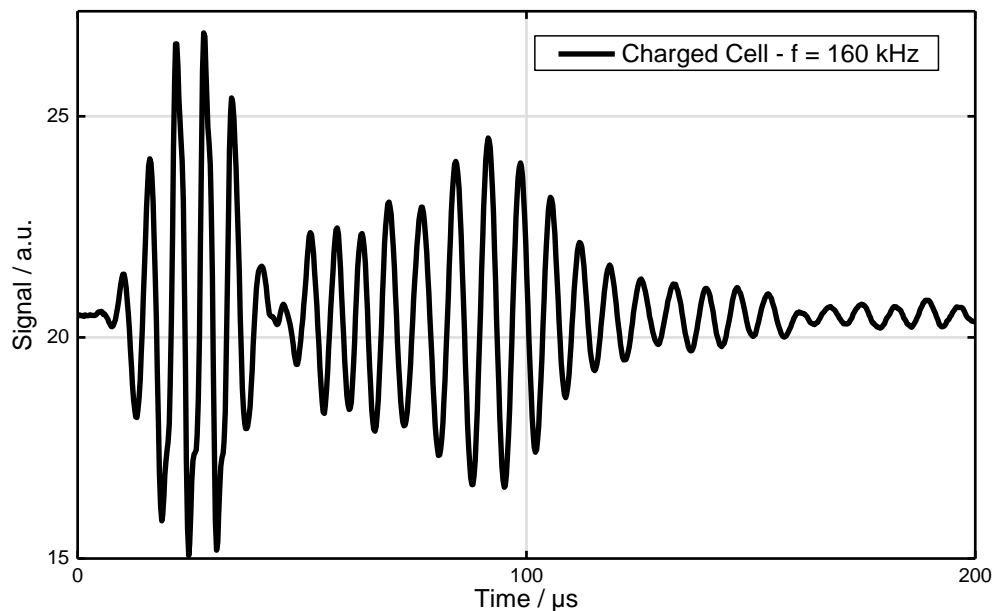
Figure 6.11 Transmitted signal in LFP based cell. Answer signal transmitted through a lithium iron phosphate cell. As observed with other cell types, fast and slow modes are visible. Based on the understanding gained in this work, the slow mode with maximum amplitude near 100 µs appears to be most promising, as its wavelength has the desired order of magnitude of one millimeter.

The optimal wavelength was determined by examining the frequency behavior in charged state. The peaks of the rectified and smoothed signal of the slow wave were picked as before and the result was plotted in Figure 6.12. As is obvious from Figure 6.12, a transition appears at wavelengths between 0.7 mm and 1 mm but additional effects cause another decrease at frequencies below 130 kHz. As higher frequencies yield better pulse separation and as the transition at lower wavelengths is steeper, a frequency of 160 kHz was chosen for charge estimation.
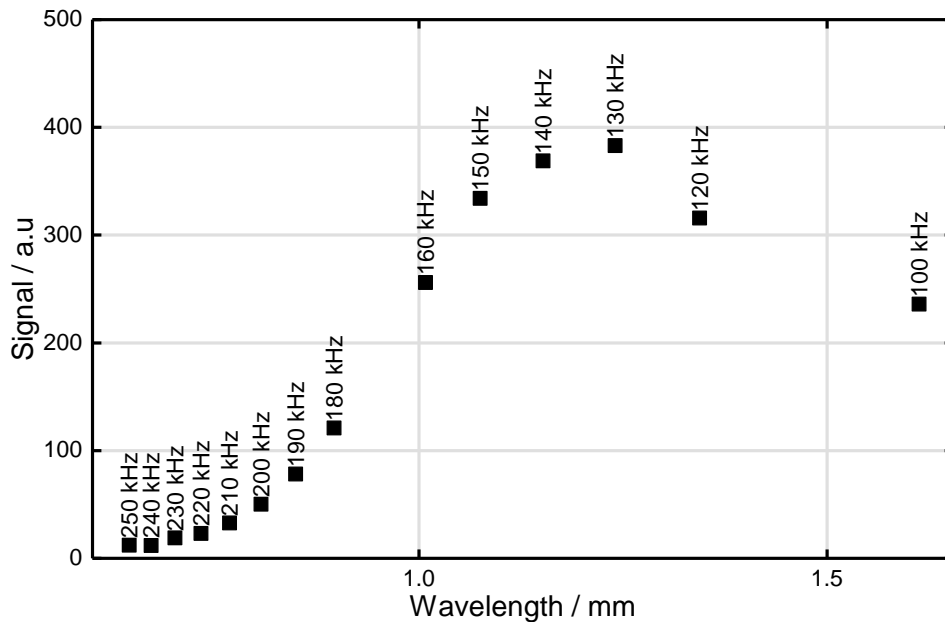
Figure 6.12 Wavelength dependency of transmitted signal in LFP based cell. Signal received from a charged lithium iron phosphate cell using pulses with different frequencies. The signal height was determined using peak picking. A strong dependency of the signal magnitude on the wavelength is visible.

The 2 Ah cell was discharged in steps of 0.4 Ah with a current of 5 A until the voltage cutoff of 2 V was reached. After each discharge step, the ultrasonic answer signal was measured. The resulting calibration line in Figure 6.13 shows the applicability of the method.

The obtained coefficient of determination $R^2 = 0,97$ allows for a good estimation from direct measurement but further refinement of signal processing as well as repeat measurements may further increase precision. This result shows the broad applicability of the method and demonstrates the procedure for quick determination of a suitable excitation frequency.
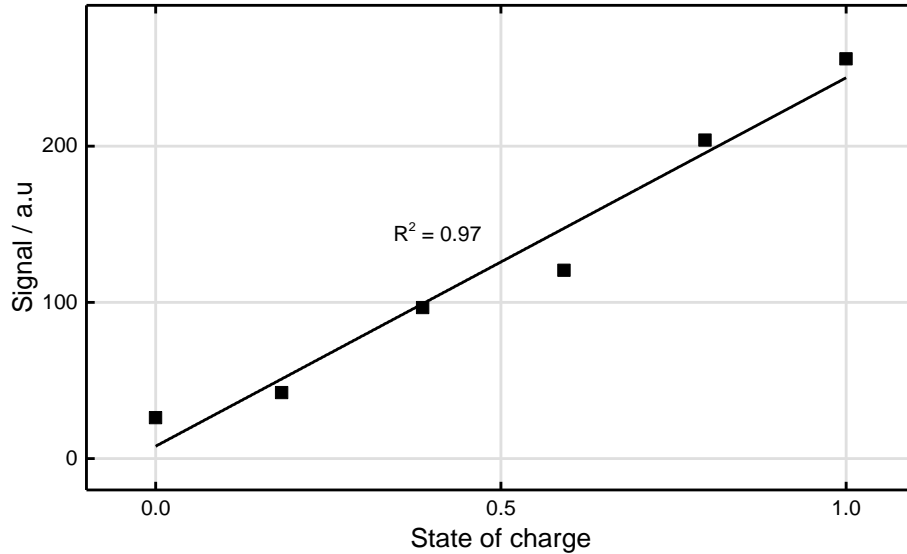
Figure 6.13 Linear dependence of signal to state of charge in an LFP cell. Signal received from a LFP cell using pulses with 160 kHz. The signal height was determined using peak picking. A linear calibration curve can be applied to estimate the state of charge by direct measurement.

6.2.5 Practical implementation of ultrasonic estimation of state of charge using a commercial microcontroller

It has been shown that ultrasonic pulses can be used to investigate the state of charge of different lithium-ion cells. In this section, it will be shown that signals of sufficient quality can be collected by a simplified implementation based on a commercial microcontroller. As in the laboratory setup, separate transducers in transmission geometry were used for signal generation and detection of the answer respectively. The setup is described in section 3.6.2.

As discussed in the theoretical section, the choice of an adequate function for signal generation is critical for minimizing distortions. Therefore, the RC_N-impulse already used in the laboratory tests is implemented. In digital applications, the function may be reproduced using pulsed or stepped signals. Higher sampling frequencies generally create better representations of the signal, but is also more hardware demanding. In this work, a stepwise approximation is realized using the digital-to-analog converter already integrated in the microchip. The maximum sampling frequency of the converter is utilized to minimize signal post processing. To realize such a high sampling rate with limited processing power, the desired signal steps were precalculated. The steps were sampled down to 7 bit values based on an exact impulse calculated from Equation 4 with $N = 5$. Exact and sampled down values are given in Figure 6.14a).
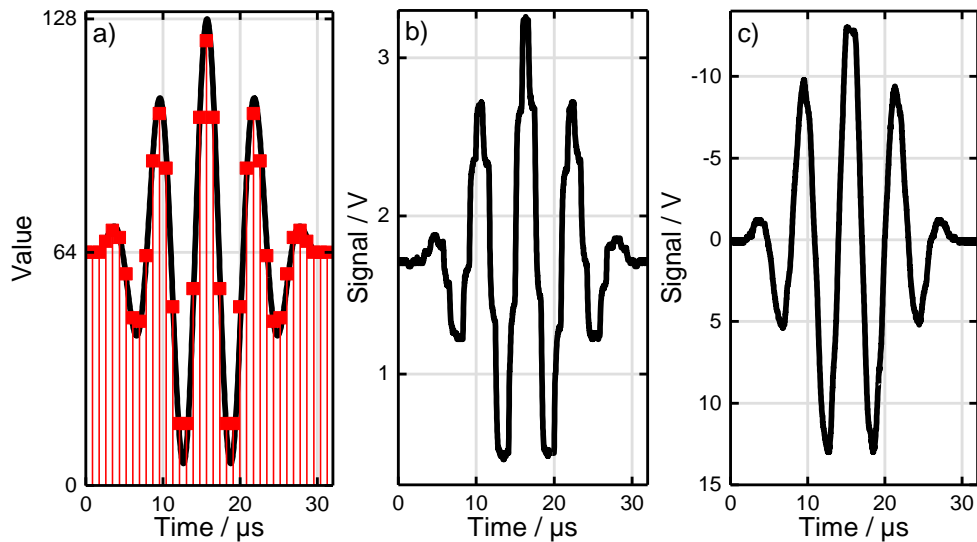
Figure 6.14 160 Hz RC_N-Signal from theory to transducer. a) Precalculated signal 7 bit values (red) are compared to the exact function. b) Output of the digital to analog converter as measured by oscilloscope. c) Output signal of the amplifier with transducer connected as measured by oscilloscope.

Using a simple lookup loop, the values are quickly transferred to the digital-to-analog converter. The waveform produced is shown in Figure 6.14b) and contains visible steps. Due to mild band-pass properties of the amplifier circuit, these steps are smoothed in the final signal which is fed to the piezo transducer. This signal in Figure 6.14c) compares well to the calculated function in Figure 6.14a).

Using a piezo transducer glued to the surface of the battery, the signal is converted to ultrasonic waves propagating into the lithium-ion cell. Two main modes take different times to travel to the second transducer and two slightly overlapping wave packages are recorded. The raw received answer signal shown in Figure 6.15a) exhibits peak to peak values below 0.1 V. Therefore, the signal is amplified before detection by the microcontroller's analog to digital converter. As shown in Figure 6.15b), the microcontroller running at 8 bit records the answer signal with good precision and a sampling rate of approximately 1 MSa s^{-1}. Also, the stability of the time base is sufficient using the internal clock of the processor only. From the obtained signal, the peak value in a suitable timeframe is recorded and transmitted along with the waveform shown in Figure 6.15a).
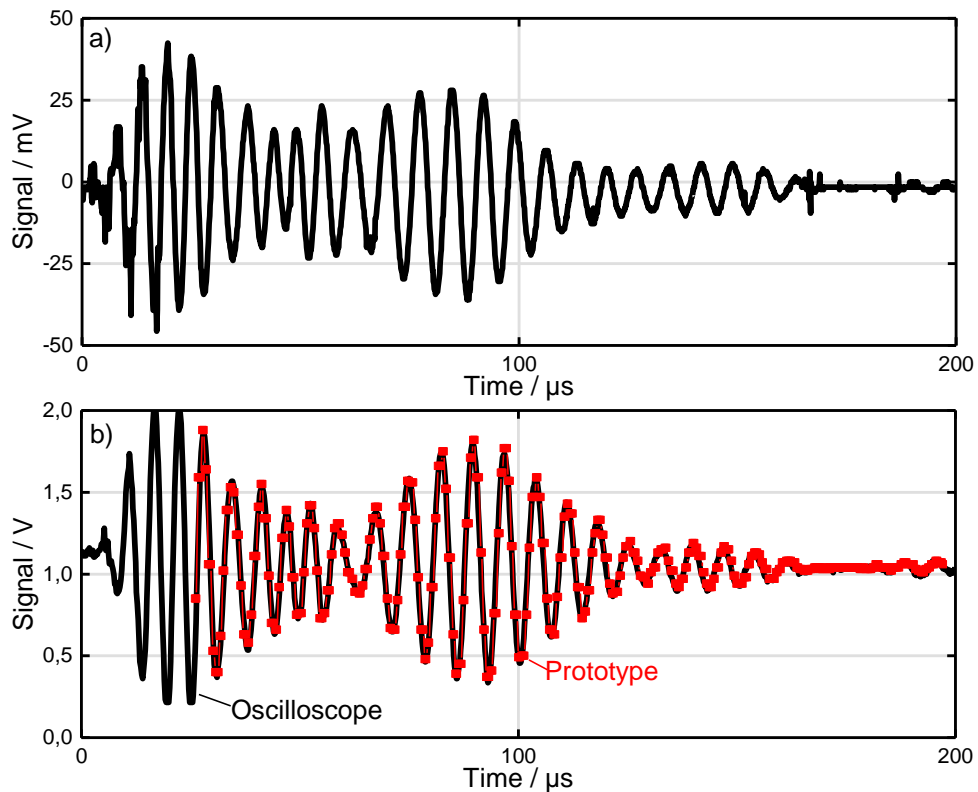
Figure 6.15 Received answer signal: Raw, amplified and measured. a) Raw answer signal received from the piezo transducer, measured by oscilloscope. b) Amplified signal measured by oscilloscope (black) and proof of concept (red). The proof of concept's microprocessor yielded a measurement dead time of 26 µs and a sampling interval of 0.335 µs, however the analog to digital converter operated at a lower rate. Overall, a useful sampling rate of 1 MSa s^{-1} was obtained at 8-bit resolution.

As has been shown in this chapter, peak height is a sensitive parameter to state of charge. In laboratory measurements, the peak height of the smoothed modulus of the answer was utilized for easy interpretation at different frequencies. Such an algorithm could also be implemented on the microcontroller, but the peak-to-peak amplitude provided also proved to be very stable and is very lean in memory space.

The obtained value can be used to display an estimated state of charge to the user and for the battery management system. As has been shown in this chapter, the obtained data is a direct indicator of state of charge. Therefore, a proof of concept based on cheap commercial-off-the-shelf electronics which allows direct state of charge estimation by the linear relationships described in this chapter was realized. Furthermore, the presented implementation is the base for further studies on the effect discovered in this thesis.

7   Summary & Conclusion

7.1   Impact of heterogeneous pressure on battery aging[1]

In this work, the causes for the sudden degradation of useable capacity of lithium-ion cells have been studied by means of complementary methods such as computed tomography, Post-Mortem studies and electrochemical analyses. The results obtained point unanimously to heterogeneous aging as a key-factor for the sudden degradation of cell capacity, which in turn is triggered by differences in local compression.

At high states of health, the capacity fade rate is moderate but some areas of the graphite electrode degrade faster than others. Still, the localized changes are hardly noticeable on cell level due to averaging effects. Lithium plating occurs first in unevenly compressed areas, creating patterns visible to the human eye. Inactive lithium, thick passive films and increased deposition of manganese and other metals washed out from the positive active material are found in affected areas of cells B and C, opened at the onset of sudden degradation and 150 cycles later, respectively. Micrographs of intact and defective areas of cell B are compared in Figure 7.1. The marked difference described before are visually obvious, as the defective area is entirely covered by a thick passive film. As lithium plating leads to rapid consumption of active lithium, a sudden drop in capacity is observed on cell level. Lithium plating appears to spread out from the initial areas over the whole graphite electrode, quickly consuming the remaining useful lithium and active graphite. It can be hypothesized that a self-amplifying circle of reciprocal acceleration of local lithium loss and material loss causes rapid local degradation. Positive active material facing large patches of defective negative active material cannot be effectively utilized anymore. Incremental capacity analyses on cell level may mislead to the assumption of degradation on the positive electrode, even if only the negative electrode has deteriorated.

Using Post-Mortem analyses, a clear cause-effect chain linking compression differences to local lithium plating is established qualitatively. Further studies are necessary to quantify the effect of compression. It is hypothesized that avoiding the initial local deposition of lithium metal can prevent the fatal kink in capacity retention. This can either be accomplished by more resistant negative active materials, robust cell design, or control measures avoiding critical states.

---

[1] This section has been published in parts under creative commons licence CC BY 4.0: T. C. Bach, S. F. Schuster, E. Fleder, J. Müller, M. J. Brand, H. Lorrmann, A. Jossen, G. Sextl, Nonlinear aging of cylindrical lithium-ion cells linked to heterogeneous compression, Journal of Energy Storage (2016), in press , http://dx.doi.org/10.1016/j.est.2016.01.003.
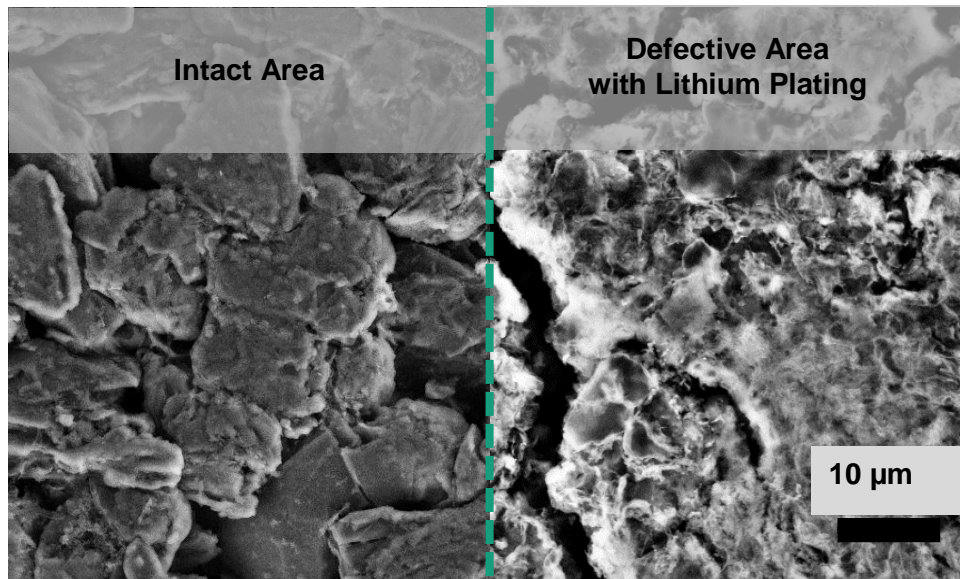
Figure 7.1 Scanning electron micrographs of defective and intact area of same cell. Within the same cell heavily defective areas with lithium plating and intact areas may coexist. Here micrographs of a defective area affected by compressive heterogeneity and an intact area of a cell in aging state B are shown. Micrographs reproduced with kind permission of Elena Fleder, Fraunhofer ISC.

Battery cell designers can improve cycle life by homogeneous pressure distribution in the cell and using negative active materials that are resilient to elevated discharge potentials as they appear in aged cells such as improved carbons or lithium titanate. Also, a sufficiently oversized negative electrode and suitable electrolyte additives can help to avoid lithium plating.[138,197] When packs are designed, care must be taken not to exert local pressure on parts of cells and to avoid both very high and low states of charge. High currents are expected to be most critical in cells with designs causing inhomogeneities.

To benchmark different cell and pack designs regarding the risk of sudden rapid degradation, cells can be cycled at maximum permissible voltage swing and charge and discharge amperage followed by Post-Mortem analysis. While localized lithium plating in limited areas is hardly detectable electrochemically, it can easily be detected by visual inspection. Based on our findings, the more cycles a battery can withstand this fast cycling regime without showing plating, the later it is expected to show rapid degradation. This test provides a relatively quick benchmark for an otherwise nearly unpredictable failure mode. The unfavorable performance of the cells investigated in this test explains why pronounced nonlinear behavior is found while other studies do not report such a behavior. Finally, the identified damaging control regimes allowing high currents in extreme states of charge are avoided in electromotive applications. It can be concluded that second life applications of automotive cells are not expected to be affected by compression-induced rapid deterioration as long currents are limited at critical states of charge in their second life, too.

7.2   Design considerations against vibrations and shocks[1]

The resilience of cylindrical and pouchbag cells to shocks and different vibrations was investigated. Stresses inflicted by vibration and shock tests according to the widely recognized UN38.3 transport test[129] were compared to a long-time test that exposed cells to a 186 days long ordeal of sine sweep vibrations with a profile based on real-world applications. For each test, cylindrical cells were shaken in axial and radial direction and prismatic cells were stressed in their longest axis and perpendicularly to their layered structure.

All cells passed visual and electric inspection performed by TU München after the vibration tests. Only cylindrical cells subjected to long-term vibrations in axial direction showed an increase in impedance and a loss of capacity that could be recuperated in part.[11]

The detailed analyses presented in this thesis gave more details on the damages inflicted by vibrations and shocks and revealed drastic damages in some cases. In cylindrical cells, only movement in axial direction caused damage. Long term vibrations were found to be especially detrimental and computed tomography exemplarily shown in Figure 7.2 revealed that the mandrel cut through insulations and the negative current collector.
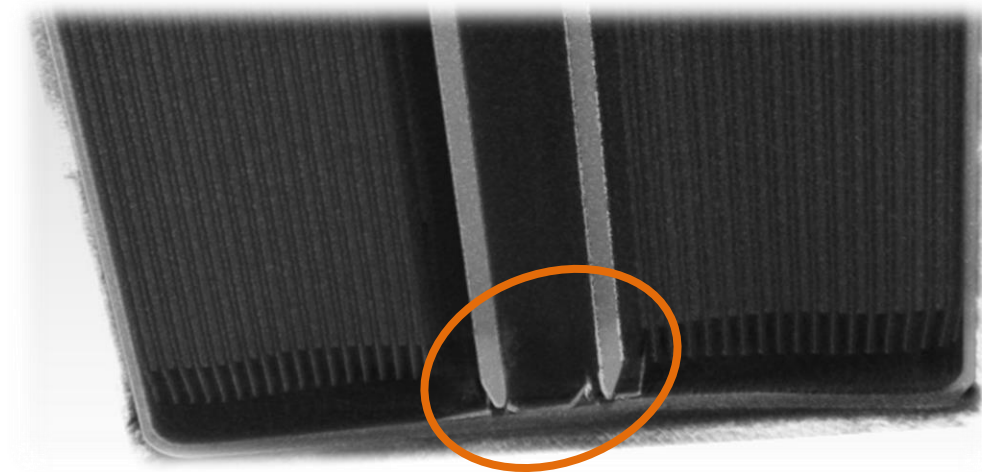
Figure 7.2 Computed X-Ray tomography of pierced current collector. During long term vibrations in axial direction, the mandrel pierced the insulation and negative current collector, thus creating pathways for internal short-circuits.

---

[1] Results presented in this section have been used for a joint publication, however no artworks or text have been reused: M. J. Brand, S. F. Schuster, T. Bach, E. Fleder, M. Stelz, S. Gläser, J. Müller, G. Sextl, A. Jossen, Effects of vibrations and shocks on lithium-ion cells, Journal of Power Sources (288, 2015), http://dx.doi.org/10.1016/j.jpowsour.2015.04.107

No damage whatsoever could be detected for pouch cells, regardless of the test protocol and the direction of movement. The extreme resilience of pouchbag cells is an important result of this study. It has been shown that the electrode stack of lithium-ion cells is resistant to vibrations, and that damages are caused by design imperfections that can be improved at low cost.

7.3 Using Ultrasound to probe anode state[1]

Since the invention of the lithium-ion battery and its commercial introduction, methods for state of charge estimation have been researched intensively. Although advanced methods based on complex algorithms such as Kalman filters have been developed, the limited data basis, measured current and voltage, still cripples the determination of state of charge. Especially in batteries with very flat OCV curves, such as lithium-iron-phosphate based ones, bookkeeping measures are used. This thesis has confirmed that aging of commercial batteries is dominated by degradation processes occurring on the graphite electrode. These degradation processes are highly dependent on the lithiation of the graphite active material, with both very low and high degrees of lithiation being detrimental.

The findings of this work, and the general state of research show that it is most crucial to control the lithiation and thus potential of the graphite electrode. A measure for intercalated lithium would also allow precise determination of state of charge independent from the positive electrode. As these measures are unavailable in commercial applications, control measures, runtime projections and aging studies have to rely on overall voltage and charge bookkeeping. Furthermore, in packs cells are connected in series and in parallel. These connections further complicate the determination of voltage and charge bookkeeping of the individual cells.

---

[1] This section has been published in parts in Journal of Power Sources: Gold, L., Bach, T., Virsik, W., et al. (2017), "Probing lithium-ion batteries' state-of-charge using ultrasonic transmission - concept and laboratory testing.", 343, 536–544. http://dx.doi.org/10.1016/j.jpowsour.2017.01.090 Copyright Elsevier (2017).
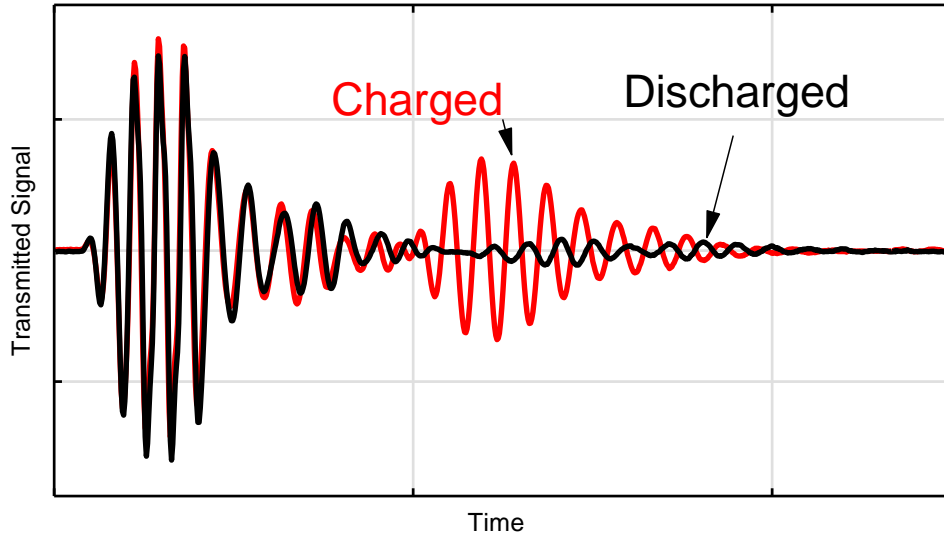
Figure 7.3 Transmitted sound dependent on state of charge When an ultrasonic pulse of appropriate waveform and frequency is sent through a lithium-ion cell, the transmitted signal exhibits two main wave packages. The first one is independent of state of charge, while the slow one changes in time-of-flight and magnitude. This change shows an approximately proportional relation to the state of charge.

In this work, a new, direct method for charge estimation based on changing transmission is presented. Transmitted signals through a charged (red) and discharged (black) cell are shown in Figure 7.3. A correlation between transmission of short ultrasonic pulses and state of charge is found. This new technology allows direct measurement of the state of charge. The method is demonstrated for batteries with different positive active materials, showing its versatility. As the observed changes can be traced to the lithiation of graphite, it can be determined without a reference electrode. By probing lithiation directly, a critical system property is made accessible in commercial batteries. Already at this early stage of development, the found correlations allow estimation of state of charge. The present hysteresis in the signal height of the slow wave, which is unneglectable especially during discharging at higher currents, will be subject to further investigation. For many applications, the hysteresis may be neglected, allowing for extremely simplistic evaluation units. In other applications, the observation of the rate dependent changes of the signal may give additional information on the state of the battery.

The observed effects can be explained by effects on different length scales, which are resumed in Figure 7.4. Biot's theory explains the second wave's slowness based on the active material particles size in the range of 0.01 mm and electrolyte-filled pores. Lithiation of graphite changes the porosity of the electrode and thereby the velocity and wavelength of the impulse. When the wavelength approaches the length scale of the layers, 0.1 mm, scattering effects dampen the transmitted signal. Finally, the wavelength of the pulse should be shorter than the transducers diameter to obtain a homogeneous wave front.
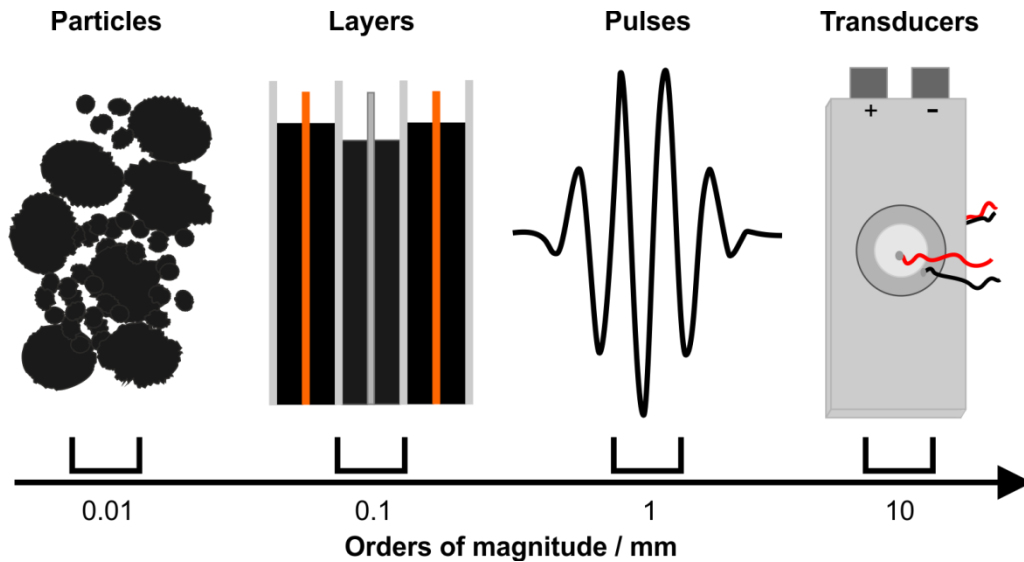
Figure 7.4 Different length scales in ultrasonic charge estimation. The observed behavior is explained by effects on different scales. The microparticles of the electrodes give rise to slow acoustic modes, and the layers cause attenuating effects when the wavelength of the pulses approaches their length scale. Finally, the size of the transducers influences the homogeneity of the acoustic field.

A proof of concept based on commercial-of-the shelf electronics shows the ease of integration into existing designs. Using low cost buzzers as transducers and a standard RISC microchip as integrated signal generator and evaluation unit, a functional state of charge estimator is realized. The used components are of very low cost and only a fraction of the pin and memory resources of the microchip are used. Microchips of similar types are already present in most mobile devices. As the resource use is low, it can be implemented into existing microchips without interference to its main tasks.

As the method does not rely on electric measurements on the cell, it is insensitive to parallel and serial connections as they are found in battery packs. As discussed before, cell level control is very costly, or even impossible, with conventional technologies. In contrast, low cost piezo buzzers can be used for ultrasonic determination of state of charge and galvanic isolation from the power circuits makes the method robust to electric topology. As a rapid direct measurement method is used, cells can be screened sequentially allowing multiplexing with one measurement logic only. To conclude, the new method allows the control of each individual cell in a pack independent from the electrical connections of the cells.

As the method shows great promise, further studies regarding factors such as long-term behavior, temperature and current rates should be conducted. In this thesis hysteresis was observed and a deeper understanding of the reasons behind it may allow further improvements of measurement precision.

8 Zusammenfassung

8.1 Einfluss ungleichmäßigen Druckes auf die Alterung

Im ersten Teil dieser Doktorarbeit wurden die Ursachen des plötzlichen Kapazitätseinbruchs von Lithium-Ionen Zellen untersucht. Die mittels sich ergänzender Methoden wie Röntgentomographie, Post-Mortem Untersuchungen und elektrochemischer Analysen gewonnenen Ergebnisse weisen darauf hin, dass heterogene Alterungseffekte eine Schlüsselrolle für den beschleunigten Kapazitätsverlust spielen. Die beobachteten Ungleichmäßigkeiten auf gealterten Elektroden konnten wiederum auf Kompressionsunterschiede zurückgeführt werden.

Im frühen Alterungsstadium war zwar nur ein moderater Kapazitätsverlust zu verzeichnen, einige Bereiche der Graphitelektrode altern jedoch schneller als andere. Diese lokalen Alterungseffekte sind auf Zellebene aufgrund von Mittelungseffekten zunächst schwer nachweisbar, sobald jedoch in Bereichen abweichender Kompression Lithiumplating auftritt, entstehen Muster welche nach Öffnen der Zelle gut zu erkennen sind. Inaktives Lithium, dicke Passivschichten sowie erhöhte Mengen an abgelagertem Mangan und anderen Metallen die aus dem positiven Aktivmaterial herausgewaschen wurden, konnten in geschädigten Bereichen der Zellen B und C, welche direkt beim Einsetzen beziehungsweise 150 Zyklen später geöffnet wurden, nachgewiesen werden. Elektronenmikroskopische Aufnahmen aus geschädigten und normal gealterten Bereichen der Graphitelektrode aus Zelle B werden in Figure 8.1 verglichen. Die beschriebenen Effekte werden durch die dicke Passivschicht veranschaulicht, die die Elektrode bedeckt.

Da Lithiumplating zu raschem Verbrauch von aktivem Lithium führt, kann ein plötzlicher Einbruch der Zellkapazität beobachtet werden. Das Lithiumplating scheint sich von den geschädigten Bereichen über die gesamte Elektrode auszubreiten, wobei rasch das verbleibende aktive Lithium und teilweise auch das negative Aktivmaterial verbraucht wird. Daher wird die Hypothese aufgestellt, dass durch lokales Lithiumplating ein sich selbst verstärkender Kreislauf in Gang gesetzt wird, wobei sich lokaler Lithium- und Aktivmaterialverlust gegenseitig beschleunigen. Positives Aktivmaterial welches größeren Bereichen durch Passivschichten deaktivieren Graphits gegenübersteht kann aufgrund stark verlängerter Diffusionswege nicht mehr effektiv zu Stromfähigkeit und Kapazität der Gesamtzelle beitragen. Inkrementelle Kapazitätsanalysen können daher zum falschen Schluss führen, dass auch das positive Aktivmaterial stark geschädigt wird, obwohl der Effekt durch großflächige Schädigung der negativen Elektrode ausgelöst wurde. Die Post-Mortem Analytik erlaubte es eine klare Ursache-Wirkungskette von lokalen Druckunterschieden über Lithiumplating zum Einsetzen der beschleunigten Alterung aufzustellen. Weitere Studien sind notwendig um den Effekt von Kompressionsunterschieden zu quantifizieren. Es kann davon ausgegangen werden, dass die beschleunigte Alterung

durch effektive Maßnahmen gegen lokales Lithiumplating vermieden werden kann. Dies kann durch robustere Aktivmaterialien, verbessertes Zelldesign und bessere Kontrolle der Betriebszustände von Lithium-Ionen Zellen erreicht werden.
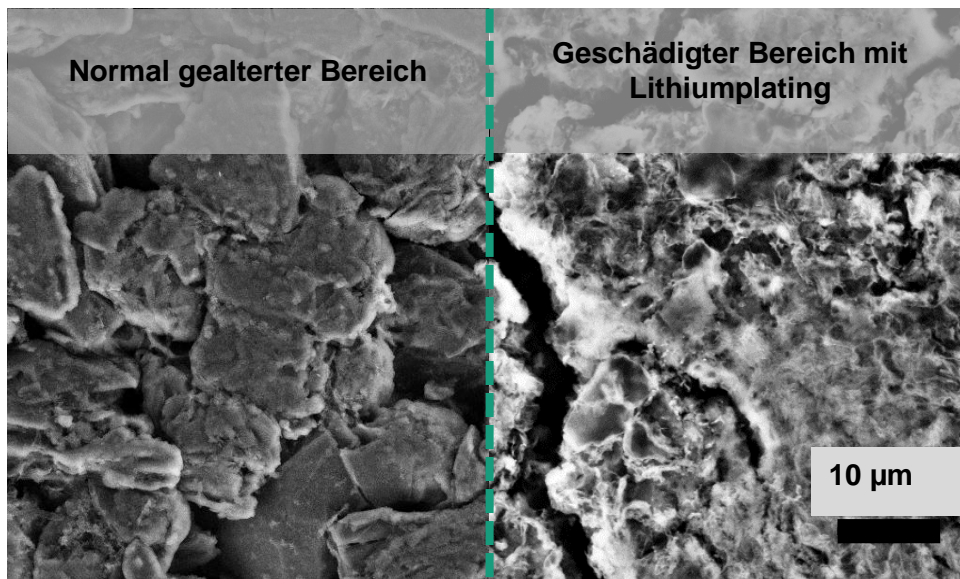

Figure 8.1 Rasterelektronenmikroskopien geschädigter und normal gealterter Bereiche der selben Zelle. Intakte und stark geschädigte Bereich mit irreversibel abgeschiedenem metallischem Lithium können auf derselben Elektrode koexistieren. Hier werden Mikroskopien eines durch lokale Druckheterogenitäten geschädigten Bereiches mit Aufnahmen eines normal gealterten Bereichs verglichen. Die Mikroskopie der Zelle B werden mit freundlicher Genehmigung von Elena Fleder, Fraunhofer ISC, abgebildet.

Bereits beim Design der Zelle kann die Zyklenstabilität verbessert werden, indem auf homogene Druckverteilung geachtet wird und Materialien mit verbesserter Potentiallage und Stabilität wie optimierte Kohlenstoffe und Lithiumtitanat eingesetzt werden. Weiterhin können ein ausreichender Kapazitätsüberhang der negativen Elektrode und Elektrolytadditive helfen Lithiumplating zu vermeiden.[138,197] Auch beim Packbau sollte darauf geachtet werden, überhöhte lokale Drücke zu vermeiden. Weiterhin sollten sowohl sehr hohe als auch sehr niedrige Ladzustände vermieden werden. Hochstromanwendungen sind bei inhomogenen Designs besonders kritisch.

Um Zell- und Packdesigns bezüglich ihrer Anfälligkeit für plötzlich beschleunigte Alterung einzustufen können sie bei größtmöglichem Spannungsfenster mit stark erhöhten Strömen schnellgealtert und anschließend per Post-Mortem Analyse untersucht werden. Während lokale Lithiumabscheidungen auf der negativen Elektrode nur schwer mit elektrischen Tests nachweisbar ist, kann es durch visuelle Inspektion der Elektroden leicht erkannt werden. Die in dieser Arbeit aufgezeigten Erkenntnisse lassen den Schluss zu, dass Zellen, die einem solchen aggressiven Schnellzyklisierungsprofil länger ohne Abscheidung metallischen Lithiums widerstehen können, auch wesentlich später beschleunigte Alterung aufweisen

sollten. Dieser Test kann also als schneller Benchmark für einen ansonsten bisher nicht vorhersagbaren Schadensmechanismus dienen. Das unvorteilhafte Abschneiden der untersuchten Zelle erklärt warum an ihnen ausgeprägtes nichtlineares Verhalten beobachtet werden konnte, während andere Studien keine solchen Beobachtungen ergaben. Schlussendlich kann festgestellt werden, dass die unvorteilhaften Betriebszustände mit hohen Strömen bei extremen Ladezuständen in Automobilanwendungen vermieden werden. Daher muss nicht davon ausgegangen werden, dass Second-Live Anwendungen von Zellen, Modulen und Packs aus Kraftfahrzeugen durch die hier beschriebenen Schnellalterungseffekte zwingend unwirtschaftlich werden solange in der Zweitverwendung die Ströme bei kritischen Ladezuständen begrenzt werden.

8.2 Designmaßnahmen gegen Vibration und Schock[1]

Die Widerstandsfähigkeit von zylindrischen und Pouchbagzellen gegenüber Schocks und Vibrationen wurde untersucht. Belastungen durch Vibrationen und Schocks gemäß des weitläufig anerkannten Transporttests UN38.3 [129] wurden mit 186 Tage dauernden Langzeittests verglichen. In den Langzeittests wurden die Zellen sinusförmigen Vibrationsprofilen, welche auf in Fahrzeugen gemessenen Vibrationen beruhen, ausgesetzt. Bei jedem Test wurden die Rundzellen in axialer und radialer Richtung, sowie die prismatischen Zellen entlang ihrer längsten Achse sowie senkrecht zu ihrer gestapelten Struktur belastet.

Alle Zellen bestanden die visuellen und elektrischen Überprüfungen die an der TU München nach Durchführung der Vibrationstests durchgeführt wurden. Nur die zylindrischen Zellen zeigten einen Anstieg des Innenwiderstands sowie einen weitgehend reversiblen Kapazitätsverlust.[11]

Die in dieser Arbeit vorgestellte tiefergehenden Analysen gaben ein detailliertes Bild der beobachteten Effekte auf und zeigten teilweise schwere versteckte Schäden auf, wobei ausschließlich in axialer Richtung belastete Rundzellen Schäden aufwiesen. Langzeitvibrationen führten zu besonders schweren Schadensbildern, so zeigt zum Beispiel das in Figure 8.2 dargestellte Computertomographische Schnittbild, dass der Mittelstab sich im Laufe der Belastung durch das Isolationsmaterial arbeiten und anschließend ein Loch in den negativen Ableiter stanzen konnte.
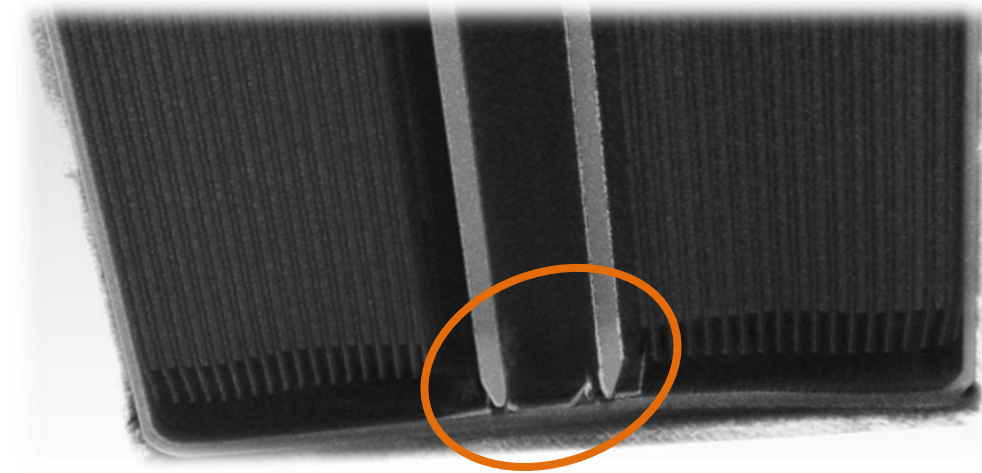
Figure 8.2 Computertomographie eines durchstoßenen Stromableiters. Durch die Vibrationsbelastung in den Langzeittests arbeitete sich der Mittelstab durch die in der Tomographie nicht erkennbare Isolation und den negativen Ableiter. In Verbindung mit weiteren Schädigungen an Separator und positivem Ableiter wurden so interne Kurzschlusspfade erzeugt.

Im Gegensatz zu den Rundzellen konnte an den untersuchten Pouchzellen unabhängig von Testprotokoll und Richtung der Belastung keinerlei Schädigung durch die Vibration festgestellt werden. Die sehr gute Widerstandsfähigkeit der Pouchzellen ist als wichtiges Ergebnis hervorzuheben. Es zeigt, dass der Elektrodenstapel, der die Grundlage jeder Lithium-Ionen Zelle bildet, äußerst Vibrationsstabil ist und auftretende Schäden auf ungenügendes Zelldesign zurückzuführen sind. Die zugrundeliegenden Fehler, wie nicht kraft- und formschlüssig verbaute Zellelemente, können mit geringem Kostenaufwand vermieden werden.

8.3   Sondierung des Anodenzustands mittels Ultraschall

Seit der Erfindung der Lithium-Ionen-Batterie und ihrer kommerziellen Einführung wurde intensiv an Methoden zur Bestimmung des Ladezustands geforscht. Obwohl auf fortgeschrittenen Algorithmen wie Kalmanfiltern beruhende Methoden zur Verfügung stehen, stellt die begrenzte Messdatenbasis, Strom und Spannung, ein Hindernis bei der Bestimmung des Ladezustands dar. Besonders in Batterien mit sehr flachen Spannungskennlinien, wie zum Beispiel Lithiumeisenphosphatzellen, beruht die Ladezustandserkennung wesentlich auf der aufwändigen und fehleranfälligen Ladungszählung.

Die vorliegende Arbeit bestätigt, dass die Alterung kommerzieller Lithium-Ionen-Batterien durch Nebenreaktionen auf der Graphitelektrode dominiert wird. Diese Prozesse sind stark vom Lithiierungsgrad und elektrochemischen Potential der Graphitelektrode abhängig, wobei sowohl sehr hohe als auch sehr niedrige Lithiierungsgrade abträglich sind.
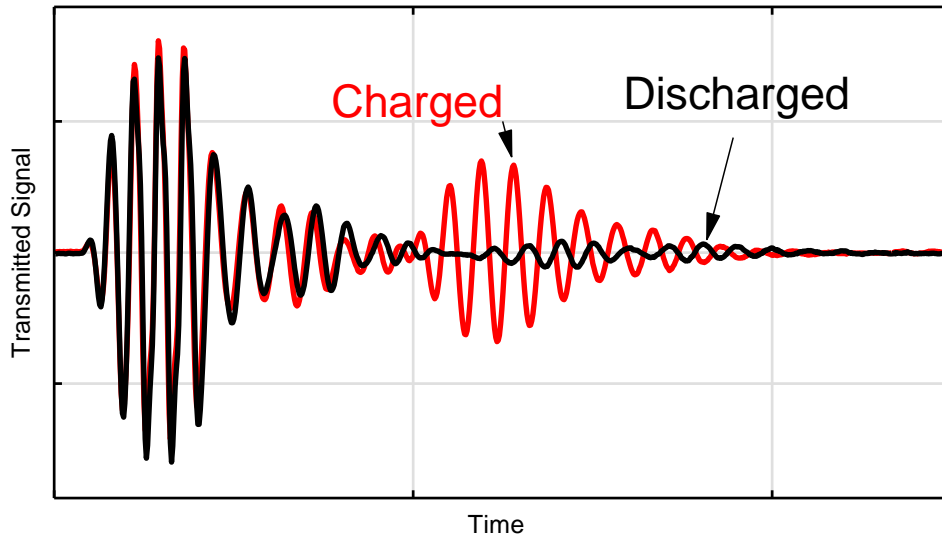
Figure 8.3 Ladezustandsabhängige Schalltransmission. Wird auf die Oberfläche einer Lithium-Ionen Zelle ein geeigneter Ultraschallpuls aufgeprägt, enthält das transmittierte Antwortsignal zwei wesentliche Wellenpakete. Das zeitlich erste ladezustandsunabhängig während das zweite sowohl Amplituden- als auch Laufzeitänderungen erfährt und beide Größen einen näherungsweise linearen Zusammenhang mit dem Ladezustand aufweisen.

Die vorgestellten Ergebnisse und der Stand der Wissenschaft zeigen die große Bedeutung der Kontrolle von Lithiierungsgrad und Potential der Graphitelektrode auf. Ein Maß für die Menge des im Graphit interkalierten Lithiums würde weiterhin unabhängig vom Aktivmaterial eine präzise Ladungszustandsanzeige ermöglichen. Da jedoch kommerzielle Zellen über keine Referenzelektroden verfügen, sind mit klassischen Methoden Potential und Lithiierungsgrad der Graphitelektrode nicht zugänglich und Regelung, Reichweitenschätzung und Alterungsabschätzug müssen auf Grundlage von Klemmenspannung und Ladungszählung durchgeführt werden. Die elektrische Topologie von Batteriepacks mit parallelen und seriellen Anordnungen von Zellgruppen kompliziert die Bestimmung auf Zellniveau weiter.

In Kapitel 6 wurde eine neue, direkte Methode zur Ladezustandsbestimmung vorgestellt. Die Transmission kurzer Ultraschallpulse durch eine geladene (rot) und eine ungeladene Zelle werden in Figure 8.3 verglichen. Die beobachteten Amplituden- und Laufzeitänderungen zeigen eine näherungsweise lineare Abhängigkeit vom Ladezustand der untersuchten Zellen und können somit zu dessen Bestimmung genutzt werden. Diese neue Methode erlaubt die direkte Bestimmung des Ladezustands von Lithium-Ionen Zellen und die Anwendbarkeit konnte an Zellen mit verschiedenen positiven Aktivmaterialien gezeigt werden. Da die beobachteten Transmissionsänderungen auf den Lithiierungsgrad der Graphitelektrode zurückzuführen sind, kann dieser mittels Ultraschall auch ohne Referenzelektrode modellfrei bestimmt werden.

Durch die direkte und zerstörungsfreie Charakterisierung der Graphitlithiierung kann eine der kritischen Systemgrößen kommerzieller Lithium-Ionen Zellen ohne Eingriffe und im Realbetrieb bestimmt werden. Bereits in dem hier präsentierten frühen Entwicklungsgrad, erlauben die erhaltenen Korrelationen trotz vorhandener Hysterese eine gute Abschätzung des Ladezustands. Für viele Anwendungen, erscheint die beobachtete Hysterese vernachlässigbar, was sehr unkomplizierte Auswerteeinheiten möglich macht. Wird eine höhere Präzision unabhängig von Lade- und Entladeraten angestrebt, kann das Hystereseverhalten berücksichtigt werden. Weiterhin bietet die Erforschung der Hysterese neue Ansätze zum tieferen Verständnis der dynamischen Vorgänge in Lithium-Ionen Zellen.

Die beobachteten Effekte können durch Vorgänge auf verschiedenen Längenskalen zurückgeführt werden, die in Figure 8.4 zusammengefasst sind. Biots Theorie bietet eine Erklärung der geringen Geschwindigkeit der zweiten Welle aufgrund der Ausbreitungsmodi der Schallwellen im porösen, elektrolytgefüllten Aktivmaterial. Die im Vergleich zur Wellenlänge kleine Längenskala der Aktivpartikel und der elektrolytgefüllten Poren von 0,01 mm führt hierbei dazu, dass sich das Material als Effektivmedium verhält. Durch die Lithiierung der Graphitpartikel ändern sich Eigenschaften und Porosität der Elektrode. Insbesondere die Porositätsänderung kann laut Biots Theorie die Geschwindigkeit und somit die Wellenlänge der zweiten Welle wesentlich verändern. Wenn die Wellenlänge auf die Größenordnung der Schichtdicken der Zelle, 0,1 mm, reduziert wird, treten Streuungseffekte auf, die die transmittierte Welle abschwächen. Schlussendlich muss der Durchmesser der eingesetzten Schallwandler größer als die Wellenlänge der Pulse sein um ein homogenes Schallfeld zu erzeugen.

Ein Demonstrator auf Basis elektronischer Standardbauteile zeigt die einfache Integration des Konzepts in bestehende Designs. Mittels kostengünstiger Piezosummer und eines RISC Mikrochips als Signalgenerator und Auswertungseinheit wurde ein funktionsfähiger Ladezustandsschätzer realisiert. Die eingesetzten Komponenten sind kostengünstig und nur ein kleiner Teil der Pins und des Speichers sind für die Umsetzung nötig. Da solche Mikrochips in elektrischen Anwendungen bereits weitverbreitet sind und die Methode sehr ressourcenschonend ist, könnte die Methode einfach auf vorhandenen Bauteilen integriert werden ohne mit deren Hauptaufgabe in Konflikt zu treten.
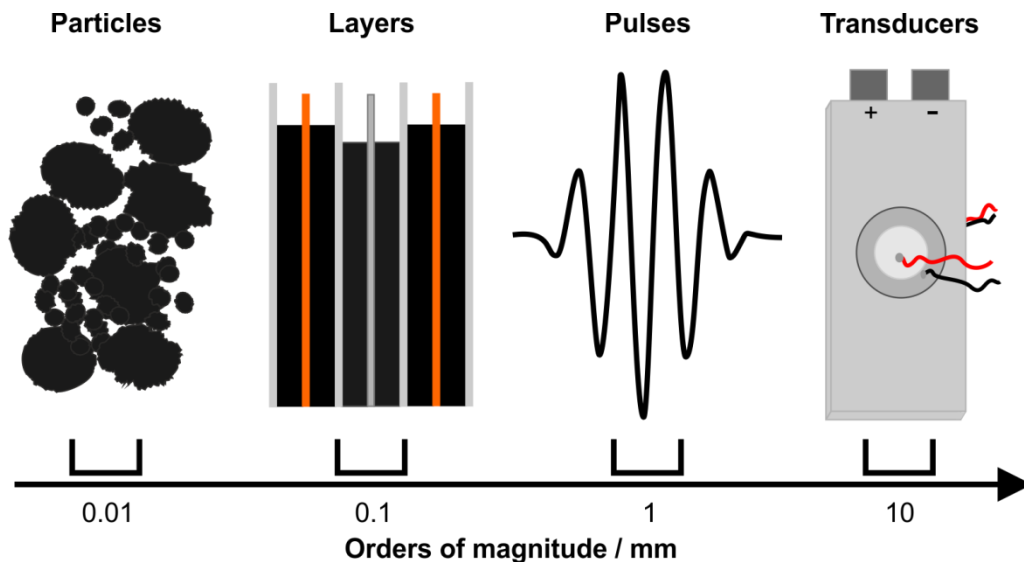
Figure 8.4 Relevante Längenskalen in Ultraschallexperimenten an Pouchzellen. Das beobachtete Transmissionsverhalten kann durch Effekte auf verschiedenen Längenskalen erklärt werden. Die Mikroporosität der Elektroden führt zum Auftreten langsamer Akustischer Moden und die Schichtstruktur führt zu Dämpfungseffekten, wenn die Wellenlänge des Schalls sich ihrer Längenskala annähert. Schlussendlich werden ausreichend große Schallwandler benötigt um ein homogenes Schallfeld zu erzeugen.

Da die Methode nicht auf elektrischen Messungen an der Zelle beruht, ist sie bezüglich der elektrischen Topologie in Batteriepacks unempfindlich. Mit klassischen Methoden ist eine Einzelzellenüberwachung des Ladezustands bisher sehr aufwändig und in manchen Topologien weitgehend unmöglich. Im Gegensatz hierzu können kostengünstige Piezosummer von den Zellen galvanisch getrennt betrieben werden und so eine von der elektrischen Topologie unabhängige Ladezustandserkennung auf Zellebene ermöglichen. Da die Messzeiten sehr kurz sind, können die Zellen mittels Multiplexing sequentiell von einer einzigen Messlogik vermessen werden. Somit kann mittels Ultraschall eine kostengünstige Einzelzellenüberwachung des Ladezustands kommerzieller Zellen unabhängig von deren elektrischer Kontaktierung implementiert werden.

Da der Einsatz von Ultraschallpulsen vielversprechend erscheint, sollten in weiteren Studien Faktoren wie Langzeitverhalten, Temperatur- und Rateneinflüsse untersucht werden. In dieser Arbeit wurde weiterhin Hysterese beobachtet deren tieferes Verständnis nicht nur die Ladezustandsbestimmung, sondern auch das Verständnis der dynamischen Prozesse in Lithium-Ionen Zellen verbessern könnte.

9 References

[1] a) C. J. Rydh, B. A. Sandén, *Energ. Convers. Manage.* **2005**, *46*, 1980; b) J. Jaguemont, L. Boulon, Y. Dubé, *Appl. Energy* **2016**, *164*, 99.

[2] B. Scrosati, J. Garche, *J. Power Sources* **2010**, *195*, 2419.

[3] J. Vetter, P. Novák, M. Wagner, C. Veit, K.-C. Möller, J. Besenhard, M. Winter, M. Wohlfahrt-Mehrens, C. Vogler, A. Hammouche, *J. Power Sources* **2005**, *147*, 269.

[4] T. Waldmann, S. Gorse, T. Samtleben, G. Schneider, V. Knoblauch, M. Wohlfahrt-Mehrens, *J. Electrochem. Soc.* **2014**, *161*, 1742.

[5] J. Cannarella, C. B. Arnold, *J. Power Sources* **2014**, *269*, 7.

[6] L. W. Sommer, P. Kiesel, A. Ganguli, A. Lochbaum, B. Saha, J. Schwartz, C.-J. Bae, M. Alamgir, A. Raghavan, *J. Power Sources* **2015**, *296*, 46.

[7] A. G. Hsieh, S. Bhadra, B. J. Hertzberg, P. J. Gjeltema, A. Goy, J. W. Fleischer, D. A. Steingart, *Energy Environ. Sci.* **2015**, *8*, 1569.

[8] M. Ecker, N. Nieto, S. Käbitz, J. Schmalstieg, H. Blanke, A. Warnecke, D. U. Sauer, *J. Power Sources* **2014**, *248*, 839.

[9] M. Broussely, P. Biensan, F. Bonhomme, P. Blanchard, S. Herreyre, K. Nechev, R. Staniewicz, *J. Power Sources* **2005**, *146*, 90.

[10] E. Sarasketa-Zabala, F. Aguesse, I. Villarreal, L. M. Rodriguez-Martinez, C. M. López, P. Kubiak, *J. Phys. Chem. C* **2015**, *119*, 896.

[11] M. J. Brand, S. F. Schuster, T. C. Bach, E. Fleder, M. Stelz, S. Gläser, J. Müller, G. Sextl, A. Jossen, *J. Power Sources* **2015**, *288*, 62.

[12] A. Yoshino, *Angew. Chem., Int. Ed.* **2012**, *51*, 5798.

[13] C. H. Hamann, W. Vielstich, *Elektrochemie*, Wiley-VCH, Weinheim, **2005**.

[14] E. Riedel, R. Alsfasser, *Moderne anorganische Chemie. Mit CD-ROM*, de Gruyter, Berlin [u.a.], **2012**.

[15] J.-i. Yamaki, S.-i. Tobishima, K. Hayashi, Keiichi Saito, Y. Nemoto, M. Arakawa, *J. Power Sources* **1998**, *74*, 219.

[16] D. Aurbach, E. Zinigrad, H. Teller, P. Dan, *J. Electrochem. Soc.* **2000**, *147*, 1274.

[17] Z. Li, J. Huang, B. Yann Liaw, V. Metzler, J. Zhang, *J. Power Sources* **2014**, *254*, 168.

[18] D. Aurbach, E. Zinigrad, H. Teller, Y. Cohen, G. Salitra, H. Yamin, P. Dan, E. Elster, *J. Electrochem. Soc.* **2002**, *149*, 1267.

[19] R. Yazami, P. Touzain, *J. Power Sources* **1983**, *9*, 365.

[20] a) D. Guerard, A. Herold, *Carbon* **1975**, *13*, 337; b) W. Rüdorff, *Angew. Chem* **1959**, *71*, 487.

[21] C. Daniel, J. O. Besenhard, *Handbook of Battery Materials*, Wiley, Weinheim, **2012**.

[22] K. Mizushima, P. C. Jones, P. J. Wiseman, J. B. Goodenough, *MRS Bulletin* **1980**, *15*, 783.

[23] J. M. Tarascon, D. Guyomard, *Solid State Ionics* **1994**, *69*, 293.

[24] J. M. Tarascon, M. Armand, *Nature* **2001**, *414*, 359.

[25] D. Aurbach, B. Markovsky, Y. Ein-Eli in *New Promising Electrochemical Systems for Rechargeable Batteries* (Eds.: V. Barsukov, F. Beck), Springer Netherlands, Dordrecht, **1996**, pp. 63–75.

[26]N. Nitta, F. Wu, J. T. Lee, G. Yushin, *Materials Today* **2015**, *18*, 252.

[27]M. M. Thackeray, C. Wolverton, E. D. Isaacs, *Energy Environ. Sci.* **2012**, *5*, 7854.

[28]B. Zhao, R. Ran, M. Liu, Z. Shao, *Materials Science and Engineering: R: Reports* **2015**, *98*, 1.

[29]H. Huang, W. Liu, X. Huang, L. Chen, E. M. Kelder, J. Schoonman, *Solid State Ionics* **1998**, *110*, 173.

[30]P. Ridgway, H. Zheng, A. F. Bello, X. Song, S. Xun, J. Chong, V. Battaglia, *J. Electrochem. Soc.* **2012**, *159*, 520.

[31]G.-N. Zhu, Y.-G. Wang, Y.-Y. Xia, *Energy Environ. Sci.* **2012**, *5*, 6652.

[32]H.-P. Boehm, U. Hofmann, *Z. Anorg. Allg. Chem.* **1955**, *278*, 58.

[33]H. Shi, J. Barker, M. Y. Saïdi, R. Koksbang, L. Morris, *J. Power Sources* **1997**, *68*, 291.

[34]D. E. Sands, *Introduction to crystallography*, Dover Publ, New York NY, **1993**.

[35]a) K. Zaghib, F. Brochu, A. Guerfi, K. Kinoshita, *Journal of Power Sources* **2001**, *103*, 140; b) A. Funabiki, *J. Electrochem. Soc.* **1998**, *145*, 172.

[36]A. Senyshyn, O. Dolotko, M. J. Muhlbauer, K. Nikolowski, H. Fuess, H. Ehrenberg, *J. Electrochem. Soc.* **2013**, *160*, 3198.

[37]M. Winter, J. O. Besenhard, M. E. Spahr, P. Novák, *Adv. Mater.* **1998**, *10*, 725.

[38]a) W. Rüdorff, U. Hofmann, *Z. Anorg. Allg. Chem.* **1938**, *238*, 1; b) H. P. Boehm, R. Setton, E. Stumpp, *Pure and Applied Chemistry* **1994**, *66*.

[39]a) D. Billaud, F. X. Henry, M. Lelaurain, P. Willmann, *J. Phys. Chem. Solids* **1996**, *57*, 775; b) Y. Qi, L. G. Hector, C. James, K. J. Kim, *J. Electrochem. Soc.* **2014**, *161*, 3010; c) T. Ohzuku, N. Matoba, K. Sawai, *J. Power Sources* **2001**, *97-98*, 73.

[40]B. Bitzer, A. Gruhle, *J. Power Sources* **2014**, *262*, 297.

[41]J. Cannarella, C. B. Arnold, *J. Power Sources* **2014**, *245*, 745.

[42]Y. Qi, S. J. Harris, *J. Electrochem. Soc.* **2010**, *157*, 741.

[43]S. J. Harris, P. Lu, *J. Phys. Chem. C* **2013**, *117*, 6481.

[44]J. W. Fergus, *J. Power Sources* **2010**, *195*, 939.

[45]a) J. Akimoto, Y. Gotoh, Y. Oosawa, *J. Solid State Chem.* **1998**, *141*, 298; b) E. Antolini, *Solid State Ionics* **2004**, *170*, 159.

[46]a) R. Gupta, A. Manthiram, *J. Solid State Chem.* **1996**, *121*, 483; b) G. G. Amatucci, *J. Electrochem. Soc.* **1996**, *143*, 1114.

[47]a) C.-Y. Jhu, Y.-W. Wang, C.-Y. Wen, C.-M. Shu, *Appl. Energy* **2012**, *100*, 127; b) Y. Furushima, C. Yanagisawa, T. Nakagawa, Y. Aoki, N. Muraki, *J. Power Sources* **2011**, *196*, 2260.

[48]A. Kraytsberg, Y. Ein-Eli, *Adv. Energy Mater.* **2012**, *2*, 922.

[49]a) T. Ohzuku, Y. Makimura, *Chem. Lett.* **2001**, 642; b) T. Ohzuku, Y. Makimura, *Chem. Lett.* **2001**, 744.

[50]S.-H. Park, S.-H. Kang, I. Belharouak, Y. K. Sun, K. Amine, *J. Power Sources* **2008**, *177*, 177.

[51]A. Ito, D. Li, Y. Sato, M. Arao, M. Watanabe, M. Hatano, H. Horie, Y. Ohsawa, *J. Power Sources* **2010**, *195*, 567.

[52] C. Wang, F. Zhou, C. Ren, Y. Wang, J. Kong, Y. Jiang, G. Yan, J. Li, *Solid State Ionics* **2015**, *281*, 96.

[53] G. Che, *J. Electrochem. Soc.* **1997**, *144*, 4296.

[54] J. Cho, Y.-W. Kim, B. Kim, J.-G. Lee, B. Park, *Angewandte Chemie (International ed. in English)* **2003**, *42*, 1618.

[55] T. Ohzuku, *J. Electrochem. Soc.* **1993**, *140*, 1862.

[56] P. G. Bruce, A. R. Armstrong, R. L. Gitzendanner, *J. Mater. Chem.* **1999**, *9*, 193.

[57] F. Lin, I. M. Markus, D. Nordlund, T.-C. Weng, M. D. Asta, H. L. Xin, M. M. Doeff, *Nat. Commun.* **2014**, *5:3529*, 1.

[58] C. Wang, F. Zhou, C. Ren, J. Kong, Z. Tang, J. Li, C. Yu, W.-P. Tang, *J. Alloys Compd.* **2015**, *643*, 223.

[59] S. K. Martha, O. Haik, E. Zinigrad, I. Exnar, T. Drezen, J. H. Miners, D. Aurbach, *J. Electrochem. Soc.* **2011**, *158*, 1115.

[60] R. Wang, X. He, L. He, F. Wang, R. Xiao, L. Gu, H. Li, L. Chen, *Adv. Energy Mater.* **2013**, *3*, 1358.

[61] M.-J. Lee, S. Lee, P. Oh, Y. Kim, J. Cho, *Nano Lett.* **2014**, *14*, 993.

[62] S. Choi, A. Manthiram, *J. Electrochem. Soc.* **2002**, *149*, 162.

[63] a) J. Hassoun, P. Reale, B. Scrosati, *J. Mater. Chem.* **2007**, *17*, 3668; b) S. Patoux, L. Sannier, H. Lignier, Y. Reynier, C. Bourbon, S. Jouanneau, F. Le Cras, S. Martinet, *Electrochim. Acta* **2008**, *53*, 4137.

[64] A. Yamada, S. C. Chung, K. Hinokuma, *J. Electrochem. Soc.* **2001**, *148*, 224.

[65] D. Choi, D. Wang, I.-T. Bae, J. Xiao, Z. Nie, W. Wang, V. V. Viswanathan, Y. J. Lee, J.-G. Zhang, G. L. Graff et al., *Nano Lett.* **2010**, *10*, 2799.

[66] J. M. Lloris, C. Pérez Vicente, J. L. Tirado, *Electrochem. Solid-State Lett.* **2002**, *5*, 234.

[67] A. Sobkowiak, M. R. Roberts, R. Younesi, T. Ericsson, L. Häggström, C.-W. Tai, A. M. Andersson, K. Edström, T. Gustafsson, F. Björefors, *Chem. Mater.* **2013**, *25*, 3020.

[68] J. Barker, R. Gover, P. Burns, A. Bryan, M. Y. Saidi, J. L. Swoyer, *J. Power Sources* **2005**, *146*, 516.

[69] T. R. Jow, K. Xu, O. Borodin, M. Ue, *Electrolytes for Lithium and Lithium-Ion Batteries*, Springer New York, New York, NY, s.l., **2014**.

[70] K. Xu, *Chem. Rev.* **2014**, *114*, 11503.

[71] M. Smart, B. Ratnakumar, *NASA Tech Briefs* **2008**, *32*.

[72] J. B. Goodenough, Y. Kim, *Chem. Mater.* **2010**, *22*, 587.

[73] G. Sarre, P. Blanchard, M. Broussely, *Journal of Power Sources* **2004**, *127*, 65.

[74] A. Würsig, H. Buqa, M. Holzapfel, F. Krumeich, P. Novák, *Electrochem. Solid-State Lett.* **2005**, *8*, A34.

[75] a) W. Xu, X. Chen, F. Ding, J. Xiao, D. Wang, A. Pan, J. Zheng, X. S. Li, A. B. Padmaperuma, J.-G. Zhang, *J. Power Sources* **2012**, *213*, 304; b) D. Aurbach, Y. Talyosef, B. Markovsky, E. Markevich, E. Zinigrad, L. Asraf, J. S. Gnanaraj, H.-J. Kim, *Electrochim. Acta* **2004**, *50*, 247.

[76] D. Y. Wang, N. Sinha, R. Petibon, J. Burns, J. R. Dahn, *J. Power Sources* **2014**, *251*, 311.

[77] a) D. Ensling, *Lithium-Ionen-Zellen mit verbesserten Eigenschaften*, **2013**, Google Patents, can be found under https://www.google.st/patents/DE102011084009A1?cl=de; b) T. Jow, S. Zhang, K. Xu, M. Ding, *Non-aqueous electrolyte solutions comprising additives and non-aqueous electrolyte cells comprising the same*, **2005**, Google Patents, can be found under http://www.google.com.tr/patents/US6905762; c) K. Abe, M. Colera, *Functional Electrolytes*. Presented at International Battery Association meeting 2013, **2013**.

[78] Trung H. Nguyen, Peter Marren, Kevin Gering, *Improving the Performance of Lithium Ion Batteries at Low Temperature*. *Grant No: DE-FG02-06ER84531, Topic: 19-A*. Final Technical Report, **2007**.

[79] S. S. Zhang, *J. Power Sources* **2006**, *162*, 1379.

[80] M. C. Smart, B. V. Ratnakumar, S. Surampudi, *J. Electrochem. Soc.* **2002**, *149*, A361.

[81] a) X. Feng, J. Sun, M. Ouyang, X. He, L. Lu, X. Han, M. Fang, H. Peng, *J. Power Sources* **2014**, *272*, 457; b) X. Han, M. Ouyang, L. Lu, J. Li, Y. Zheng, Z. Li, *J. Power Sources* **2013**; c) Y. Li, M. Bettge, B. Polzin, Y. Zhu, M. Balasubramanian, D. P. Abraham, *J. Electrochem. Soc.* **2013**, *160*, 3006.

[82] B. Stiaszny, J. C. Ziegler, E. E. Krauß, J. P. Schmidt, E. Ivers-Tiffée, *J. Power Sources* **2014**, *251*, 439.

[83] B. Stiaszny, J. C. Ziegler, E. E. Krauß, M. Zhang, J. P. Schmidt, E. Ivers-Tiffée, *J. Power Sources* **2014**, *258*, 61.

[84] M. Broussely, S. Herreyre, P. Biensan, P. Kasztejna, K. Nechev, R. Staniewicz, *J. Power Sources* **2001**, *97-98*, 13.

[85] A. Barré, B. Deguilhem, S. Grolleau, M. Gérard, F. Suard, D. Riu, *J. Power Sources* **2013**, *241*, 680.

[86] V. Agubra, J. Fergus, *Materials* **2013**, *6*, 1310.

[87] S. F. Schuster, T. C. Bach, E. Fleder, J. Müller, M. Brand, G. Sextl, A. Jossen, *J. Energy Storage* **2015**, *1*, 44.

[88] S. J. An, J. Li, C. Daniel, D. Mohanty, S. Nagpure, D. L. Wood, *Carbon* **2016**, *105*, 52.

[89] a) J. B. Goodenough, K. S. Park, *Journal of the American Chemical Society* **2013**, *135*, 1167; b) K. Xu, *Chem. Rev.* **2004**, *104*, 4303.

[90] E. Peled, *J. Electrochem. Soc.* **1979**, *126*, 2047.

[91] I. A. Shkrob, Y. Zhu, T. W. Marin, D. Abraham, *J. Phys. Chem. C* **2013**.

[92] I. A. Shkrob, Y. Zhu, T. W. Marin, D. Abraham, *J. Phys. Chem. C* **2013**, *117*, 19270.

[93] E. Peled, D. Golodnitsky, A. Ulus, V. Yufit, *Electrochim. Acta* **2004**, *50*, 391.

[94] D. Aurbach, *Solid State Ionics* **2002**, *148*, 405.

[95] M. Grützke, V. Kraft, B. Hoffmann, S. Klamor, J. Diekmann, A. Kwade, M. Winter, S. Nowak, *J. Power Sources* **2015**, *273*, 83.

[96] a) G. Gachot, S. Grugeon, M. Armand, S. Pilard, P. Guenot, J. M. Tarascon, S. Laruelle, *J. Power Sources* **2008**, *178*, 409; b) P. Handel, G. Fauler, K. Kapper, M. Schmuck, C. Stangl, R. Fischer, F. Uhlig, S. Koller, *J. Power*

Sources **2014**, *267*, 255; c) V. Kraft, W. Weber, M. Grützke, M. Winter, S. Nowak, *RSC Adv.* **2015**, *5*, 80150; d) V. Kraft, M. Grützke, W. Weber, M. Winter, S. Nowak, *J. Chromatogr. A* **2014**, *1354*, 92.

[97] L. Yang, B. Ravdel, B. L. Lucht, *Electrochem. Solid-State Lett.* **2010**, *13*, A95-A97.

[98] K. Tasaki, K. Kanda, T. Kobayashi, S. Nakamura, M. Ue, *J. Electrochem. Soc.* **2006**, *153*, A2192.

[99] X. Zhang, R. Kostecki, T. J. Richardson, J. K. Pugh, P. N. Ross, *J. Electrochem. Soc.* **2001**, *148*, A1341.

[100] K. Schroder, J. Alvarado, T. A. Yersak, J. Li, N. Dudney, L. J. Webb, Y. S. Meng, K. J. Stevenson, *Chem. Mater.* **2015**, *27*, 5531.

[101] W. Märkle, C.-Y. Lu, P. Novák, *J. Electrochem. Soc.* **2011**, *158*, A1478.

[102] P. Verma, P. Maire, P. Novák, *Electrochim. Acta* **2010**, *55*, 6332.

[103] D. L. Wood, J. Li, C. Daniel, *Journal of Power Sources* **2015**, *275*, 234.

[104] A. M. Andersson, K. Edström, *J. Electrochem. Soc.* **2001**, *148*, A1100.

[105] T. Zheng, *J. Electrochem. Soc.* **1999**, *146*, 4014.

[106] a) E. P. Roth in *Proceedings volume / Electrochemical Society*, *2000-21* (Ed.: M. Doyle), Electrochemical Society, Pennington, NJ, **2001**, pp. 401–413; b) M. N. Richard, *J. Electrochem. Soc.* **1999**, *146*, 2068.

[107] K. Edström, T. Gustafsson, J. O. Thomas, *Electrochimica Acta* **2004**, *50*, 397.

[108] S. Malmgren, K. Ciosek, M. Hahlin, T. Gustafsson, M. Gorgoi, H. Rensmo, K. Edström, *Electrochimica Acta* **2013**, *97*, 23.

[109] I. Buchberger, S. Seidlmayer, A. Pokharel, M. Piana, J. Hattendorff, P. Kudejova, R. Gilles, H. A. Gasteiger, *J. Electrochem. Soc.* **2015**, *162*, A2737-A2746.

[110] J. Choi, A. Manthiram, *J. Electrochem. Soc.* **2005**, *152*, 1714.

[111] a) D. J. Xiong, R. Petibon, M. Nie, L. Ma, J. Xia, J. R. Dahn, *J. Electrochem. Soc.* **2016**, *163*, A546-A551; b) D. W. Abarbanel, K. J. Nelson, J. R. Dahn, *J. Electrochem. Soc.* **2015**, *163*, A522-A529.

[112] I. A. Shkrob, A. J. Kropf, T. W. Marin, Y. Li, O. G. Poluektov, J. Niklas, D. P. Abraham, *J. Phys. Chem. C* **2014**, *118*, 24335.

[113] S. Komaba, N. Kumagai, Y. Kataoka, *Electrochim. Acta* **2002**, *47*, 1229.

[114] H. Zheng, Q. Sun, G. Liu, X. Song, V. S. Battaglia, *J. Power Sources* **2012**, *207*, 134.

[115] a) T. Ohzuku, *J. Electrochem. Soc.* **1993**, *140*, 2490; b) W. H. Woodford, W. C. Carter, Y. M. Chiang, *Energy and Environmental Science* **2012**, *5*, 8014; c) W.-S. Yoon, K. Y. Chung, J. McBreen, X.-Q. Yang, *Electrochemistry Communications* **2006**, *8*, 1257.

[116] R. Kostecki, F. McLarnon, *J. Power Sources* **2003**, *119-121*, 550.

[117] V. A. Sethuraman, L. J. Hardwick, V. Srinivasan, R. Kostecki, *J. Power Sources* **2010**, *195*, 3655.

[118] L. J. Hardwick, M. Marcinek, L. Beer, J. B. Kerr, R. Kostecki, *J. Electrochem. Soc.* **2008**, *155*, 442.

[119] a) N. Yuca, H. Zhao, X. Song, M. F. Dogdu, W. Yuan, Y. Fu, V. S. Battaglia, X. Xiao, G. Liu, *ACS Appl. Mater. Interfaces* **2014**, *6*, 17111; b)

R. S. Rubino, H. Gan, E. S. Takeuchi, *J. Electrochem. Soc.* **2001**, *148*, A1029.

[120] K. Takahashi, V. Srinivasan, *J. Electrochem. Soc.* **2015**, *162*, 635.

[121] F. Sagane, R. Shimokawa, H. Sano, H. Sakaebe, Y. Iriyama, *J. Power Sources* **2013**, *225*, 245.

[122] M. Petzl, M. A. Danzer, *J. Power Sources* **2014**, *254*, 80.

[123] K. Jalkanen, J. Karppinen, L. Skogström, T. Laurila, M. Nisula, K. Vuorilehto, *Appl. Energy* **2015**, *154*, 160.

[124] a) M. Dubarry, C. Truchot, B. Y. Liaw, K. Gering, S. Sazhin, D. Jamison, C. Michelbacher, *J. Electrochem. Soc.* **2012**, *160*, 191; b) M. Zier, F. Scheiba, S. Oswald, J. Thomas, D. Goers, T. Scherer, M. Klose, H. Ehrenberg, J. Eckert, *J. Power Sources* **2014**, *266*, 198.

[125] J. Cannarella, C. B. Arnold, *J. Electrochem. Soc.* **2015**, *162*, A1365-A1373.

[126] D. Martin, A. Hiebl, L. Krueger, *Mat.-wiss. u. Werkstofftech.* **2011**, *42*, 958.

[127] J. M. Hooper, J. Marco, *J. Power Sources* **2014**, *245*, 510.

[128] C. Mikolajczak, M. Kahn, K. White, R. T. Long, *Lithium ion batteries hazard and use assessment*, **2011**.

[129] *Recommendations on the transport of dangerous goods. Manual of tests and criteria*, United Nations, New York, Geneva, **2009**.

[130] International Electrotechnical Commission, *Secondary lithium-ion cells for the propulsion of electric road vehicles - Part 2: Reliability and abuse testing*, *29.220.20 43.120*.

[131] *ECE R100 Uniform provisions concerning the approval of vehicles with regard to specific requirements for the electric power train*, Geneva, **2013**.

[132] SAE International, *Vibration Testing of Electric Vehicle Batteries*, **2013**.

[133] British Standards Institution, *Secondary lithium-ion cells for the propulsion of electric road vehicles. Performance testing*, *29.220.20*, **2011,** can be found under http://shop.bsigroup.com/ProductDetail/?pid=000000000030214275.

[134] J. Hooper, J. Marco, G. Chouchelamane, C. Lyness, *Energies* **2016**, *9*, 52.

[135] a) H. J. Ploehn, P. Ramadass, R. E. White, *J. Electrochem. Soc.* **2004**, *151*, 456; b) M. Ecker, J. B. Gerschler, J. Vogel, S. Käbitz, F. Hust, P. Dechent, D. U. Sauer, *J. Power Sources* **2012**, *215*, 248.

[136] a) J. Wang, J. Purewal, P. Liu, J. Hicks-Garner, S. Soukazian, E. Sherman, A. Sorenson, L. Vu, H. Tataria, M. W. Verbrugge, *J. Power Sources* **2014**, *269*, 937; b) J. Schmalstieg, S. Käbitz, M. Ecker, D. U. Sauer, *J. Power Sources* **2014**, *257*, 325.

[137] L. Su, J. Zhang, C. Wang, Y. Zhang, Z. Li, Y. Song, T. Jin, Z. Ma, *Appl. Energy* **2016**, *163*, 201.

[138] J. C. Burns, A. Kassam, N. N. Sinha, L. E. Downie, L. Solnickova, B. M. Way, J. R. Dahn, *J. Electrochem. Soc.* **2013**, *160*, 1451.

[139] M. Petzl, M. Kasper, M. A. Danzer, *J. Power Sources* **2015**, *275*, 799.

[140] K. J. Langenberg, R. Marklein, K. Mayer, *Ultrasonic Nondestructive Testing of Materials: Theoretical Foundations*, CRC Press, **2012**.

[141]   K. Gentile, *RF DESIGN* **2002**, *25*, 50.

[142]   M. A. Biot, *J. Acoust. Soc. Am.* **1956**, *28*, 168.

[143]   M. A. Biot, *J. Acoust. Soc. Am.* **1956**, *28*, 179.

[144]   K. N. van Dalen (Ed.) *Springer Theses*, Springer Berlin Heidelberg, Berlin, Heidelberg, **2013**.

[145]   M. Weller, T. Overton, J. Rourke, F. A. Armstrong, *Inorganic chemistry*.

[146]   J. Jocker, D. Smeulders, *Ultrasonics* **2009**, *49*, 319.

[147]   a) T. E. Gómez Alvarez-Arenas, Riera-Franco de Sarabia, E., Montero de Espinosa-Feijo, F.R., *Ultrasonics* **1994**, *32*, 131; b) T. E. Gómez-Alvarez Arenas, E. Riera Franco De Sarabia, *J. Phys. IV France* **1994**, *04*, 187; c) K. I. Lee, S. W. Yoon, *J. Biomech.* **2006**, *39*, 364; d) Z. A. Fellah, N. Sebaa, M. Fellah, F. G. Mitri, E. Ogam, W. Lauriks, C. Depollier, *IEEE transactions on ultrasonics, ferroelectrics, and frequency control* **2008**, *55*, 1508; e) M. Pakula, F. Padilla, P. Laugier, M. Kaczmarek, *J. Acoust. Soc. Am.* **2008**, *123*, 2415; f) C. M. Langton, C. F. Njeh, *IEEE transactions on ultrasonics, ferroelectrics, and frequency control* **2008**, *55*, 1546; g) T. J. Plona, *Appl. Phys. Lett.* **1980**, *36*, 259.

[148]   a) S. R. Pride, E. Tromeur, J. G. Berryman, *Geophysics* **2002**, *67*, 271; b) L. A. Molotkov, A. V. Bakulin, *J Math Sci* **1999**, *96*, 3371.

[149]   J. O. Parra, *J. Acoust. Soc. Am.* **1994**, *95*, 91.

[150]   J. G. Berryman, *PAGEOPH* **1988**, *128*, 423.

[151]   a) W. F. Murphy, K. W. Winkler, R. L. Kleinberg, *Geophysics* **1986**, *51*, 757; b) J. Dvorkin, R. Nolen-Hoeksema, A. Nur, *Geophysics* **1994**, *59*, 428; c) B. Gurevich, D. Makarynska, de Paula, Osni Bastos, M. Pervukhina, *Geophysics* **2010**, *75*, N109-N120.

[152]   A. N. Norris, *J. Acoust. Soc. Am.* **1993**, *94*, 359.

[153]   a) T. M. Müller, B. Gurevich, M. Lebedev, *Geophysics* **2010**, *75*, 75; b) S. Gelinsky, S. A. Shapiro, T. Müller, B. Gurevich, *Int. J. Solid Struct.* **1998**, *35*, 4739.

[154]   J. B. Walsh, *J. Geophys. Res.* **1969**, *74*, 4333.

[155]   J. M. Carcione, D. Kosloff, A. Behle, *Geophysics* **1991**, *56*, 245.

[156]   a) H. Ren, G. Goloshubin, F. J. Hilterman, *Geophysics* **2009**, *74*, N49-N54; b) J. E. White, *J. Acoust. Soc. Am.* **1975**, *57*, 654.

[157]   B. B. S. A. Vogelaar, *Dissertation*, Technische Universiteit Delft, Delft, **2009**.

[158]   a) X. Feng, J. Li, M. Ouyang, L. Lu, J. Li, X. He, *J. Power Sources* **2013**, *232*, 209; b) J. P. Christophersen, S. R. Shaw, *J. Power Sources* **2010**, *195*, 1225.

[159]   a) F. J. Padden, H. D. Keith, *J. Appl. Phys.* **1959**, *30*, 1479; b) L. C. Sawyer, D. T. Grubb, G. F. Meyers, *Polymer microscopy*, Springer, New York, ©**2008**.

[160]   D. A. Stevens, R. Y. Ying, R. Fathi, J. N. Reimers, J. E. Harlow, J. R. Dahn, *J. Electrochem. Soc.* **2014**, *161*, A1364-A1370.

[161]   F. Rosciano, J.-F. Colin, F. La Mantia, N. Tran, P. Novák, *Electrochem. Solid-State Lett.* **2009**, *12*, 140.

[162]   N. Yabuuchi, Y. Makimura, T. Ohzuku, *J. Electrochem. Soc.* **2007**, *154*, 314.

[163]   Y. Idemoto, T. Matsui, *Electrochemistry* **2007**, *75*, 791.

[164]   a) O. Dolotko, A. Senyshyn, M. J. Mühlbauer, K. Nikolowski, H. Ehrenberg, *J. Power Sources* **2014**, *255*, 197; b) X.-L. Wang, K. An, L. Cai, Z. Feng, S. E. Nagler, C. Daniel, K. J. Rhodes, A. D. Stoica, H. D. Skorpenske, C. Liang et al., *Sci. Rep.* **2012**, *2*, 747.

[165]   S.-C. Yin, Y.-H. Rho, I. Swainson, L. F. Nazar, *Chem. Mater.* **2006**, *18*, 1901.

[166]   N.-S. Choi, Z. Chen, S. A. Freunberger, X. Ji, Y.-K. Sun, K. Amine, G. Yushin, L. F. Nazar, J. Cho, P. G. Bruce, *Angew. Chem., Int. Ed.* **2012**, *51*, 9994.

[167]   M. Wohlfahrt-Mehrens, C. Vogler, J. Garche, *J. Power Sources* **2004**, *127*, 58.

[168]   M. Dollé, L. Sannier, B. Beaudoin, M. Trentin, J. M. Tarascon, *Electrochem. Solid-State Lett.* **2002**, *5*, 286.

[169]   M. Fleischhammer, T. Waldmann, G. Bisle, B.-I. Hogg, M. Wohlfahrt-Mehrens, *J. Power Sources* **2015**, *274*, 432.

[170]   a) M. Dubarry, C. Truchot, B. Y. Liaw, *J. Power Sources* **2012**, *219*, 204; b) A. Barré, F. Suard, M. Gérard, M. Montaru, D. Riu, *J. Power Sources* **2014**, *245*, 846; c) M. Ouyang, Z. Chu, L. Lu, J. Li, X. Han, X. Feng, G. Liu, *J. Power Sources* **2015**, *286*, 309.

[171]   a) M. Dubarry, C. Truchot, B. Y. Liaw, K. Gering, S. Sazhin, D. Jamison, C. Michelbacher, *J. Power Sources* **2011**, *196*, 10336; b) M. Dubarry, C. Truchot, M. Cugnet, B. Y. Liaw, K. Gering, S. Sazhin, D. Jamison, C. Michelbacher, *J. Power Sources* **2011**, *196*, 10328.

[172]   K. B. Oldham, *J. Electroanal. Chem. Interfacial Electrochem.* **1981**, *122*, 1.

[173]   a) M. Klett, R. Eriksson, J. Groot, P. Svens, K. Ciosek Högström, R. W. Lindström, H. Berg, T. Gustafson, G. Lindbergh, K. Edström, *J. Power Sources* **2014**, *257*, 126; b) N. Zhang, H. Tang, *J. Power Sources* **2012**, *218*, 52; c) W. Zhao, G. Luo, C.-Y. Wang, *J. Power Sources* **2014**, *257*, 70; d) L. Cai, K. An, Z. Feng, C. Liang, S. J. Harris, *J. Power Sources* **2013**, *236*, 163.

[174]   T. Waldmann, M. Wohlfahrt-Mehrens, *ECS Electrochem. Lett.* **2014**, *4*, A1-A3.

[175]   J. Cannarella, C. B. Arnold, *J. Power Sources* **2013**, *226*, 149.

[176]   A. Barai, Y. Guo, A. McGordon, P. Jennings (Eds.) *A study of the effects of external pressure on the electrical performance of a lithium-ion pouch cell*, IEEE, **2013**.

[177]   K. B. Oldham, *J. Solid State Electrochem.* **1997**, *1*, 36.

[178]   a) R. Chandrasekaran, *J. Power Sources* **2014**, *262*, 501; b) B. K. Purushothaman, U. Landau, *J. Electrochem. Soc.* **2006**, *153*, 533.

[179]   L. Lu, X. Han, J. Li, J. Hua, M. Ouyang, *J. Power Sources* **2013**, *226*, 272.

[180]   H. Maleki, J. N. Howard, *J. Power Sources* **2009**, *191*, 568.

[181]   S.-i. Tobishima, J.-i. Yamaki, *J. Power Sources* **1999**, *81-82*, 882.

[182]   *Road vehicles -- Environmental conditions and testing for electrical and electronic equipment -- Part 3: Mechanical loads*, *43.040.10*, **2012,** can be found under http://www.iso.org/iso/catalogue_detail.htm?csnumber=58049.

[183]   P. Svens, M. Kjell, C. Tengstedt, G. Flodberg, G. Lindbergh, *Energies* **2013**, *6*, 400.

[184]   a) J. Lamb, C. J. Orendorff, *J. Power Sources* **2014**, *247*, 189; b) E. Sahraei, J. Meier, T. Wierzbicki, *J. Power Sources* **2014**, *247*, 503; c) L. Greve, C. Fehrenbach, *J. Power Sources* **2012**, *214*, 377; d) I. Avdeev, M. Gilaki, *J. Power Sources* **2014**, *271*, 382; e) H. Budde-Meiwes, J. Drillkens, B. Lunz, J. Muennix, S. Rothgang, J. Kowal, D. U. Sauer, *Proc. Inst. Mech. Eng., Part D* **2013**, *227*, 761.

[185]   J. M. Hooper, J. Marco, *J. Power Sources* **2015**, *285*, 247.

[186]   R. El Abdi, N. Benjemaa, *Proc. Inst. Mech. Eng., Part D* **2015**, *229*, 189.

[187]   M. Berecibar, I. Gandiaga, I. Villarreal, N. Omar, J. van Mierlo, Van den Bossche, P., *Renewable Sustainable Energy Rev.* **2016**, *56*, 572.

[188]   a) V. Sethuraman, N. van Winkle, D. P. Abraham, A. Bower, P. Guduru, *J. Power Sources* **2012**, *206*, 334; b) L. Gold, *Master's thesis*, Julius-Maximilians Universität Würzburg, Würzburg, **2015**.

[189]   a) C. Zhang, J. Jiang, W. Zhang, S. M. Sharkh, *Energies* **2012**, *5*, 1098; b) M. A. Roscher, O. Bohlen, J. Vetter, *Int. J. Electrochem.* **2011**, *2011*, 1; c) W. Dreyer, J. Jamnik, C. Guhlke, R. Huth, J. Moskon, M. Gaberscek, *Nat Mater* **2010**, *9*, 448.

[190]   H. C. Howard, G. A. Hulett, *J. Phys. Chem.* **1923**, *28*, 1082.

[191]   "Product Specification. Lithium hexafluorophosphate solution in ethylene carbonate and ethyl methyl carbonate, 1.0 M LiPF6 in EC/EMC=50/50 (v/v), battery grade Specification Sheet".

[192]   M. Ebner, D.-W. Chung, R. E. García, V. Wood, *Adv. Energy Mater.* **2014**, *4*, n/a.

[193]   G. Y. Gor, J. Cannarella, J. H. Prevost, C. B. Arnold, *J. Electrochem. Soc.* **2014**, *161*, 3065.

[194]   Y. Qi, H. Guo, L. G. Hector, A. Timmons, *J. Electrochem. Soc.* **2010**, *157*, 558.

[195]   M. Singh, J. Kaiser, H. Hahn, *Journal of the Electrochemical Society* **2015**, *162*, A1196-A1201.

[196]   T. Huria, G. Ludovici, G. Lutzemberger, *J. Power Sources* **2014**, *249*, 92.

[197]   C.-S. Kim, K. M. Jeong, K. Kim, C.-W. Yi, *Electrochim. Acta* **2015**, *155*, 431.

10 Table of Figures

11 Annex

The following source code was implemented in the Arduino software version 1.6.7, using standard libraries and transferred to a Teensy 3.2 overclocked to 96 MHz. The example is optimized for a frequency close to 160 kHz.

```
#include <stdint.h>
#include "ADC.h"

const int readPin = A10;
const int writePin = A14;
uint16_t i = 0;
uint16_t MinValue = 0;
uint16_t MaxValue = 0;
uint16_t PeakToPeak = 0;
uint8_t Maximum = 0;
const uint8_t RCN_data [37] ={64, 64, 64, 67, 70, 68, 58, 46, 45, 63, 89, 102, 87, 49, 17,
  17, 54, 101, 122, 101, 54, 17, 17, 49, 87, 102, 89, 63, 45, 46, 58, 68, 70, 67, 64, 64, 64};
uint8_t CollectedData [512];
uint8_t t0 = 0;
uint8_t t = 0;

ADC *adc = new ADC(); // adc object

void setup(){
 pinMode(LED_BUILTIN, OUTPUT);
 pinMode(readPin, INPUT);

 Serial.begin(9600);

 // Setup Analog to digital converter adc
 adc->setReference(ADC_REF_3V3, ADC_0);
 adc->setAveraging(0); // set number of averages
 adc->setResolution(8); // set bits of resolution ->Changed 12 to 8
 adc->setConversionSpeed(ADC_VERY_HIGH_SPEED);
 adc->setSamplingSpeed(ADC_VERY_HIGH_SPEED);
 adc->disableCompare(ADC_0);

 // disable DMA and interrupts
```

```
  adc->disableDMA(ADC_0);
  adc->disableInterrupts(ADC_0);


  //Setup DAC0
  analogWriteResolution(7);
  pinMode(writePin, OUTPUT);
  analogWrite(writePin, 64);

}

void loop(){
  delay(500);
  i = 0;
  for (i = 0; i < 37; i++){
    analogWrite(writePin, RCN_data[i]);
    asm volatile (".rept 5 \n\t nop \n\t .endr\n\t");
  }
  adc->startContinuous(readPin, ADC_0);
  t0 = micros();
  for (i = 0; i < 512; i++){
    CollectedData [i] = adc->analogReadContinuous(ADC_0);
  }
  t = micros();
  adc->stopContinuous(ADC_0);
  if (Serial.available()){
    Serial.print("ReadTime: ");
    Serial.println(t - t0);
    printData();
    eraseData();
  }
  digitalWriteFast(LED_BUILTIN, !digitalReadFast(LED_BUILTIN));
  delay(500);
}

void printData(){
  Evaluate();
  Serial.print("Peak to Peak Value: ");
    Serial.println(float(PeakToPeak) / 256 * 3.3);
```

```
Serial.println("Values:");
for (i = 0; i < 512; i++){
  Serial.print(float(CollectedData [i]) / 256 * 3.3);
  Serial.print(", ");
}
Serial.println("");
}

void Evaluate(){
  MaxValue = 0;
  MinValue = 256;
  for (i = 100; i < 512; i++){
    MaxValue = max(CollectedData [i] , MaxValue);
    MinValue = min(CollectedData [i] , MinValue);
  }
  PeakToPeak = MaxValue - MinValue;
}

void eraseData(){
  for (i = 0; i < 512; i++){
    CollectedData [i] = 0;
  }
}
```

12 Acknowledgments

I would like to express my gratitude to Prof. Dr. Gerhard Sextl for giving me the opportunity to join the Fraunhofer ISC and for providing the excellent conditions and room for personal development I have enjoyed during my thesis. Thank you for giving freedom for research and new projects and your supportive leadership.

I am indebted to the partners of the ABattReLife project and I would like to especially thank Dr. Simon Schuster, Martin Brand and Prof. Dr. Andreas Jossen for the successful cooperation. Simon, Martin, thank you for your great work and the visits to Munich's cellars and towers after our project workshops.

I would also like to thank my team and department leaders Jana Müller and Dr. Henning Lorrmann for their support as well as the great scientific, organizational and totally unrelated discussions. Jana, thank you for shaping our OE 324 into a great team and tutoring my thesis. Your coffee breaks were probably the best meetings I have seen so far. Henning, thank you for your trusting leadership and for empowering me and other PhDs in your department. I thank all the members of the OE 324 and all the electrochemists at Fraunhofer for the good times and the successful science we carried out.

I kindly thank Elena Fleder for her good mood, scientific eye and motivation. Elena, thank you for kindly but persistently pushing for better organization of meetings, workflow and filing system. I would probably still be searching for data pieces if it wasn't for you.

I am indebted to Wolfgang Virsik for building up all kinds of electronic circuitry and for his inventive mind. I learned a lot from you, and I could learn much more.

Angelika Schmitt was key to realizing the idea of ultrasonic state of charge estimation. Thank you, Angelika for your openness to this idea and your experienced help. That chapter would not exist if you wouldn't have invested your time.

Lukas Gold also invested a lot into our ultrasonic experiments and checking the physics behind our experiments. Lukas, it was great doing science with you and I wish you all the best for your PhD.